INTEGRATED, LOW-POWER SUB-NANOSECOND TIMING SYSTEMS FOR SPACE NAVIGATION AND COMMUNICATION

By

PAUL SERRA

A DISSERTATION PRESENTED TO THE GRADUATE SCHOOL
OF THE UNIVERSITY OF FLORIDA IN PARTIAL FULFILLMENT
OF THE REQUIREMENTS FOR THE DEGREE OF
DOCTOR OF PHILOSOPHY

UNIVERSITY OF FLORIDA

2018

To my loving family and to the memory of Maria Serra Pires

ACKNOWLEDGMENTS

This work have been completed under grant NNX14AO53G from the National Aeronautics and Space Administration Early Career Faculty program and grant NNX16AT13A from the National Aeronautics and Space Administration Space Technology Program, and thanks to the support of the United State Air Force University Nanosatellite Program. I would like to acknowledge Daniel Raible from the NASA Glenn Research Center for his generous support on the Miniature Optical Transceiver project, and the Mission Design Division at the NASA Ames Research Center for their effort on the Optical Precision Time Instrument. The projects in this dissertation could not have been completed without the precious help and the persistent work of many students from the Precision Space Laboratory. In particular, I would like to thank Seth Nydam, Nathan Barnwell, Tyler Ritz and Samantha Parry. I would not have been able to ... without their help and personal support. I am thankful to Kerri Cahoy and her students from the MIT STAR Lab for their support during the seed laser test. Also, I have special thanks for Darius Bunandar from the Quantum Photonics Laboratory who let me hijack all his equipment for a few days, and for his help during my stay in Boston.

Above all, I would like to thank my advisor, Dr. John W. Conklin. His unfailing support is the main reason I decided to stay to complete this degree.

TABLE OF CONTENTS

[1] The results in this section have already been published in (1)

[2] The results in this section are part of a forthcoming paper in the IEEE Transactions on Instrumentation and Measurement.

[3] The results in this section are part of a forthcoming paper in the IEEE Transactions on Instrumentation and Measurement.

LIST OF TABLES

LIST OF FIGURES

Abstract of Dissertation Presented to the Graduate School
of the University of Florida in Partial Fulfillment of the
Requirements for the Degree of Doctor of Philosophy

INTEGRATED, LOW-POWER SUB-NANOSECOND TIMING SYSTEMS FOR SPACE NAVIGATION AND COMMUNICATION

By

Paul Serra

May 2018

Chair: John W. Conklin
Major: Aerospace Engineering

Thanks to the continuous improvement in lasers, high quality and powerful pulsed light sources are now available and can be used to exchange time and data between spacecraft, over increasing distances. Time Transfer by Laser Link (T2L2), a payload host on the JASON-2 satellite, has established state-of-the-art performance for time-transfer. Time transfer with a space instrument has reached a precision of a few tens of a picoseconds. Optical timing systems can also be designed for communication, using schemes like pulse-position modulation. The Lunar Laser Communication Demonstration (LLCD) hosted on the Lunar Atmosphere and Dust Environment Explorer (LADEE) has demonstrated optical communications with pulsed lasers, with record data rates of 622 Mbps from a lunar orbit to earth.

This research explores two topics: How high-precision time transfer can be achieved with a spacecraft of limited size and power, and how pulsed laser communication systems can be built on similar platforms. This is done through two projects. The first one is a payload for time transfer between an optical ground station equipped with a laser and spacecraft. The second one is a modulator for a space-borne laser communication transmitters. These projects are enabled by two new technologies: compact atomic clocks and CubeSats. The miniaturization of atomic clocks provides accurate oscillators such as the Chip Scale Atomic Clock (CSAC) in very compact form-factors and with low power consumption. CubeSats are nano-satellites with standardized dimensions. They enable many organizations to access space at a reduced cost.

In this work, a compact instrument for the space segment of a small satellite time transfer mission has been designed, fabricated and tested. It can perform single-shot optical time transfer with a precision better than 80 ps in ground tests, with a power consumption below 250 mW while counting and below 5 W when performing time transfer. Components for a new pulse-based communication systems have been designed and evaluated. They include a software-defined modulator, implemented in a Field-Programmable Gate Array (FPGA). The modulator features a novel timestamp-based approach and a calibration circuit with an accuracy estimated at $1\sigma = 1.7$ ps, and is able to generate pulses at a rate of 20 MHz. In addition, a compact seed laser driver has been built and we have demonstrated gain-switched pulses of selectable duration, the shortest ones being 100 ps full width at half maximum, with a jitter below 25 ps.

The time transfer instrument has been integrated in a 10 cm $\times$ 10 cm $\times$ 30 cm spacecraft for a mission named CubeSat Handling of Multisystem Precision Time Transfer (CHOMPTT). Launch is expected in May 2018. The components developed in the second part of this work will support an upcoming small satellites optical communication cross-link mission called CubeSat Laser Intersatellite CrosslinK (CLICK) in the 2019 timeframe.

CHAPTER 1
INTRODUCTION

1.1 Precision Timing Usage

1.1.1 Navigation

Navigation may be the most ubiquitous usage of precision timing. Global Navigation Satellite Systems (GNSS) are constellations of satellites broadcasting precise radio-frequency time signals. The Global Positioning System (GPS) was the first constellation to be completed, in 1995, by the United State Department of Defense. It has since been joined by GLONASS from Russia partially completed in 1996 and Galileo built by the European Union in 2010. Several local augmentation systems have been built, such as Differential Global Positioning System (DGPS) and European Geostationary Navigation Overlay Service (EGNOS). China is in the process of extending a local system into a global constellation called BeiDou-2 by 2020.

All global constellations are based on the same concept of operation. The satellites in medium earth orbit send time signals to users on Earth or lower orbits. A user can measure the time difference at arrival between several the satellites of the system, and with the speed of light, find a difference in distance to the satellites called pseudorange. With at least 4 pseudoranges, the user can estimate its own position and obtain a time reference on-par with the spacecrafts clocks. Since it has been made available for public use, GPS has been the most commercially impactful space system. GNSS requires that each member of the constellation share a common time reference, and because of that they must be regularly synchronized. GNSS not only provides precision timing in space, they also need to exchange precision timing with a ground station for synchronization.

1.1.2 Time Standard Propagation

The International Atomic Time (Temps Atomique International, TAI) is calculated from the weighted average of hundreds clocks, with a few atomic clocks used as primary references (9 in 2016 (3)). The National Institute of Standards and Technology (NIST) maintains a time an frequency standard for the United State with the fountain atomic clock NIST-F1 and

NIST-F2, and takes part in the TAI. The TAI is the base of the Coordinated Universal Time (UTC). So transferring time with a high accuracy between the various clocks all around the Earth is necessary to establish the UTC, and UTC is the reference for civilian time all over the world.

Radio Frequency based time-transfer are executed on a regular basis, based on observation at the same time of GNSS signals, including GLONASS and GPS. The Two-Way Satellite Time and Frequency Transfer (TWSTFT) is another RF system used to establish TIA, hosted on some GEO satellites (4).

1.1.3 Communications

If distant systems are capable of time-stamping common events, then they can share information. If one of them is generating the event, it controls the information being shared, and can use that to communicate. Pulse-Position Modulation (PPM) is an example of modulation scheme using time to convey information. It is described in section 1.5. Space optical communications based on PPM an other schemes have been considered since the beginning of space exploration, but have gained considerable traction since the invention of the laser in 1960. Several systems have been tested since the 1990s.

Communication systems built around precision timing have advantages for long ranges, beyond earth orbit. In order to achieve long range, such systems must concentrate the available energy in short, very intense pulses. As the range requirements increase, so should the time between pulses, to keep consumed power under control. With low pulse rates, below the tens of kilohertz range, the quality of the reference oscillator has an impact on the error rate, and systems based to Time to Digital Converters (TDC) like the one presented in this dissertation can bring an advantages in term of low complexity and power efficiency compared to approaches based on Analog to Digital Converters (ADC). On the other hand, TDCs are limited to repetition rates under the hundred of megahertz range. Systems designed around ADCs do not require a comparator, which introduce a hard decision on pulses. Because of that

they usably perform better in case of high channel noise. ADCs can also reach superior data rates.

1.2 Advantages of Optical Pulses

They are several key advantages to relying on light pulses instead of Radio Frequencies (RF). Light is less affected by the ionosphere. Most lasers used for ranging and communications use wavelengths between 532 nm and 1550 nm. This correspond to hundreds of THz in frequency, while RF systems are limited to high GHz values. In the atmosphere, fluctuation of the index of refraction introduce beam deflection and variations in time delay, in particular in the ionosphere. Since ionospheric disturbances are proportional to $1/f^2$, laser light is much less affected (5).

Diffraction is proportional to the wavelength, so light beams can be tighter than RF beams , with smaller apertures. This results in more compact, lower power designs. Alternatively, higher data throughputs can be achieved with equivalent Size, Weight and Power (SWaP). Data throughput can be improved by factors of 10 or even 100. A good figure of merit to compare RF and optical systems is the Effective Isotropic Radiated Power, or EIRP. The EIRP is equal to the total power that would be emitted by an isotropic antenna to match the power emitted in the best direction of the antenna, where the signal is the most intense. Tighter beam leads to higher EIRP. The LADEE LLCD experiment, using a 10 cm aperture with 1550 nm light, had the same EIRP as a 34 m S-Band dish of the Deep Space Network, around 8 GW (6). This means that at long ranges, those two systems can radiate a similar amount of power to a target of identical size, while having vastly different size and weight. However, as the radiated energy gets more concentrated, better pointing capabilities are required. Coherent optical signals are more complicated to generate and amplify, and the amplification efficiency is much lower compared to RF. Finally, optics requires tight mechanical tolerances, better alignment and greater surface quality than RF waveguides.

Another advantages of optical frequencies is the lack of frequency licensing or coordination. Currently, the RF spectrum is crowded, and frequency allocation and licensing is a complex

and sometime expensive process. With optical communication, isotropic and low directivity apertures are unpractical. Since the diffraction is much reduced compared to radio frequencies, and light does not penetrate obstacles, transmitter and receiver can be discriminated with optics and allocation mechanisms are not required yet. On the other hand, there is legislation that applies to free-space lasers for safety reasons. In the United States, the Federal Aviation Administration (FAA) impose limits in navigable airspace and in particular close to airports. The Joint Space Operations Center (JSpOC) maintains a service called the Laser Clearinghouse (LCH) for deconfliction with spacecraft. It is mandatory for Department of Defense (DoD) lasers emitting above the horizon, but voluntary for other users not funded by the DoD. There is also an American national standards for the safe use of lasers (ANSI Z 136.1 2007) and several individual states have laws on free-space lasers.

1.3 Time Standards

1.3.1 Oscillator Technology

In this subsection, we summarize the types of oscillators commonly used in modern electronics, as well as the most accurate ones built to this date.

1.3.1.1 Relaxation oscillators

Relaxation oscillators are based on the continuous augmentation of a parameter and a threshold to release it. They are non-linear devices. A simple example can be built with two passive components. A capacitor is charged and discharged through a resistor, and cycled with a comparator. This gives low cost, low power and low accuracy frequency sources that can be added inside integrated circuits with no external components. The NE555, the most popular circuit ever manufactured, can be operated as a relaxation oscillator (7).

1.3.1.2 Harmonic oscillators

Contrary to relaxation oscillators, harmonic oscillators are linear devices and generate sinusoidal outputs. Accurate clocks use resonators too keep frequency constant through time. R-L-C circuits are an example of resonators, but more stable ones are usually used as primary frequency source.

Quartz Crystals. Quartz crystals, and some ceramic materials, are subject to the piezoelectric effect. Electric charges applied to the material create stress in it. Deformation can be applied and sensed with voltage on a pair of electrodes. If the material sample is cut to obtain a mechanical resonance, this createsa stable electric resonator. Different cuts are available to generate a wide range of frequencies, typically from kHz to 100s of MHz. An open crystal oscillator is shown in figure 1-1A. Bias voltages can be applied to steer the obtained frequency. This allows one to compensate for temperature variations. These oscillators are then called Temperature Compensated Crystal Oscillators (TCXO). For even more stability, quartz crystals can be kept at constant temperature with an heating elements, this results in an Oven Controlled Crystal Oscillators (OCXO). Some high-performance oven controlled quartz oscillators are called Ultra-Stable Oscillators (USO). The performance of crystal oscillators is diverse. They can be designed as cheap low power devices, or as high accuracy space-grade ultra-stable oscillators of several kilograms.

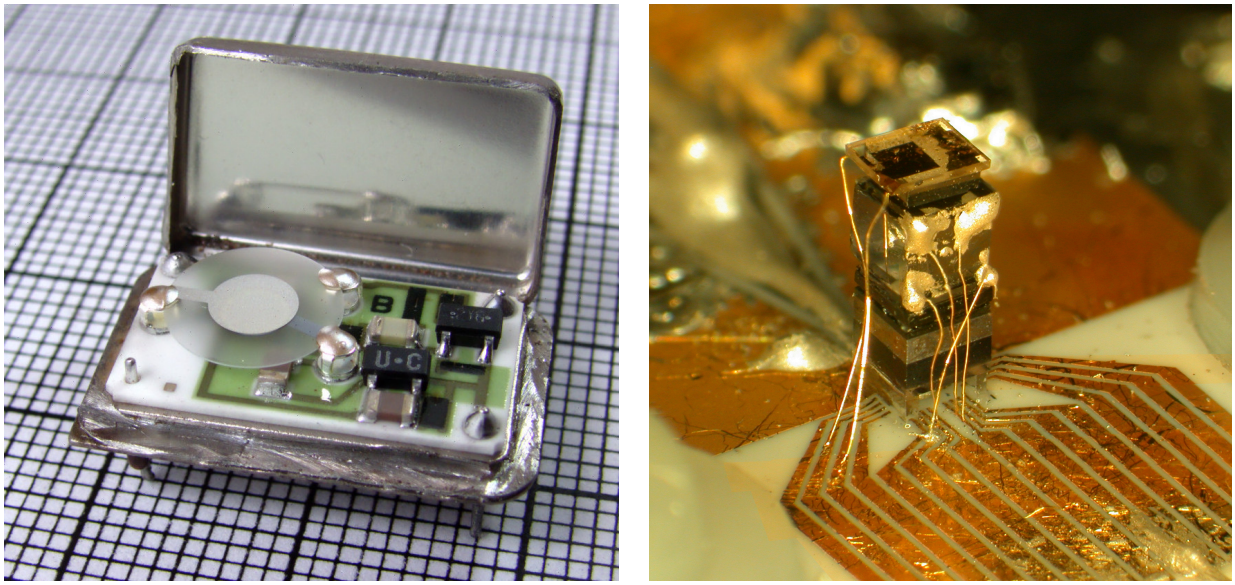

A B

Figure 1-1. A) Internals of Kyocera KXO-01 crystal oscillator, by Marcin Andrzejewski, under CC BY-SA 3.0. B) Physics package of a chip-scale atomic clock, picture from NIST

1.3.1.3 Atomic Clocks

Maser. Maser stands for Microwave amplification by stimulated emission of radiation. Hydrogen Masers designed for timekeeping use a radio-frequency cavity as a resonator. The oscillation is maintained by injecting excited hydrogen atoms into the cavity. The hydrogen atoms then decay to a lower energy level through stimulated emission, generating photons with a frequency of 1.42 GHz. Masers are currently the most accurate devices available for time keeping with integration times below 10,000 seconds.

Atomic Beam. Cesium and Rubidium atomic clocks also use a RF cavity, but instead of stimulated emission, absorption is used. The frequency is tunned to maximize the absorption of the RF power, and a detector estimates the number of atoms in the higher energy state using fluorescence and provides feedback. The physics package from a miniaturized atomic clock is shown in figure **??**. It includes a cell of cesium atoms, electrodes to deliver the RF excitation signal, and a laser plus a photodetector to measure the state the atoms.

Atomic Fountain. Fountain clocks are similar to beam clocks. The atoms are cooled and placed in weightlessness to increase the time during which RF power is absorbed, increasing the contrast of the clock.

Optical Atomic Clock. Optical atomic clocks use optical frequencies instead of radio frequencies to change the states of neutral atoms. They are currently the most accurate clocks for long integration times.

1.3.1.4 Voltage Controlled Oscillator (VCO)

Both relaxation oscillators and harmonic oscillators car be designed so that they can be controlled, and their frequency adjusted, usually with a voltage or digital value. Controlled oscillators are a central part of phase-locked loops.

1.3.2 Short Term Errors: Phase Noise and Jitter

Just as the electrical parameters of a circuit such as voltage and current have noise and uncertainty, the measured time of an event or the phase of periodic signal is also susceptible to noise. For time intervals below 1 second, jitter and phase noise are the standard measures.

1.3.2.1 Jitter

Noise in the time domain of an event is called jitter. There are several types of jitter. Random jitter is typically Gaussian, and accounts for random effects of uncorrelated noise sources. Deterministic jitter accounts for errors from correlated sources, such as data patterns on the signal itself or disturbances driven by the same clock signal. Deterministic jitter is bounded.

Jitter definitions can vary. It can be taken as the variation from period to period of a clock (cycle jitter) or variation in position of a clock rising or falling edge against a reference (absolute jitter).

1.3.2.2 Phase Noise

Phase noise, noted $\mathcal{L}(f)$, is the frequency domain equivalent of jitter. $\mathcal{L}(f)$ is defined as the spectral density of the fractional frequency. Jitter can be estimated from phase noise, by integrating it with Equation 1–1.

$$x_{jitter} = \frac{1}{2\pi f_0}\sqrt{\int 2\mathcal{L}(f)df} \tag{1–1}$$

Here, f_0 is the nominal frequency of the periodic signal.

1.3.3 Long Term Errors: Allan Deviation

The Allan deviation is a statistical tool introduced by David W. Allan in (8) . It allows one to compare the stability of oscillators.

1.3.3.1 Definition of the Allan Deviation

The Allan deviation is based on the fractional frequency $y(t)$, which is the normalized value of the difference between the instantaneous oscillator's frequency $f(t)$ and the nominal value of the frequency f_n. The average of $y(t)$ over an interval τ can be computed by integrating $y(t)$ as follow:

$$y(t) = \frac{f(t) - f_n}{f_n} \qquad \overline{y}(t,\tau) = \frac{1}{\tau}\int_0^{\tau} y(t + t_v)dt_t v \tag{1–2}$$

The fractional frequency $y(t)$ can be related to the time error $x(t)$. The quantity $x(t)$ is the difference between the oscillator phase in seconds and the nominal time. If the deviation is computed from samples of the phase, made with a measurement time-base of τ_0, then $\overline{y}(t,\tau)$ can be rewritten as a function of the phase values $x(t)$ (9):

$$x(t) = \int_0^t y(t_v)\,dt_v \qquad \overline{y}(t,\tau) = \frac{x(t+\tau) - x(t)}{\tau} \tag{1–3}$$

The Allan deviation can be defined as the standard deviation of two samples of the normalized frequency fluctuation separated by a time interval τ. For this reason, the Allan variance is also known as the two-sample variance, and can be expressed as (9):

$$\sigma_y^2(\tau) = \frac{1}{2}\left\langle (\Delta y)^2 \right\rangle \tag{1–4}$$

If we assume that the interval τ is both the averaging time and the sampling period, then Equation 1–4 becomes:

$$\sigma_y^2(\tau) = \frac{1}{2}\left\langle (\overline{y}(i\tau+\tau,\tau) - \overline{y}(i\tau,\tau))^2 \right\rangle_i \tag{1–5}$$

Equation 1–4 and Equation 1–5 can also be written in terms of phase errors (9):

$$\sigma_y^2(\tau) = \frac{1}{2\tau^2}\left\langle (\Delta^2 x)^2 \right\rangle = \frac{1}{2\tau^2}\left\langle (x(i\tau+2\tau) - 2x(i\tau+\tau) + x(i\tau))^2 \right\rangle_i \tag{1–6}$$

This expression can also by derived from (8) as shown in Appendix A

1.3.3.2 Estimators

The Allan deviation is defined as an expected value, assuming averaging over an infinite amount of time. Unfortunately, we could not wait long enough to satisfy this requirement. Estimators of the Allan deviation must be used instead.

Non-overlapped. If N phase measurements made at an interval τ_0 are available, it is possible to evaluate to $\sigma_y^2(n\tau_0)$ by averaging Equation 1–6 $\frac{N-1}{n} - 1$ times.

$$\sigma_y^2(n\tau_0, N) = \frac{1}{2(n\tau_0)^2}\frac{1}{(\frac{N-1}{n}-1)}\sum_{i=0}^{\frac{N-1}{n}-2}(x_{i+2n} - 2x_{ni+n} + x_{ni})^2 \qquad n \leqslant \frac{N-1}{2} \tag{1–7}$$

Overlaped. The previous estimator only uses $1/n$ of all available samples, but has the advantage of averaging only statistically independent terms. Reference (10) introduced an estimator with improved accuracy as n rises and approaches $N/2$. This estimator is the standardized method to measure the Allan variance (11).

$$\sigma_y^2(n\tau, N) = \frac{1}{2n^2\tau^2(N-2n)} \sum_{i=0}^{N-2n-1} (x_{i+2n} - 2x_{i+n} + x_i)^2 \qquad n \leqslant \frac{N-1}{2} \tag{1–8}$$

1.3.3.3 Interpretation of the Allan Deviation

If we only consider two frequency samples, Equation 1–5 yields:

$$\sigma_y^2(\tau) \approx \frac{1}{2}(\overline{y}(t_0+\tau, \tau) - \overline{y}(t_0, \tau))^2 \tag{1–9}$$

If we assume that the frequency at time t_0 is known, and that the clock random walk follows a Wiener process, this result can be interpreted as the distribution of the frequency at time $t_0 + \tau$:

$$\overline{y}(t_0+\tau, \tau) \sim \mathcal{N}\left(\overline{y}(t_0, \tau), 2\sigma_y^2(\tau)\right) \tag{1–10}$$

By replacing $\overline{y}(t_0+\tau, \tau)$ and $\overline{y}(t_0, \tau)$ by their definition from Equation 1–2, this can further be approximated to:

$$\overline{f}(t_0+\tau, \tau) \sim \mathcal{N}\left(\overline{f}(t_0, \tau), 2f_n^2\sigma_y^2(\tau)\right) \tag{1–11}$$

If we know the average frequency from t_0 to $t_0 + \tau$, noted $\overline{f}(t_0, \tau)$, then Equation 1–11 gives the standard deviation for the average frequency over the next period, from $t_0 + \tau$ to $t_0 + 2\tau$. For example, the CSAC has an Allan deviation of $3.0 \cdot 10^{-10}$ after 1 s (12). The CSAC, or Chip Scale Atomic Clock is a very compact cesium beam clock, produced by Microsemi Corporation. For the CSAC, with $\tau = 1$ s, $\sigma_y(\tau) = 3.0 \cdot 10^{-10}$, so , $f_n\sqrt{2}\sigma_y(\tau) = 4.24$ mHz. After one second, the average frequency over one second of the CSAC is expected to remain within a 4.24 mHz interval with a confidence interval of one standard deviation. This is equivalent to a phase error of 424 ps after 1 s. Note that this is derived from the CSAC specifications (12), measured phase error is expected to be lower.

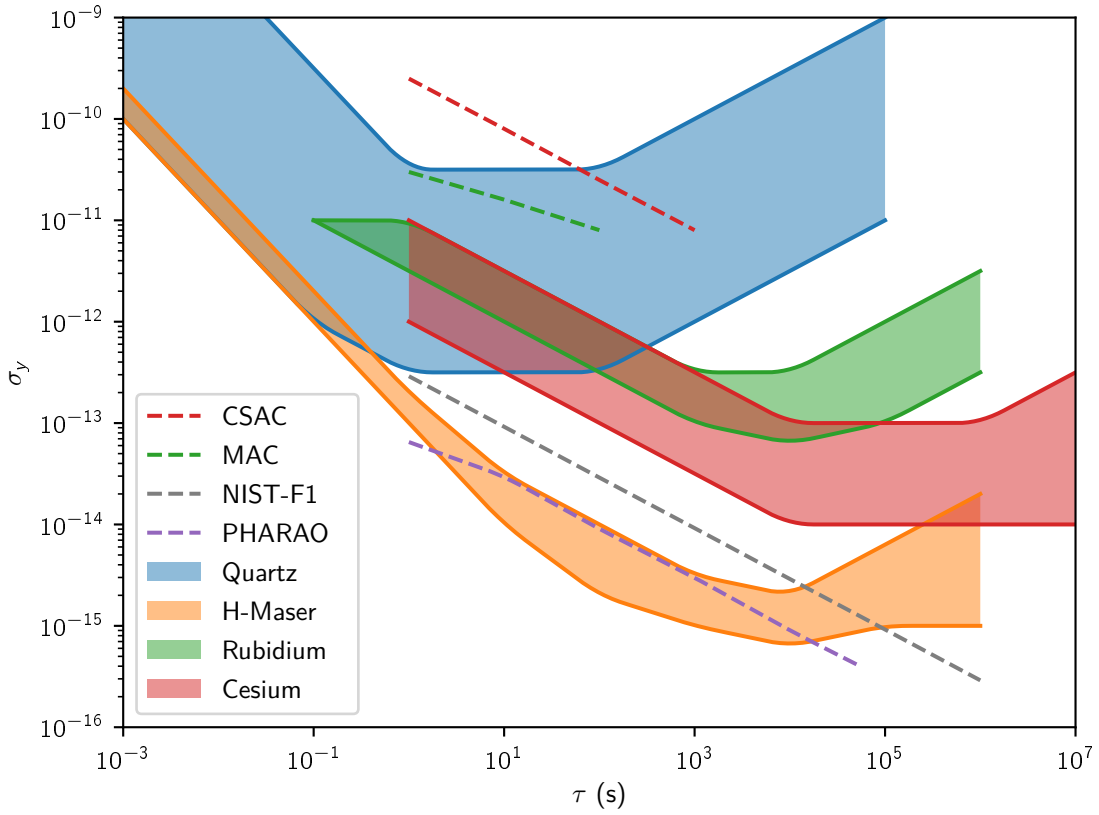

Figure 1-2. Typical Allan deviations of various types of oscillators (9) (12) (13)

Figure 1-2 is a compilation of the typical performance of various kinds of oscillators, reproduced from (9), with the addition of specific oscillators relevant in this work. In this figure, "Quartz" refers to high performances oven controlled quartz oscillators, sometimes referred as Ultra Stable Oscillators (USO). "Rubidium" and "Cesium" are respectively rubidium and cesium beam atomic clocks. The CSAC specifications are also included. The CSAC consumes less than 120 mW on average, below high performance OCXO. The next named clock is the Miniature Atomic Clock or MAC, it is a Rubidium atomic clock, also of small dimensions but with an higher average power consumption, at 5 W. The NIST-F1 is a cesium fountain clock. It is shown on figure 1-3A. NIST-F1 is the primary time and frequency reference of the United States. Finally, PHARAO is a cesium fountain reference designed for micro-gravity. The vacuum chamber hosting PHARAO's physics package is shown on

figure 1-3B. PHARAO is a part of the Atomic Clock Ensemble in Space (ACES), which is scheduled to fly to the International Space Station in 2018. Once launched, it is expected to be the highest performing clock in space (14). The CSAC and the MAC curves are from specifications, and are worse than measured performances. The data for the NIST-F1 is measured against an array of H-Masers, and the data for PHARAO is expected performance, based on ground tests (14).

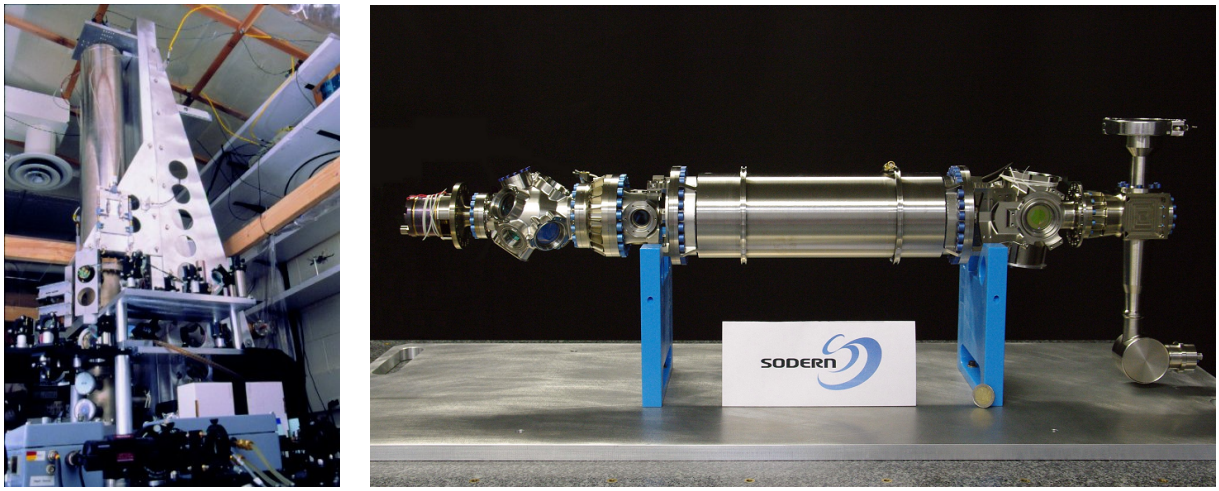

A B

Figure 1-3. A) The NIST-F1 atomic clock The NIST-F1 atomic clock, from NIST . B) The vacuum chamber for the physics package of PHARAO, reproduced with permission, ©EADS SODERN

1.3.3.4 White phase noise

A special case for the Allan deviation is that of white phase noise. It can be modeled as Gaussian random variables for time samples, with a jitter of σ_{wpn}.

$$\begin{aligned}\sigma_y^2(\tau) =& \frac{1}{2\tau^2}\left\langle \left(\mathcal{N}\left(i\tau+2\tau,\sigma_{wpn}^2\right)-2\mathcal{N}\left(i\tau+\tau,\sigma_{wpn}^2\right)+\mathcal{N}\left(i\tau,\sigma_{wpn}^2\right)\right)^2\right\rangle_i \\ =& \frac{1}{2\tau^2}\left\langle \left(\mathcal{N}\left(0,4\sigma_{wpn}^2\right)\right)^2\right\rangle_i\end{aligned} \tag{1–12}$$

The variance of $\mathcal{N}\left(0,6\sigma_{wpn}^2\right)$ appears in Equation 1–12. Once replaced by its formula, it becomes:

$$\sigma_y(\tau) = \sqrt{3}\frac{\sigma_{wpn}}{\tau} \tag{1–13}$$

Phase noise can be identified as a curve with a slope of $1/\tau$ on allan deviation plots.

1.4 Measuring and Distributing Time with Electronics

Generating, transmitting and sampling time requires various electronic circuits. In this section, we will present building blocks used to manipulate clock signals and time events.

1.4.1 Devices

The circuits examined in this section can be integrated into different kinds of components. A micro-controller can be programmed to execute a program. Most micro-controllers include peripherals such as counters which can be controlled by the software. Field-Programmable Gate Arrays (FPGAs) are programmable devices capable of directly implementing logic circuits. They contains hundreds of thousands of logic blocks called cells built with look-up tables and registers, which can recreate any combinational or sequential logic functions. The logic blocks are connected together by a connection matrix. The association of the routing matrix and the cells is called the fabric. Some FPGAs include complex circuits and clocking resources that cannot be implemented with the fabric as efficiently as hard-wired modules. Application Specific Integrated Circuits (ASIC) are specialized circuits. They are dedicated to a particular use and cannot be reprogrammed.

1.4.2 Phase Locked Loops

Phase Locked Loops, abbreviated as PLLs, are control systems capable of generating clock signals in phase with their input. PLLs are extremely common circuits, used in many applications. When data is received without an associated clock signal, PLLs can be used to generate a clock signal in phase with the data stream, with a process called clock recovery. They can also decode frequency-modulated signals, and can be used as clock buffer with no phase delay, even with changes in voltage, temperature or frequency. PPLs can reduce jitter, by filtering the high frequency part of the input phase noise. They are still limited by the phase noise of their own oscillator. PLLs are frequently used in clock distribution, and they can generate frequencies that are an integer fraction of the input frequency. This fraction can be inferior or superior to one: PLLs can generate frequencies higher than what they receive.

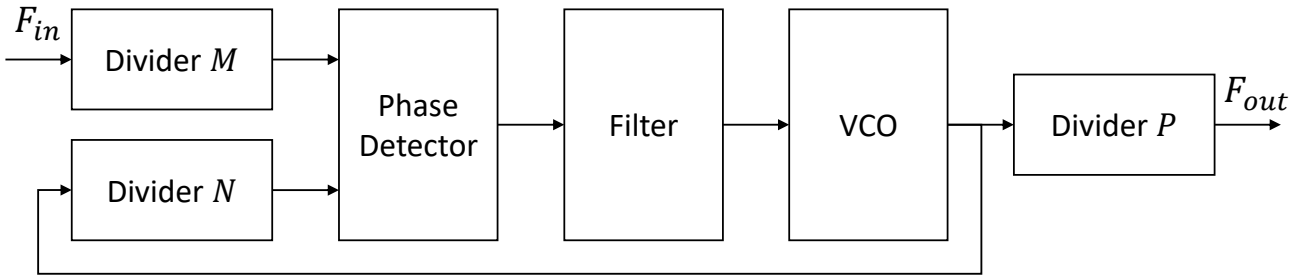

Figure 1-4. Block diagram of a phase locked loop

A simplified example of a PLL is shown in Figure 1-4. The main components are a phase detector, a loop filter, and a controlled oscillator. The phase detector generates a signal proportional to the phase difference between its two inputs. A very simple form of phase detector is exclusive-or gate, which outputs a high signal whenever the inputs don't match. The loop filter is usually a low pass filter, required to stabilize the loop and filter out unwanted high frequency clock variations. PLLs must include a controlled oscillator. The most common ones are Voltage Controlled Oscillators (VCO).

PLLs sometime have dividers connected on outputs or inputs. An output divider, such as P on Figure 1-4, allow the VCO to run at a higher frequency than the required clock output. VCOs integrated on Silicon IC rely on on-chip inductance and tend to run at GHz frequencies, and faster than most circuits driven by PLLs. The divider P also extends the range of possible output since integrated VCOs have limited tuning capabilities. Dividers at the inputs, M and N on Figure 1-4, allows the generation of fractions of the input frequency. Divider M reduces the frequency at the input, so both M and P divide the output frequency. Divider N acts on the feedback arm of the loop. Since the feedback mechanism forces the frequencies received by the phase detector to match, the VCO must run faster to match the input, so N is multiplying the output frequency. Accounting for all of these dividers results in the following equation:

$$F_{out} = \frac{N}{M \cdot P} F_{in} \tag{1–14}$$

Note that M, N, and P are divider values, and must be non zero integers. Phase detectors require a minimum input frequency in order to keep the loop locked. Therefore M and N cannot be arbitrarily high.

1.4.3 Counters

Counters store the number of occurrences of an event, such as the rising edge of a clock signal. They can both record and generate time. They record time with capture registers, in which an event, typically a pulse edge, triggers a recording of the current counter value. They can also be used with compare registers, where the value of the counter is compared to a programmed value to generate an event. Because they count the number of clock cycles, their resolution is limited to a clock period. In programmable devices such as FPGAs, counters can typically run at frequencies up to 500 MHz. Counters can be built with arbitrary length, in number of bits. This make them very suitable for long-term time-keeping. For example, a 32 bit counter running at 500 MHz will saturate and roll-over after 8 seconds, and a 64 bit counter at the same frequency will not saturate for more than a thousand years.

Some FPGAs include Serialization/Deserialization (SERDES) modules built in the I/O pin structures (15). Those modules are intended for high rate serial links, such as PCI express or USB 3 (16). They receive information in a serial form at very high rates, accumulate it in registers, and output it in parallel, at lower rates. The SERDES modules can also do the converse: receive data in parallel and output it at high rate on a single output. SERDES modules can be used to extend counters at higher frequencies. As of early 2018, the fastest commercially available design can reach transfer rates of 32 Ghz, which corresponds to a resolution of 31 ps. However, FPGAs designed for space application are limited to frequencies below 5 GHz. Because the modules are built for error-free data transfer, their accuracy for timing application is guaranteed to be significantly lower than their resolution.

1.4.4 Delay chains and signal propagation

Delay chains can generates small time increment without using high frequencies. An example is displayed in Figure 1-5. The minimum increment is usually the delay of a single

logic gate, which is around 10 ps on recent integrated circuits. By selecting the gate output at one of the chain stages, it is possible to obtain a signal delay of $t_n \approx n\tau$.

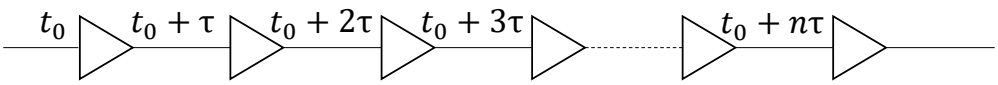

Figure 1-5. An example of delay chain

The delay increment, τ, is subject to environmental effects and random variations. These effect are mainly Process, Voltage, and Temperature, abbreviated to PVT variations. Process comprises all the variations introduced by the fabrication process. Increasing the supply voltage tends to reduce the delay of a logic gate, at the cost of power dissipation. On the other hand, increasing temperature tends to increase the delay. Two other effects are not included in PVT variations: aging and radiation. Aging is a complicated process to model, depending not only on time, but also on stress from use and recovery mechanisms. Radiation is a problem specific to space hardware. Radiation damage will modify the switching threshold of transistors in CMOS (Complementary metal–oxide–semiconductor) integrated circuits, causing a change in the switching time. Radiation will also change the propagation time in unprotected flash-based programmable logic devices, where flash cells directly control interconnections (17): electrical charges will be injected in flash cells by ionizing rays and particles, slowly changing the potential at the gate of transistors used in connection matrices. This changes the load on the gate output and slows their response time.

Since delay chains are open-loop structures, PVT variation, radiation and aging create non-linearities. They can be measured with Differential Non-linearity (DNL), defined in Equation 1–15, and Integral Non linearity (INL), defined in Equation 1–16. For a delay chain of N delay elements, from τ_1 to τ_N, with $t_i = t_0 + \sum_{i=1}^{N} \tau_i$:

$$DNL(i) = \frac{t_i - t_{i-1}}{\overline{\tau}} - 1 = \frac{\tau_i}{\overline{\tau}} - 1 \tag{1–15}$$

$$INL(i) = t_i - t_0 - i \cdot \overline{\tau} \tag{1–16}$$

In Equation 1–15 and Equation 1–16, $\overline{\tau}$ is the average time delay of a single chain element. For the complete chain, $INL = \max_i INL(i)$ and $DNL = \max_i DNL(i)$. Non linearities can be quite large in programmable devices, because they are not designed with precision timing in mind. For example, a delay chain presented in subsubsection 3.2.2.2 has a DNL higher than 800%. Specialized integrated circuits usually have lower non-linearities.

All the gates on the chain are also subject to noise. Because of this, the jitter of the signal tends to increase as it travels through the chain. This effect can be significant, and limit the practical size of delay chains.

1.4.5 Time-to-digital converters

A Time-to-Converter (TDC) is a circuit which convert an electrical event, almost always a signal edge, into a digital time value. Some TDCs can integrate the time between a start signal and a stop signal. In this case they can also be called Time Interval Counters. Otherwise, they tag one or more stop signals against a clock, in witch case they are designated as Time-stamping TDCs. There are several ways to build TDC circuits, such as time-to-amplitude converters, built with a current source and a capacitor, or pulse stretching converters (18). TDC systems have also been implemented with pulse shaping circuits coupled with high-speed analog to digital converters (19). We will focus on a method called the taped delay line. An example of taped delay line converter is shown in Figure 1-6.

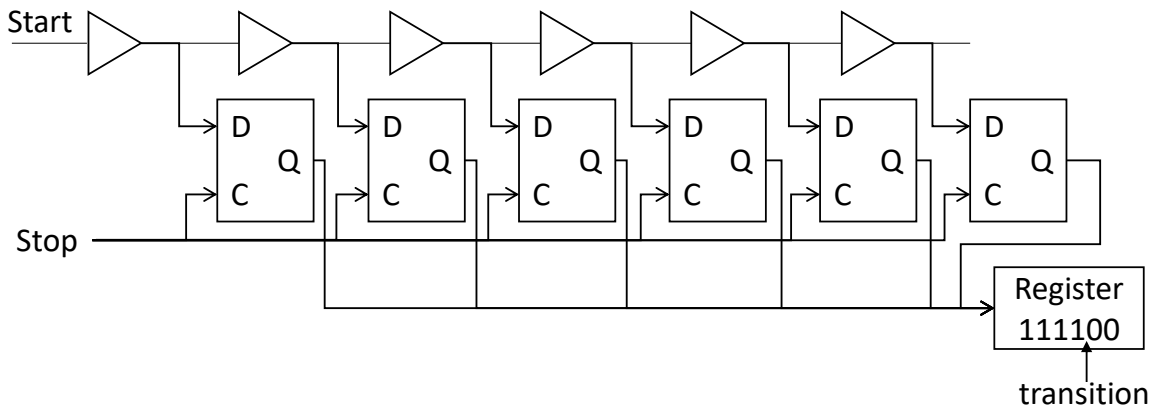

Figure 1-6. Structure of taped delay line time-to-digital converter

The converter in Figure 1-6 utilizes a delay chain. The start signal is referenced by its rising edge. The signal starts propagating at a slow speed through the chain, at t_{start}. A D-latch is placed after each delay element. Latches will record the state of their input D when they receive a rising edge at their input C. At this time, the value of D will be transferred to their output Q and stay constant until the next rising edge on C. A stop signal arrives after a certain time t_{stop}. The stop signal can be distributed simultaneously to all the latches. The output of the latches can then be read. The output will be high up to the position of the rising edge signal in the chain, were it will transition to a low level. The position of the transition gives a reading of $t_{stop} - t_{start}$ with a resolution equal to the delay of one element of the chain. The defect such as INL and DNL discussed in subsection 1.4.4 are also present. A related method to build TDCs is called the time vernier. With this method, the stop signal is also propagated through a delay chain, but still faster than the start chain. The resolution is then equal to the average of one element of the start chain minus one element of the stop chain.

1.5 Pulse-Based Communication

As mentioned is section 1.1, precision timing can be used to exchange data. A event can be generated with a oscillator as reference, for example a light pulse can be emitted by a laser at a selected time. This event can be observed from another location and timed against a local oscillator. If the difference between oscillator was known before the event, then arbitrary information can be transmitted. There are several schemes used for transmitting data in this way.

1.5.1 Pulse Position Modulation

Pulse Position Modulation, or PPM, is a scheme based on the principle described above. An example of PPM frame is shown in Figure 1-7. Time is divided into M slots of duration τ. To signal a PPM symbol, an event, usually a pulse, is generated in on of the slots. Each slot encodes a unique symbol, among M possibilities. The device generating the event may need a certain amount of time to prepare for the next pulse. For example, a high-power laser could need time to build up enough energy in its cavity, in order to emit a large enougth pulse. This

duration is called the guard time, noted T_g. T_g is inserted after each group of M time interval τ. M different symbols can encode up to $log_2 M$ bits, and the total time to send a symbol $M\tau + T_g$. From this, the data rate D_{PPM}, in bit per second, can be calculated:

$$D_{PPM} = \frac{\text{data per pulse}}{\text{time per pulse}} = \frac{log_2 M}{M\tau + T_g} \tag{1–17}$$

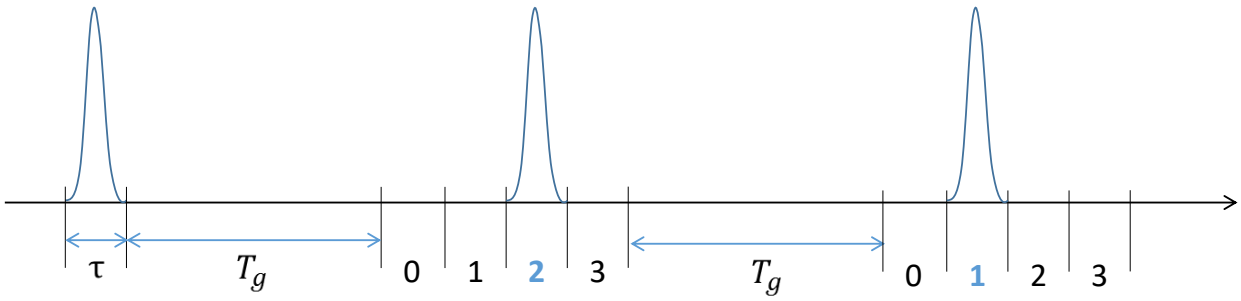

Figure 1-7. Example of pulse position modulation with $M = 4$

1.5.2 Differential Pulse Position Modulation

One of the variations of Pulse Position Modulation is Differential Pulse Position Modulation (DPPM). Figure 1-8 is an example of a DPPM transmission, again with $M = 4$. The difference with between PPM and DPPM is that the guard time T_g is inserted immediately after the pulse. The reference for the next pulse is not the last possible slot, but the previous pulse, so the data is encoded directly in the time difference between the pulses, hence the qualification of differential. The number of symbols and the associated number of bits encoded by the pulses remains the same, but the time to send a symbol is, on average, shorter. At worst, it is equal to the time by symbol of PPM. On average, the data rate D_{DPPM} is improved:

$$D_{DPPM} = \frac{\text{data per pulse}}{\text{average time per pulse}} = \frac{log_2 M}{(M+1)\tau/2 + T_g} \tag{1–18}$$

The drawback of DPPM is that the data rate can be variable, and the design of the receiver can be more difficult as the position of the data encoding time slots τ are different from pulse to pulse. Also, in some cases where there is excessive noise, pulses missed by the detector

could introduce a shift in the data stream. Similarly, extra pulses generated by noise sources can shift the data stream in the other direction.

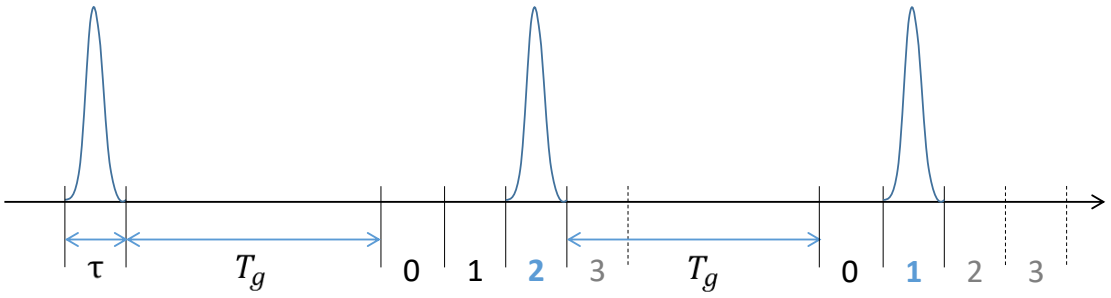

Figure 1-8. Example of differential pulse position modulation with $M = 4$

1.6 Contributions

The next chapter will discuss a new compact instrument for time transfer called OPTI, or the Optical Precision Time Instrument (20). It has a much reduced volume, weight, and power compared to precious systems with similar performance. This chapter will cover the principle, the architecture and the resulting performance of the instrument. A precision below 80 ps has been achieved, with a power below 5 W in a volume of less than 10 by 10 by 3 cm for one complete instrument channel.

My contributions to the CHOMPTT mission were centered on the two instrument channels of OPTI. I designed the instrument architecture, and draw the circuits for OPTI 1 (a breadboard version), OPTI 2 (a first engineering units), OPTI 3 (a second engineering units) and OPTI 3.1 (the flight version). I received some help from Seth Nydam on the power section of OPTI 3. I completed the layout and tested the electronics board for OPTI 1, OPTI 2 and OPTI 3.1. This include some repairs on OPTI 3.1 (the flight boards). I also wrote the software of OPTI 1, and of OPTI 2 with the participation of Blake Richard. I completed an initial release of the OPTI 3.1 embedded software that was later completed by Seth Nydam. Last, I put together a data post-processing and debugging script for OPTI 3.1.

Several other graduate students heavily contributed to the OPTI project and the CHOMPTT mission. Nathan Barnwell was responsible for the experimental setup of OPTI

1. He also did the analysis of the data collected by this experiment. He completed all the optical link budgets, from OPTI 1 to OPTI 3.1. Nathan helped with mechanical design of the flight instrument, and worked on the optical ground station. Seth Nydam did board layout of OPTI 3.0, and participated to the OPTI 3.0 schematics. Seth tested OPTI 3.0 and OPTI 3.1, and completed the flight software for the channel boards. He designed, laid out, fabricated and programed the instrument supervisor. Seth and Nathan collected data on OPTI 3.1. I analyzed some of this data in subsec:31dataan. Tyler Ritz worked on the optical ground station. Several undergraduate student worked under the supervision of Seth, Nathan and Tyler on some aspect of the instrument. Many have also contributed to CHOMPTT mission outside of OPTI.

Chapter 3 will examine a modulator and a seed laser for the Miniature Optical Communication Transmitter (MOCT) (2). The modulator use a novel approach based on timestamps. It is entirely contained within a FPGA and is highly flexible. The modulator includes a calibration circuit with an unprecedented accuracy of 2 ps in a programmable device. The seed laser driver, originally developed for another application (21), is capable of generating gain-switched pulses from 100 ps to arbitrary duration. It features a very high extinction ratio, along with a jitter below 25 ps.

On MOCT, my contribution includes the entirety of the modulator software and its calibration circuit presented in chapter 3. I designed the seed laser driver described in the same chapter, and guided Samantha Parry through the schematic capture and the layout for this board. I tested the seed laser and analyzed the results. I also worked on elements of the project that are not included on this dissertation. They included simulation of a receiver chain compatible with the transmitter of MOCT, and the schematics for a set of boards that included all the required functions for a long range optical modem.

Nathan Barnwell tested and developed a model of an erbium doped fiber amplifier to be used with the modulator. Nathan completed all the optical link budgets, and he also explored various possible mission configuration for MOCT. Tyler Ritz have adapted, improved and built detector assemblies for this second project.

CHAPTER 2
SUB-NANOSECOND TIMING OF OPTICAL PULSES IN A COMPACT PACKAGE

Fist, we will review previous techniques and similar missions section 2.1. Then, we will introduce the CHOMPTT mission and explain its concept of operation and objectives. We will show CHOMPTT's instrument, OPTI (Optical Precision Timing Instrument), and compare it to the state of the art in section 2.2. We will explain OPTI's architecture and its evolution in section 2.3, and list its major components. A scheme to identify the exchanged pulses will be presented in section 2.4. Last, data that resume the instrument performance will be analyzed in section 2.5. This section will also contain suggestion for future test.

2.1 Related Systems & Methods

Time transfer can be carried out on the ground with networks and telecommunication technologies. The Network Time Protocol is the most common way to synchronize computers, through Internet Protocol (IP) networks. It can reach an accuracy of a few tens of milliseconds. Coaxial cable and dedicated optical fibers can distribute frequency timing over long distances, within a continent. In this section, we will focus on space methods, suitable for intercontinental links.

2.1.1 GNSS Carrier Phase

GNSS Receivers are the most common tool to precisely synchronize distant clocks. The highest accuracy measurements are obtained by measuring the phase of GNSS RF signals and is called the Carrier Phase method. Accuracy below 250 ps can be achieved over an averaging period of 24h. (22).

2.1.2 TWSTFT

Two-way Satellite Time and Frequency Transfer (TWSTFT) is a radio-frequency time transfer system hosted on a few satellites in Geo-synchronous orbit (4). TWSTFT payloads act as transponders between two ground users. Each user sends a modulated pseudo-random RF signal to the TWSTFT space segment. The signals are repeated to the opposite users, allowing them to find the time difference between their emitted signal and the signal received from the

distant user. After a few minutes of averaging, TWSTFT can reach an accuracy of less than a nanosecond. Over 30 min, the error is similar to the GNSS carrier phase method.

2.1.3 LASSO

LASSO stands for Laser Synchronization from Stationary Orbit. The space segment for this experiment was hosted on Meteosat-P2, launched in 1988. Meteosat-P2 was a meteorological observation satellite in geo-synchronous orbit, with spin stabilization. Meteosat-P2 was also called Meteosat-3, and was originally an engineering unit of Meteosat-2. In 1991 it was positioned over the west Atlantic, were time transfer experiments were performed. It was retired in 1995. The space segment included an array of retro-reflectors, a detection unit, an event timer, and a clock. Users could measure the time difference between the on-board clock and their own by shooting a laser pulse at the payload and recording the time the pulse was transmitted. The space segment recorded the time according to its own when it detected the pulse. The pulse was sent back to the ground segment with a retro-reflector, where the time wasrecorded a third time, against the ground clock. The reference clock was an oven controlled quartz oscillator, and the event timer resolution was 69 ps. LASSO was compatible with both 694 nm, for Ruby lasers, and 532 nm, for Nd:YAG lasers. In 1992, the LASSO experiment demonstrated a common view time-transfer between the McDonald Observatory, at Fort Davis, Texas, an the station of the Observatoire de la Côte d'Azur (OCA), in Grasse, France. The residuals for time transfer with the satellite were below 300 ps, and the interval of confidence for the time difference between the two locations was around 100 ps (23).

2.1.4 MESSENGER

The MErcury Surface, Space ENvironment, GEochemistry and Ranging probe (MESSENGER) hosted an instrument called the Mercury Laser Altimeter (MLA) (24) (25). In May of 2005, while MESSENGER was in transit to Mercury, MLA was re-purposed to complete a ranging and time transfer experiment with a ground station at Greenbelt, Maryland and demonstrated

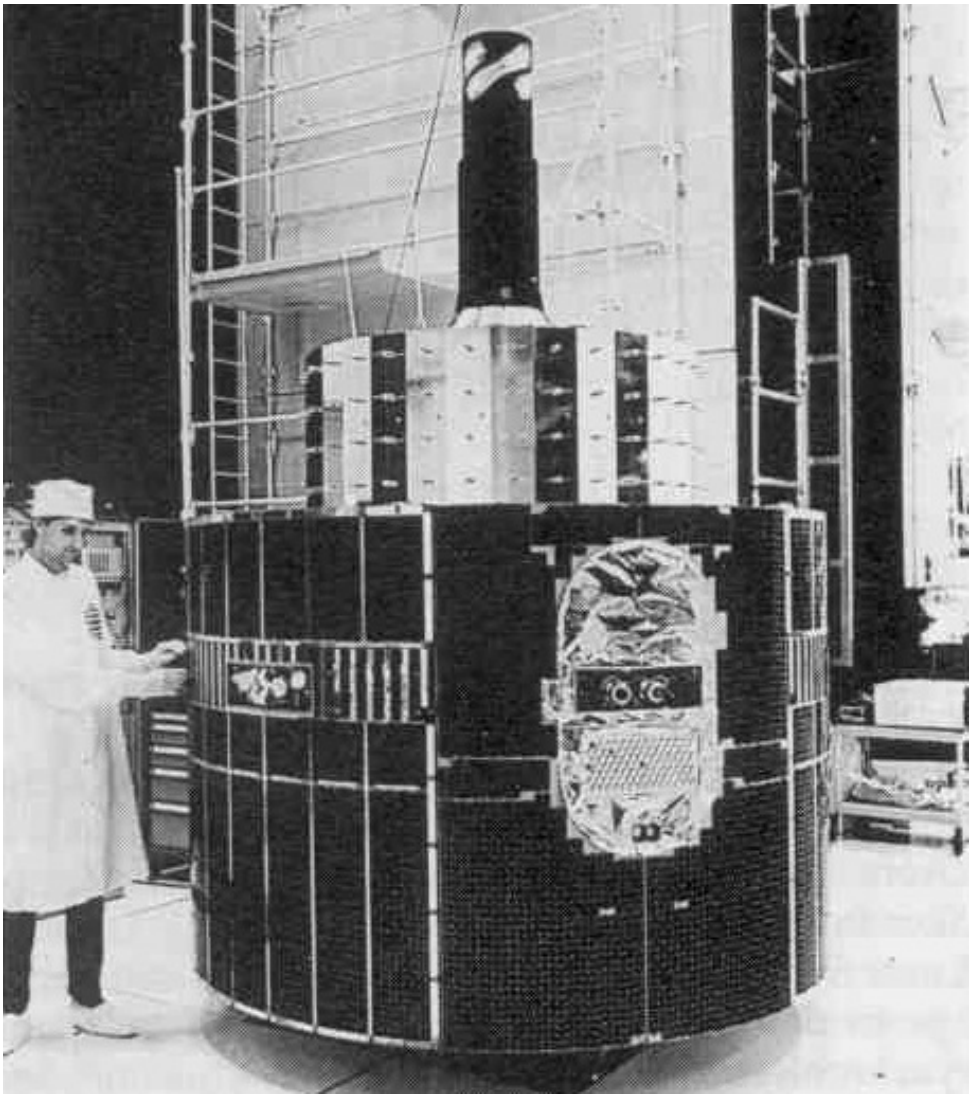

Figure 2-1. Meteosat-P2 satellite. The array of retro-reflectors and the apertures of the LASSO payload are on the right, on the main cylinder.

a two-way time transfer over 24 million kilometers. The residuals were of 390 ps on the downlink, and 2.9 ns on the uplink (26).

2.1.5 T2L2

Time Transfer by Laser Link (T2L2) is a time transfer system using the same concept as LASSO. It was first proposed in 1994, to be carried on a Russian meteorological satellite, Meteor-3M-1. The instrument was launched as a passenger of Jason-2 in 2008. T2L2 uses an oven-controlled quartz oscillator from the Doppler Orbitography by Radiopositioning Integrated

on Satellite (DORIS) payload as reference. T2L2 has two detectors. The first one is a linear Avalanche Photo-Diode (APD) operated in linear mode. It measures the received pulse energy and gates the other detector. The second detector is an APD in Geiger mode, which can count individual photons. The light sent to the Geiger APD is delayed with an optical fiber while a pulse is detected by the linear APD. The pulse energy measurement is used to correct the time-walk of the Geiger APD. The accuracy of the event timer on T2L2 is better than 2 ps (27). On ground, T2L2 achieved a single-shot time transfer accuracy between 3 ps to 35 ps, for 1 photon and 1000 photons respectively (28). From 2009, and as of early 2018, T2L2 has provided time transfer to around 30 ground stations, with an accuracy better than 100 ps and residuals of a few tens of picoseconds.

2.1.6 LRO

The Lunar Reconnaissance Orbiter (LRO), launched in 2009, included an instrument called the Lunar Orbiter Laser Altimeter (LOLA). One of the channels on LOLA was attached to a laser ranging telescope. This telescope was placed behind the RF high-gain antenna to be aligned with the ground station. The telescope was able to receive pulses from satellite ranging stations on earth. Its aperture was 19 mm (29). With 2 SLR facilities, LRO position can be estimated with precision even if no navigation systems are available around the moon. LRO performed one-way time transfer and ranging with a precision of 12.7 cm, or 424 ps (30).

2.1.7 LLCD

The NASA Lunar Laser Communication Demonstration (LLCD) was a payload on the Lunar Atmosphere and Dust Environment Explorer. LLCD demonstrated optical communications between Earth and Lunar orbit, this aspect is further discussed in chapter 3. LLCD also demonstrated ranging using optical pulses (31). The times of arrival of pulses on the uplink were measured by the payload using a phase detector, and thanks to a Phase-Locked-Loop (PPL) the pulses on the downlink were transmitted with the same time reference and known phase difference. LLCD achieved a time-transfer precision of $1\sigma = 44.3$ ps. With filtering, the ranging precision was below $1\sigma = 1$ cm.

2.1.8 ACES

Atomic Clock Ensemble in Space is a experiment sponsored by ESA. It aims at testing clock and time transfer technologies by flying a package with two clocks and a microwave time-transfer link. The two clocks are an active hydrogen maser (Space Hydrogen Maser, SHM) and a cesium fountain clock (Projet d'Horloge Atomique Par Refroidissement d'Atomes en Orbit, PHARAO). SHM will provide short term stability. ACES also includes a MicroWave Link (MWL), (32) and an optical time-transfer link called European Laser Timing (ELT). MWL uses a principle similar to TWSTFT, with modulated RF signals in the K_u-band and S-band. ELT is similar to T2L2 and aims at reproducing its performance, with reduced resources. ACES is scheduled for launch in late 2018 or early 2019. It will be deployed on the Columbus External Platform Facility on the International Space Station.

2.2 Concept Of Operation

The principle of the proposed instrument is nearly identical to the one of LASSO and T2L2, and its components are similar. The mission is called CubeSat Handling of Multisystem Precision Time Transfer (CHOMPTT) Its payload designed is called OPTI (Optical Precision Timing Instrument). The concept of operation for CHOMPTT and OPTI is shown in Figure 2-2. A Satellite Laser Ranging facility (SLR), on the ground, will emit a laser pulse and record the time of emission against its own clock. This time is noted t_0^{ground}. The pulse will travel through the atmosphere and space to the satellite and illuminate a photodetector. The photodetector will trigger a time-to-digital converter, recording the time t_1^{space} when the pulse was received at the spacecraft relative to its onboard clock. The pulse will also hit a retro-reflector sending a fraction of the pulse back in the same direction. The return pulse can be detected again on ground with a telescope and a photodetector, and the time is recorded as t_2^{ground}, against the ground clock. The pulse travels approximatively through the same distance on its way to the satellite and on the way back, so the time at which the pulse hits the satellite according to the ground clock can be approximated as $t_1^{ground} = \frac{t_0^{ground} + t_2^{ground}}{2}$. The time difference between the two clocks is then $\chi = t_1^{space} - t_1^{ground}$. A few relativistic effects

must be compensated, including the Sagnac effect. Corrections due to the distance between the space detector and the retro-reflector may also be required. Those terms can be accounted for with an extra term t_{cor}. The equation for time transfer becomes:

$$\chi = t_1^{space} - \frac{t_0^{ground} + t_2^{ground}}{2} + t_{cor} \tag{2–1}$$

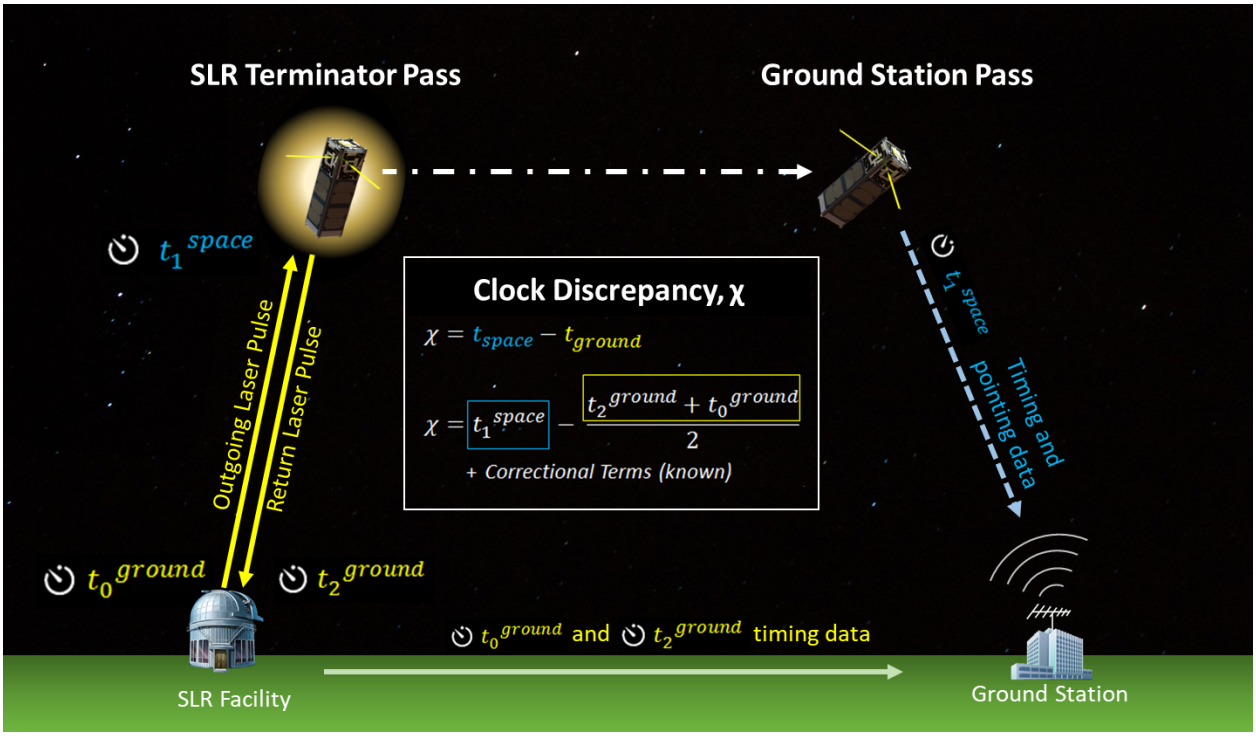

Figure 2-2. The CHOMPTT mission concept of operation. Image courtesy of Ahn Nguyen.

OPTI have been integrated into a 3U CubeSat, a small satellite of 10cm × 10cm × 30 cm. CubeSat are miniaturized satellites with standardized dimensions. They have rails on their edges, and can be launch into space as secondary payloads. They are fitted on launch vehicles in containerized deployment system to protect other passengers. The bus for the CHOMPTT mission have been provided by the NASA Ames research center. They also completed most of the work required for integration. The instrument and the on-orbit exploitation of the satellite is the responsibility of the University of Florida. CHOMPTT is expected to launch in May 2018.

This work will primarily deal with the space segment of the time transfer system, with a focus on detection, time-stamping and clock stability. On those aspects, the most advanced system currently in operation is T2L2, introduced in subsection 2.1.5. Compared to T2L2, OPTI is much more compact: one instrument channel, capable of time transfer on its own, fit within a volume of 10 cm by 10 cm by 2 cm. As shown later in subsection 2.5.1, the power consumption of one channel is under 5 W when active, and at 250 mW when counting. This well below T2L2 levels, of 42 W (28) when active, without accounting for reference oscillator. OPTI brings picosecond-range precision timing and centimeter level navigation in space, and does it with power, weight and volume requirements that are substantially lower than the previous missions. Although OPTI cannot reach the level of durability and reliability of large instruments like T2L2, the time transfer performance has not been sacrificed and is similar to T2L2, as discussed in subsubsection 2.5.2.5. Also, since the complete OPTI instrument includes two independent channels, it has the capability to compare its two clocks on-board, autonomously. The JASON-2 satellite carried only one high accuracy oscillator, so T2L2 cannot verify the stability of its oscillator without optical time-transfer.

2.3 System Architecture and Implementation

To apply the concept described in the previous section, the space segment needs a detector, a time-to-digital circuit capable of time-stamping the received pulses, and a clock. In the next subsections, we describe each of these elements, and explain the design choices. The design of OPTI has evolved through the project, following the development cycle but also because of changing requirements and corrections. OPTI went through 4 iterations: OPTI1 (breadboard), OPTI 2 (first engineering unit), OPTI 3 (second first engineering unit) and OPTI 3.1 (flight unit). The changes between those versions are also discussed in this section.

2.3.1 Electro-Optical Conversion

OPTI utilizes Avalanche Photodiodes (APD) to detect the light pulses emitted from the SLR facility. Other fast direct detection technologies include Photo-Multiplier Tubes (PMT), Microchannel Plates (MCP), Superconducting Nanowire Single Photon Detectors

(SNSPD), and PIN photodiodes. Photo-multipliers offer both high gain and good bandwidth but can be fragile and cumbersome in the reduced volume of a CubeSat. MCPs offer excellent performance but require very high bias voltages, beyond 1kV. As of this writing, SNSPDs offer the best performance in single photon detection, with jitter below 15 ps (33). SNSPDs also have excellent quantum efficiency and outperform avalanche photodiodes for infrared wavelengths. However, they require a cryogenic system, not compatible with the volume and cost requirements of the mission. PIN photodiodes are linear devices and have the highest bandwidth, but compared to the other technologies listed here, they lack internal amplification.

APDs have been selected for OPTI because they offer amplification at the required bandwidth, and because they impose reasonable constraints on volume, power and complexity. Since they are solid state devices, they are less sensitive to launch vibration, as opposed to PMTs. The bias voltages that they require range from 40 V for some InGaAs (Indium, Gallium, Arsenic) devices up to 300 V for Si (Silicon) devices. This range is easier to manage in a small volume. APDs can be used in linear mode, where the output current is proportional to the received light, or in Geiger mode, where a single photon can trigger an avalanche response measurable in the macroscopic scale. In Geiger mode, APDs are operated at biases beyond their breakdown voltages. The avalanche, once triggered by a photon, must be quenched either with a resistor, or an active component. APDs in Geiger mode can also be triggered without a photon, the measured pulse is then called a dark count. They also need a certain amount of time, typically a few nanoseconds, before receiving another photon. This delay is called dead-time. The dead-time is longer with passive quenching, using resistors.

Two wavelengths have been considered for the optical link, 1064 nm and 532 nm. 1064 nm correspond to the output of Nd:YAG lasers, and 532 nm pulses are obtained from the same lasers with frequency doubling. Q-switched Nd:YAG lasers offer high peak power, this make then them the preferred option for satellite ranging applications. 1064 nm have been selected for the CHOMPTT mission for cost and simplicity reasons.

To detect pulses at 1064 nm, various type of APD can be selected. Both InGaAs and Si devices can be used with that wavelength. Si detectors often give higher gain, sometimes beyond $M = 100$, while InGaAs detectors are limited to gains of 20 to 40. The quantum efficiency of Si devices is low at 1064 nm, below 40% even for Near-Infrared (NIR) enhanced devices. The OPTI design has used different variations of APDs through the various generations of hardware. OPTI 1, the breadboard demonstrator, used (NIR) 200 um Si APDs, without thermal control or integrated amplification. OPTI 2, the first complete instrument prototype, was designed while the characteristics of the SLR facility were still evolving and was fitted with both Si and InGaAs APDs, to detect both 1064 nm from Nd:YAG lasers, and 532 nm from frequency doubled lasers. The detectors have an integrated amplifier and an external thermo-electric cooler module. OPTI 3 and OPTI 3.1 were only built with InGaAs detectors. They are still compatible with Si devices. The detectors in the third generation devices do not have integrated amplifiers, but do have internal thermo-electric coolers. Through all the revisions, the APDs are operated in linear mode.

2.3.2 Timing Chain

The timing chain for OPTI relies on two components: a TDC to measure time intervals with high precision, and a counter for long term time keeping. The selected TDC is an ASIC, the TDC-GPX, manufactured by ams AG. The TDC-GPX is operated in M-mode. In this mode, it has a resolution of less than one picosecond, and an advertised precision of 10 ps, measured to 12 ps in laboratory tests. The INL, from Equation 1–16, is below 80 ps. The TDC is limited to a range of 7 μs (34), so another device is required to keep track of time. This is done with a 16 bit counter, clocked at 10 MHz. The counter is an integrated peripheral of the instrument micro-controller, a Texas Instruments MSP460F2618 (35). The counter overflows every $2^{16}/10$ MHz $= 6.6$ ms, and the micro-controller software counts the number of overflows in a 32 bit integer. This allows OPTI to keep track of time for 325 years.

The TDC and the counter must be synchronized. From OPTI 2 to OPTI 3.1, this is done with a set of D-latches. The signal from photodetection is first sent to a fast comparator with

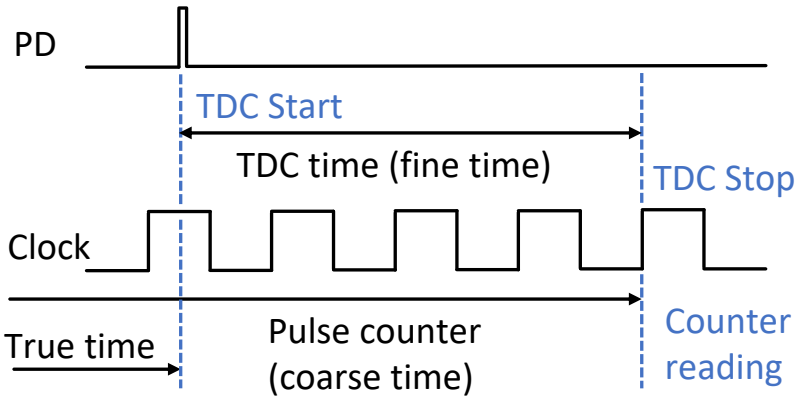

Figure 2-3. Synchronization of Time-to-Digital and counter times

an adjustable threshold. The signal is then split and distributed to two data-type latches. One detects the rising edge of the pulse and the other one the falling edge. The synchronization of the counter and the TDC, and the chronology of start and stop events, is shown in Figure 2-3. The rising edge latch triggers the start input of the TDC. This is the beginning of the fine time in Figure 2-3. The start input also enables a counter in the TDC called the M timer. The M timer is set to a few clock cycles. Once the M timer expires the TDC will set an output pin high, which will at the same time enable a third latch connected to the reference clock, and allows the micro-controller counter to be sampled on the next clock rising edge. When the next clock edge arrives, the counter is sampled and the Stop2 input of the TDC is triggered. The counter value is the coarse time of Figure 2-3, and the Stop2 input mark the end of the fine time The pulse duration is equal to $t_{Stop1} - t_{Start}$ and the fine time is $t_{fine} = t_{Stop2} - t_{Start}$. The true time of arrival of the pulse can be calculated as:

$$t_{true} = (N_{overflow} \cdot 2^{32} + N_{counter})100 \text{ ns} - t_{fine} \quad (2\text{–}2)$$

The M timer allows several clock periods to be skipped before Stop2 is asserted, so that non-linearities due to the start input disturbances are minimized.

When the amplitude of the received pulses changes, the recorded timestamps are also affected. This is illustrated in Figure 2-4. A pulse with a smaller amplitude will be detected by

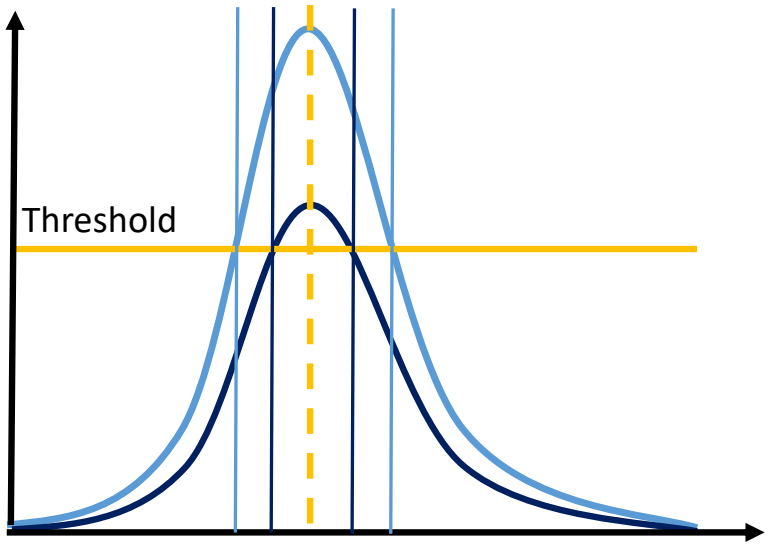

Figure 2-4. Effect of pulse amplitude on timestamps

the comparator later, and its duration will appear smaller. The TDC has a second stop input noted Stop1. This stop pin is connected to the detector, and is sensible to the falling edge of pulses. With the Stop1-Start interval the instrument can measure pulses duration. It can also account for the time walk by using the average between the rising edge and the falling edge for each pulse. The timewalk correction depends of the pulse shape and should be adapted to the laser at the ground station.

2.3.3 Clock

Two clocks have been considered for OPTI: The Chip-Scale Atomic Clock (CSAC) (12) and the Miniature Atomic Clock (MAC). Both clocks are produced by Microsemi, and they both are beam atomic clocks. The CSAC uses cesium as a reference, and consumes 120 mW in normal operation. The MAC is more accurate, but consumes 5 to 15 W. It uses Rubidium. The frequency stability of both clocks is shown in Figure 1-2. They both have a 10 MHz output frequency.

2.3.4 Support Functions

The instrument requires a certain number of supporting circuits. The most important ones are a Thermo-Electric Cooler (TEC) controller and an high voltage bias supply for the APD.

The TEC controller uses an analog PID controller with a PWM power stage implemented in a single chip, and the bias supply is based on a controlled transition switching regulator with a transformer (36). The bias supply is capable of providing up to 300V to be compatible with silicon APDs. The power converters and the power distribution tree of the instrument includes several current-limiting load switches to provide some protection against radiation-induced latch-up.

2.3.5 Evolution of the Architecture

The instrument went through 4 revisions. OPTI 1, in figure 2-5A, is the breadboard, and was used to prove the feasibility of the concept and gain initial experience with the components of the system. OPTI 2, in figure 2-5B, was the first prototype for a flight instrument. Although OPTI 2 demonstrated its ability to detect and time pulses, soon after the first demonstration, the payload was required to integrate with a different bus, with a lower average power available. OPTI 3 was designed to lower the power consumption while counting clock cycles. OPTI 3.1 improved the layout of OPTI 3 with minor circuit corrections.

2.3.5.1 OPTI 1

OPTI 1 was used to validate the concept and the selected components. To be flexible, the electronics were spread across different boards. Detector boards included a 200-um silicon APD, the high-voltage bias supply for it, an amplifier, a comparator, and coaxial cable drivers. The bandwidth of the boards was higher than 300 MHz. The TDC and the controller were implemented on another board. The block diagram for this board is shown in Figure 2-7, and Figure 2-6 is a picture of it. This generation did not include latches and had troubles with TDC and counter synchronization. Post-processing was required to solve an ambiguity of one clock cycle (100 ns) due to this issue. The detector boards were robust, but needed a lens in order to close the link during the first table-top demonstration. Both t_1^{space}, at the satellite side, and t_2^{ground}, receiving return pulse on the SLR side, received unfocused light and needed a lens to operate with the reduced power of the test laser diode.

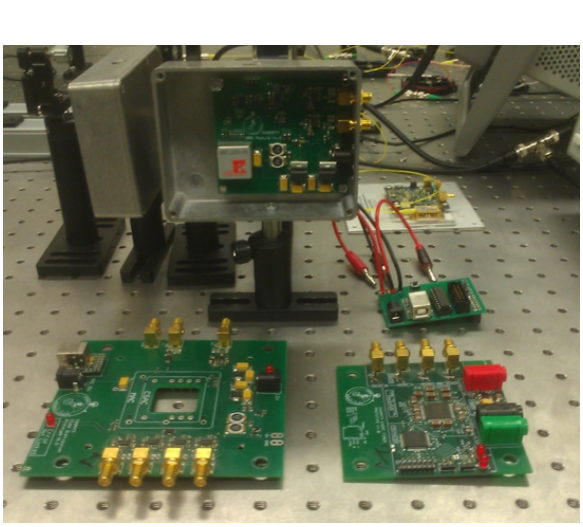

A

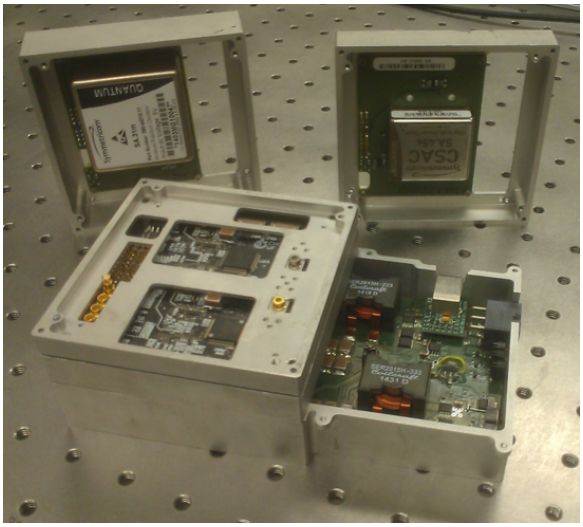

B

C

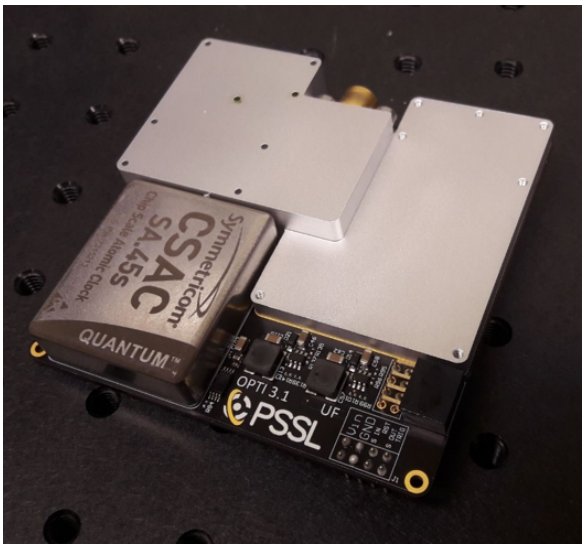

D

Figure 2-5. OPTI revisions: A) OPTI1 (breadboard), B) OPTI 2 (first engineering unit), C) OPTI 3 (second first engineering unit), D) OPTI 3.1 (flight unit). Photo A, B and D courtesy of author. Photo C courtesy of Seth Nydam.

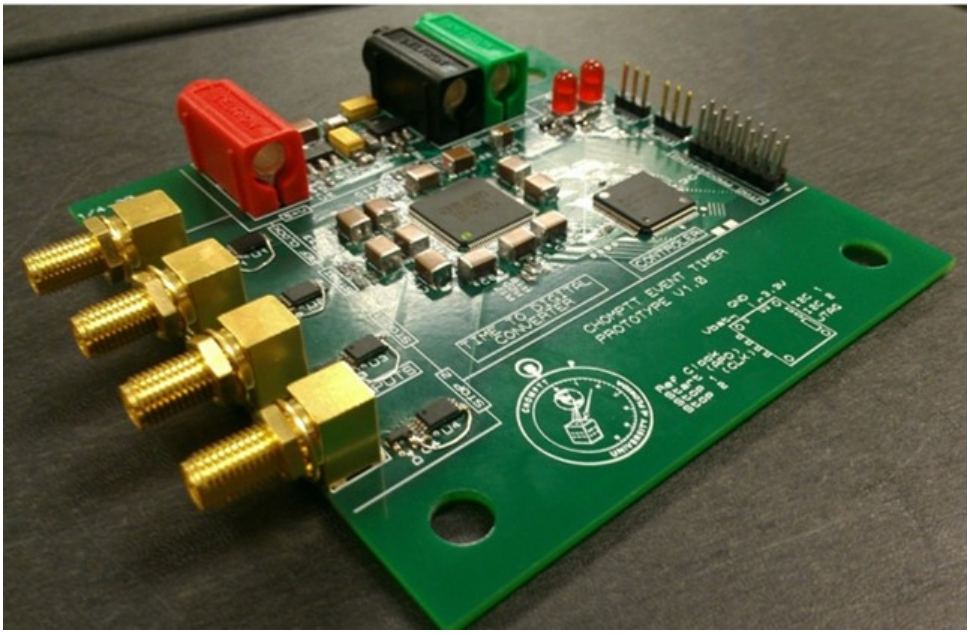

Figure 2-6. Event Timer electronics board of OPTI 1. Photo courtesy of author.

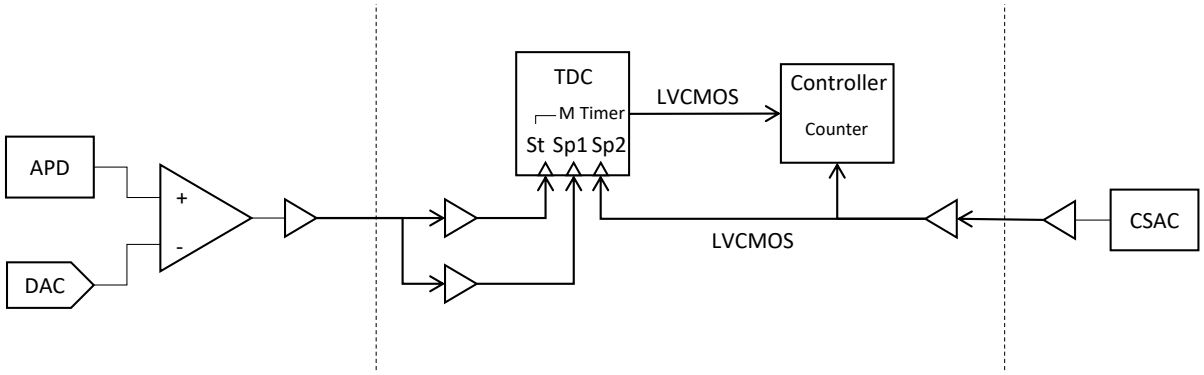

Figure 2-7. OPTI 1 measurement chain configuration

2.3.5.2 OPTI 2

OPTI 2 was the first engineering unit of the project. Figure 2-8 shows a cross-section of the design. Only one was fabricated. It was designed with high flexibility in mind. As shown in Figure 2-9, any APD and any clock could be connected to one of two event timer cores. A silicon and an InGaAs APD with integrated transimpedance amplifiers were installed, which allowed the payload to perform time transfer using both 532 nm and 1064 nm pulsed lasers. Both the MAC and the CSAC were available as references and could be distributed in any configuration. The instrument recorded both the rising and the falling edges of the pulses to

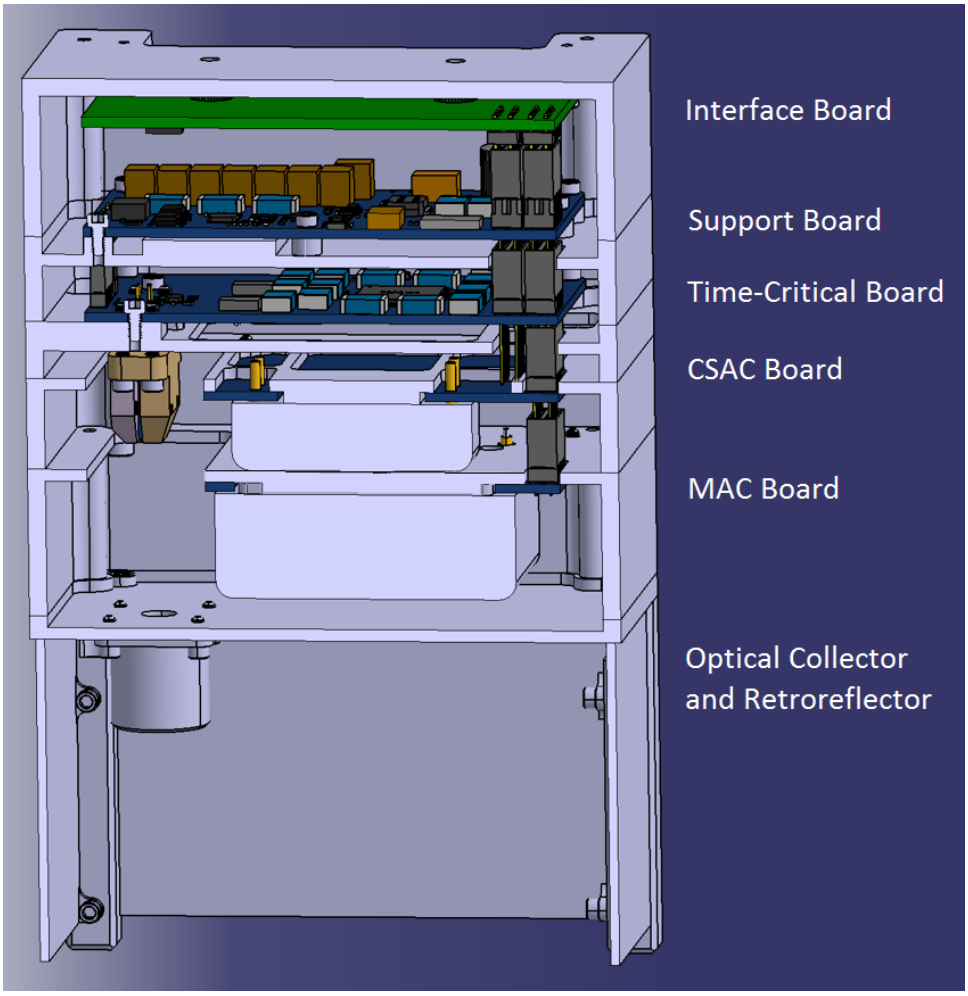

Figure 2-8. Section view of OPTI 2. The retro-reflector is not shown. Image courtesy of author.

correct for variations of pulse amplitude, an effect called time-walk. This version achieved basic functionality. Soon after, a change in the CHOMPTT mission required the instrument to be adapted to a different satellite bus, with less average power available. The orbit average power available on the new bus was around 2W. Out of those 2W, a large fraction was needed by the bus itself. The flexibility of OPTI 2 became a liability, because the integrated circuit used for clock distribution consumed too much power. This IC, the CDCE62005, must stay activated while counting clock cycles, so the power draw is constant. The CDCE62005 consumes 0.75 W with all outputs disabled, and was consuming more than 1.6 W when the payload was counting clock cycles. This circuit could be replaced without a major redesign of the instrument

architecture. Also, the high power consumption of the MAC made it impractical with the new satellite bus.

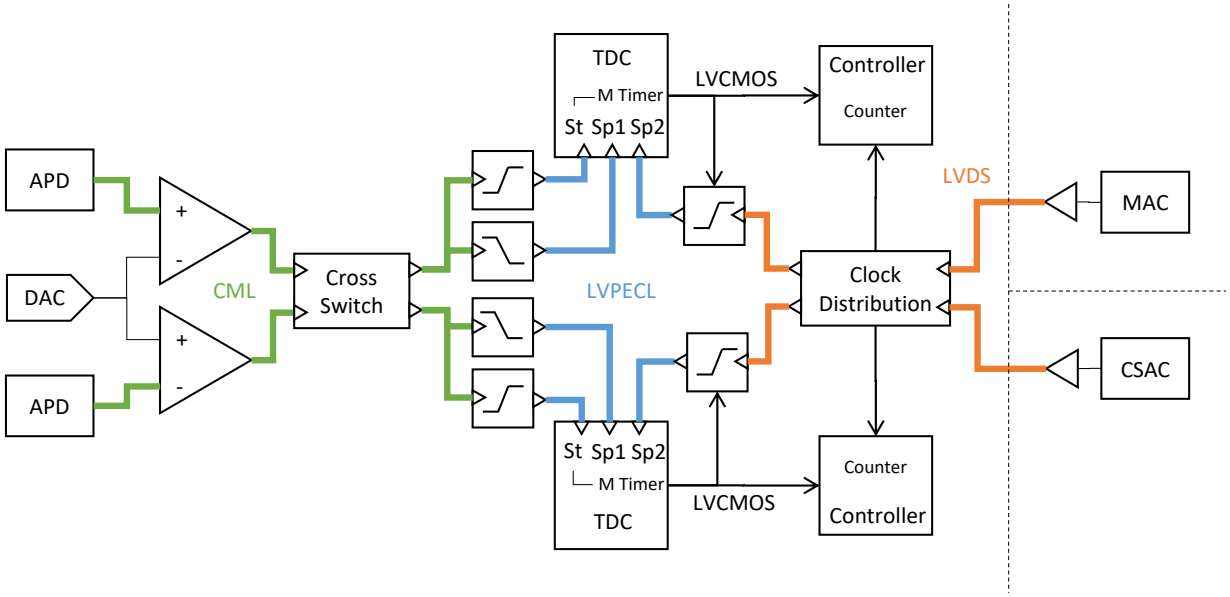

Figure 2-9. OPTI 2 measurement chain configuration

2.3.5.3 OPTI 3 and 3.1

OPTI 3 and OPTI 3.1 are almost identical. The layout of OPTI 3.1 is more refined, and compatible with the mechanical design of the instrument. Both OPTI 3 and 3.1 achieved basic functionality at the desired accuracy, but some sub-circuits were not tested on OPTI 3. Figure 2-10 is the block diagram of the OPTI 3 channels. The two sides have been separated, and are now identical boards with no crosslinks. The flexibility of the instrument is reduced compared to OPTI 2, but the power efficiency has been greatly improved, and the electronics are more compact. OPTI 3.1 is the final flight version for the CHOMPTT mission. Four instrument channels have been fabricated and tested. Two of them are engineering units and two are flight boards. Repairs have been conducted on each board, to correct two pin swaps and to add a passive filter on the TEC controller.

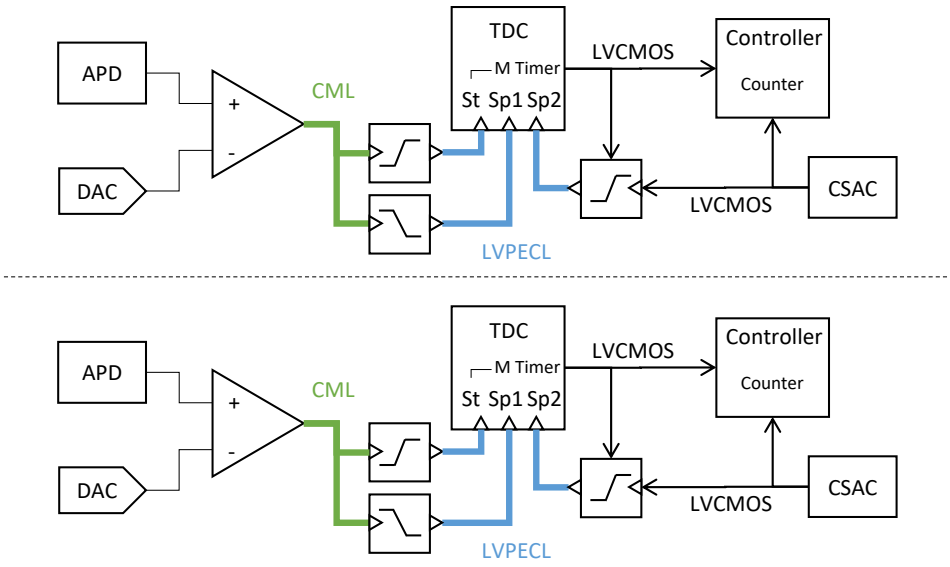

Figure 2-10. OPTI 3 measurement chain configuration

2.4 Pulse Identification

In order to identify triplets of time t_0^{ground}, t_1^{space} and t_2^{ground}, we need to encode a known signal into the laser trigger times. This section discusses a method to create that signal and match the pulses. The performanceof this approach are estimated through a simulation.

2.4.1 Range Error

The pulse energy of high-power Q-switched lasers depends on the time spent by the emitted pulse in the cavity. Because of that, the laser period has a direct impact on the output peak power. To keep the pulse amplitude variation of the laser low, we limit the period variation to 1%. The laser pulse period is noted T_{laser}. At 50 Hz:

$$\frac{t_{ModMax}}{T_{laser}} = 1\% \qquad t_{ModMax} = 200\ \mu\text{s} \tag{2–3}$$

Range variations are more pronounced at higher orbits. With a 500 km orbit:

$$r_{min} = h = 500\ \text{km} \qquad r_{max} = \ sqrt(r_\oplus + h)^2 - r_\oplus^2 = 2573\ \text{km} \tag{2–4}$$

In Equation 2–4, r_{min} is the minimum distance to the satellite, r_{max} is the maximum distance, when the satellite is at the horizon, and $r_\oplus$ is the radius of the Earth. The variation in the time-of-arrival is:

$$\Delta t_{pass} = \frac{r_{max}}{c} - \frac{r_{min}}{c} = 6 \text{ ms} \tag{2–5}$$

This is larger than the modulation limit. Therefore, we need to account for the expected time of arrival and create a cross-correlation function that is adjusted for it. However, this is lower than $T_{laser} = 25$ ms. Therefore, we don't need to consider it to correlate the ground and space timestamps. The satellite is traveling at a constant speed because the orbit is circular. The range rate is at its maximum when the velocity vector of the satellite is closely aligned with the vector from the satellite to the ground station. This happens at the horizon on a pass that is going over the ground station. The unit vector from the satellite to the ground station is noted $\vec{e_r}$.

$$\dot{r} = \vec{v} \cdot \vec{e_r} = \sqrt{\frac{GM_\oplus}{r_\oplus + h}} cos\left(\frac{\pi}{2} - sin^{-1}\frac{r_\oplus}{r_\oplus + h}\right) = \frac{r_\oplus}{r_\oplus + h}\sqrt{\frac{GM_\oplus}{r_\oplus + h}} \tag{2–6}$$

$$\dot{r}_{min} = 0 \text{ km.s}^{-1} \qquad \dot{r}_{max} = 7.06 \text{ km.s}^{-1} \tag{2–7}$$

With a 50 Hz repletion rate, the variation of the time interval between two pulses is, at most:

$$\Delta t_{p-p} = \frac{\dot{r}_{max} T_{laser}}{c} = 471 \text{ ns} \tag{2–8}$$

If the modulation applied to the laser has a resolution close or below this value, then the range rate must be compensated to get a satisfying correlation.

2.4.2 Encoded String

We want a string of time-shifts with the following properties: Long enough for a 15 minutes pass (45000 samples), Random or semi-random, in order to avoid aliases or artifacts and avoid auto-correlation, Depth of $t_{Mod} = 200$ µs. A way of generating such a string is to randomly pick all integers once in $[\![1,45000]\!]$. Those integers are noted $s(i)$ with i from 1 to 45000. The integers are inserted in the following formula to get the desired depth for the

modulation of the laser period:

$$T_{mod}(i) = \left(1 - \frac{s(i-1)}{45000} t_{ModMax}\right) + T_{laser} + \frac{s(i)}{45000} t_{ModMax} \tag{2–9}$$

In Equation 2–9, $T_{mod}(i)$ is the period between the pulse number $i-1$ and the pulse number i. $T_{mod}(i)$ is equal to the nominal pulse period T_{laser}, plus the deviation of next pulse, minus the deviation of the previous pulse. The time of emission of each pulse is then:

$$t_0(i) = t_{epoch} + \sum_{k=1}^{i} T_{mod}(k) \tag{2–10}$$

The smallest possible encoded interval is:

$$t_{LSB} = \frac{t_{ModMax}}{45000} = 4.44 \text{ ns} \tag{2–11}$$

This is well above the expected resolution of the system. This method gives us 45,000 different encoded intervals, and we can identify any of these intervals with our current system, on ground. However, since Δt_{p-p} is larger than t_{LSB}, the change in range $\dot{r}$ can induce an error that is large enough to require compensation.

2.4.3 Range-Corrected Cross-Correlation Function

To correct for the range rate induced variation in the timestamps, we must modify the usual definition of a cross-correlation function. As explained in the concept of operation, we record t_0 and t_2 at the ground station for all the pulses emitted. Some return timestamps t_2 could be missing, depending on the link conditions. The timestamp t_1 is recorded by the CubeSat only for some of the emitted pulses. We could calculate the expected time of arrival of the pulses t_{1g}, at the CubeSat according to the ground clock. However, we would have issues with the normalization of t_{1g} and t_1, and this step is required to extract a cross-correlation. Instead, from $t_0(k)$ and $t_2(k)$, we can find the range, and a time correction for the range $t_c(k)$. With no consideration for the relativistic or atmospheric effects:

$$t_c(k) = \frac{t_2(k) - t_0(k)}{2} \qquad k \in [\![1, size(t_0)]\!] \tag{2–12}$$

Note that since the emitted and return pulses travel on approximatively the same path, atmospheric effects should be negligible. The correction term $t_c(k)$ is intended to correct one of the CubeSat timestamp $t_1(j)$, such that $t_0(k) \approx t_{0c}(j) = t_1(j) - t_c(k)$, when k and j are for the same pulse: k is the index of the pulse on ground, j is the index of the same pulse according to the CubeSat. The continuous increase of $t_0(k)$ as time is passing can be canceled by subtracting the expected value of the time increment:

$$t_{0i}(k) = t_0(k) - k(T_{laser} + t_{ModMax}) \tag{2–13}$$

And then partially normalized:

$$t_{0n}(k) = t_{0i}(k) - \langle t_{0i}(l) \rangle_l \tag{2–14}$$

Similarly, with the CubeSat times:

$$t_{0gi}(j,i) = t_{0g}(j,i) - j(T_{laser} + t_{ModMax}) \tag{2–15}$$

$$t_{0gn}(j,i) = t_{0gi}(j,i) - \langle t_0 gi(m,i) \rangle_m \tag{2–16}$$

Finally, the cross-correlation can be computed:

$$C_{t_0,t_0g}(i) = \langle t_{0n}(j+i)\, t_{0gn}(j,i) \rangle_j \tag{2–17}$$

C_{t_0,t_0g} should be maximal when offsets i and j are matching, and close to zero when pulses are not aligned correctly.

2.4.4 Simulation of pulse identification

To demonstrate the performance of this timestamp correlation algorithm, a time-transfer pass have been simulated. Timstamp have been randomly deleted on both the CubeSat and on the ground, for the return pulse.Figure 2-11 shows the results of the correlation function TC_{t_0,t_0g}, with a Gaussian time-transfer noise of 500 ps. The correct offset corresponds to the maximum of the correlation function. The maximum can be found reliably if at least 50 triplets are recorded. Therefore, in order to appropriately match the pulses, the instrument

must successfully perform time transfer operations for a total of one second out of a 10 minute pass over the SLR facility. This one second time interval does not need to be continuous, the 50 timestamp triplets can be acquired at any time during the pass.

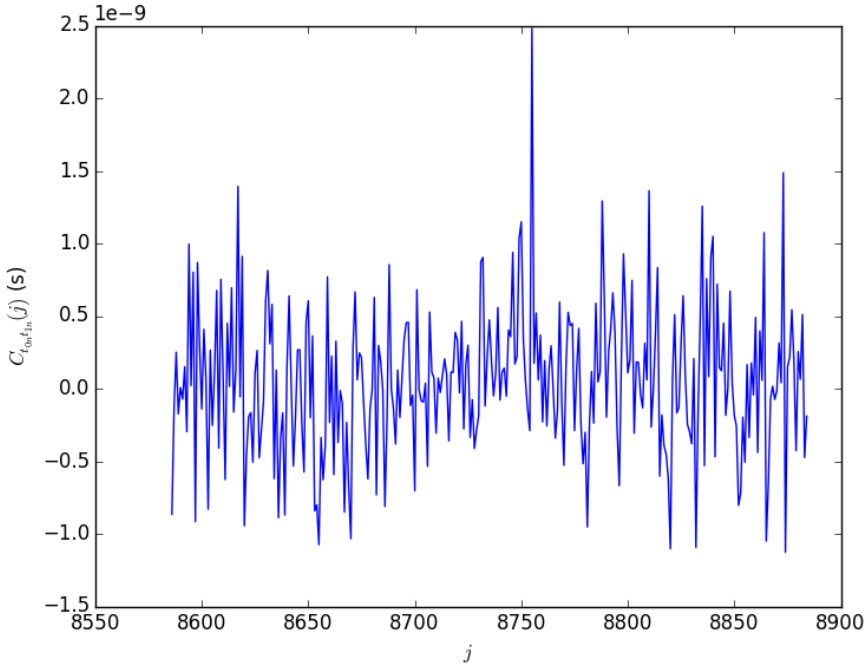

Figure 2-11. Correlation for 50 non-consecutive t_1 pulses, with 500 ps of noise

2.5 Measured Performance

Over the duration of the project, various tests have been conducted either to validate some aspect of the mission, or check the functionality and performance of successive hardware revisions. The timing errors of OPTI 1 has been analyzed in details (20). The data presented and interpreted in this section has been collected on the final revision of OPTI, the flight boards. It verify whether OPTI 3.1 meets the CHOMPTT mission requirements in term of accuracy and power, or not.

2.5.1 Proto-flight unit power consumption

The flight board's power consumption has been tested and is plotted against time in Figure 2-15. The three different modes, counting, self-test, and time-transfer, are indicated in blue.

In counting mode, only the clock (the CSAC), the micro-controller, and a house-keeping ADC are turned on to conserve power as much as possible. In order to keep track of time, the instrument must stay in counting mode between time-transfer operations, so its power consumption must be as low as possible. On OPTI 3.1, the counting mode consumed less than 250 mW with the initial software revision.

Next is the self-test mode, In this mode, the TDC and its input circuits are turned on, but the detector bias and thermal control are shut-down. The TDC can receive electrical triggers, from both external test inputs and the control connector. This mode allows testing of the TDC and the clock. With both instrument channels, it is possible to measure the Allan deviation between the two CSACs of the spacecraft. In his mode, the power consumption is around 1.5 W.

After that, around 7 minutes and 30 seconds on Figure 2-15, at TEC On, the TEC controller is turned on, set to a target temperature and then enabled. One minute later, at HV On, the bias supply is turned on, and finally, at HV Set, the bias supply is set to its target voltage. Once the bias is applied, the instrument is ready for time transfer. All the functions of the board are enabled at that time. The power consumption depends on temperature. It is below 4.5 W for a instrument case temperature below 35 degree Celsius.

The power consumption in counting of OPTI 3 and OPTI 3.1 is a large improvement over OPTI 2, were the consumption was higher than 2 W for the same task. With a power below 250 mW, an OPTI channel can keep counting continuously, since the bus is generating 2 W on average. In time-transfer configuration, the power used by OPTI 3.1 is one order of magnitude below the consumption of T2L2, which is 42 W (28).

2.5.2 Proto-flight unit optical test

The flight instrument (OPTI 3.1) have been used to validate the performance of the instrument, using the setup shown in **??**. Earlier tests on OPTI 1, described in (20), had already validated the principle and the basic performance with a similar instrument configuration. The set-up used in the following test is described in Figure 2-13. A function

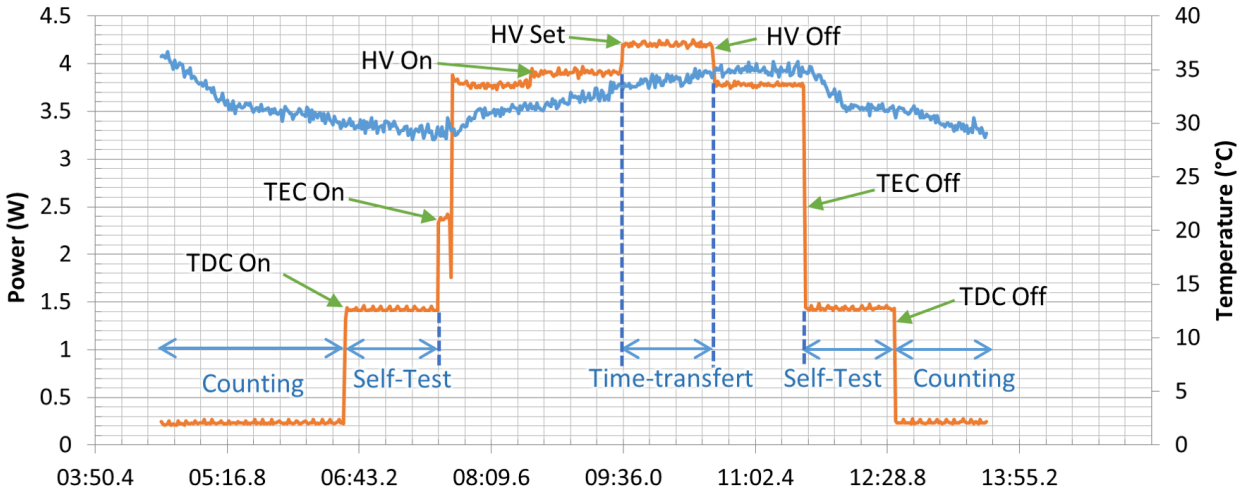

Figure 2-12. Power and temperature of the flight instrument through various modes

generator uses a 10 MHz reference from an atomic clock and generates a 1 Hz signal. This signal is sent to a laser driver which generates nanosecond pulses at 1064 nm. Unlike this set-up, the experiment conducted in reference (20) also recorded the pulse emission time t_0, and the return time t_2. By recording those two times, the errors due to the laser driver and the signal generator can be factored out.

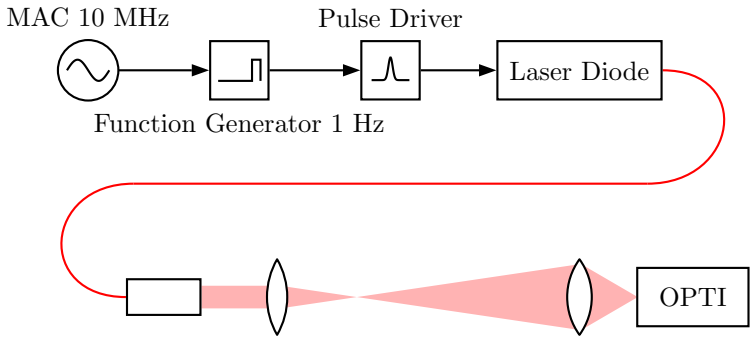

Figure 2-13. OPTI Test Setup Diagram

2.5.2.1 Time difference and clock stability

The pulses have been recorded on each channel, in two separated experiments, over 1 hour and 30 minutes. More than 5000 timestamps have been recored, and fitted to an order one polynomial. The residuals of this least-square fits are shown in Figure 2-15. The instrument channel including the clock, and the laser driver where not powered before the

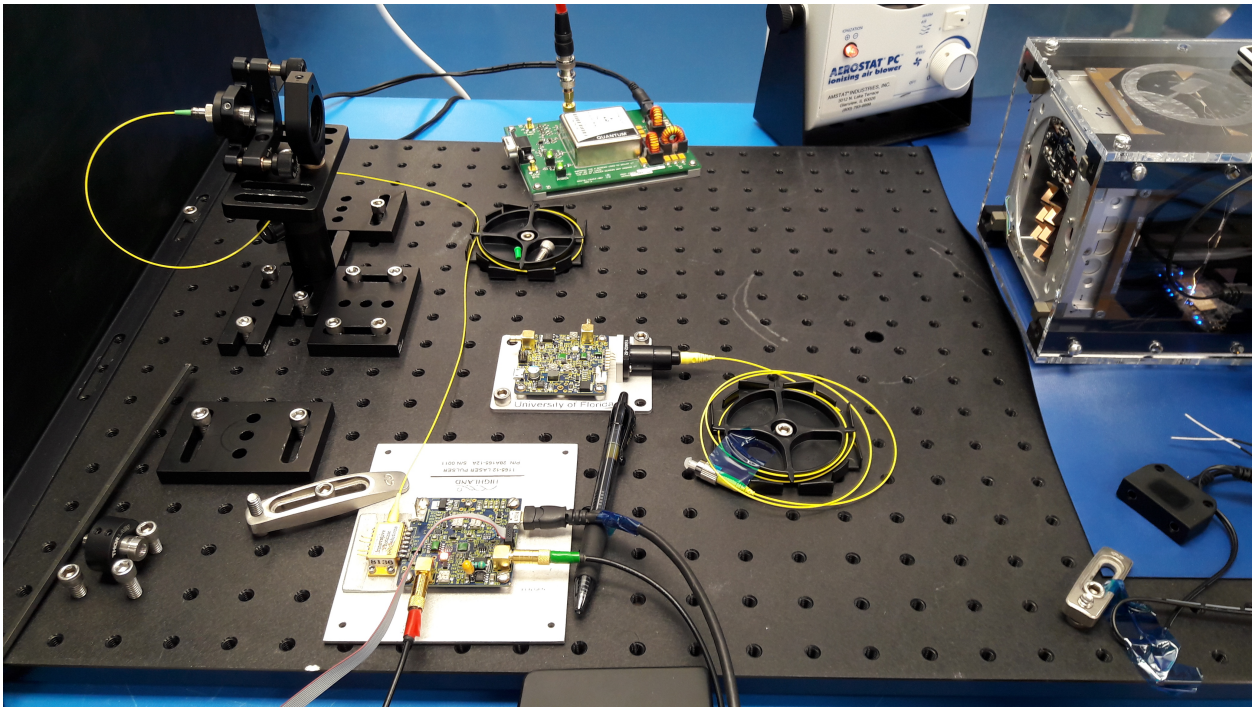

Figure 2-14. Test setup for OPTI in the clean room at University of Florida. Image courtesy of author.

experiment, and started cold, resulting in a rapid change of the time difference on Figure 2-15, in particular for channel 1.

The Allan deviation has been computed using Equation 1–8 and plotted in Figure 2-16. The CSAC specification is also plotted for comparison. The complete instrument including the clock and the time-stamping electronics is more stable than the CSAC specifications. The tails of the Allan deviations have not been removed. Although they have a diminishing statistical relevance as τ increase, they also show errors not due to the lack of samples. This is further discussed in subsubsection 2.5.2.5. For the test of channel 2, the detection threshold was set higher than required, on the top part of the pulse, where the signal slope is lower. This point will be developed in subsubsection 2.5.2.4

2.5.2.2 Pulse duration

Both the rising edges and the falling edges of pulses are recorded by the instrument. The histogram of pulses duration is plotted in Figure 2-17 for channel 1. The histogram is separated in 5 sections stacked together. Each section contains 1000 timestamps. Figure 2-17

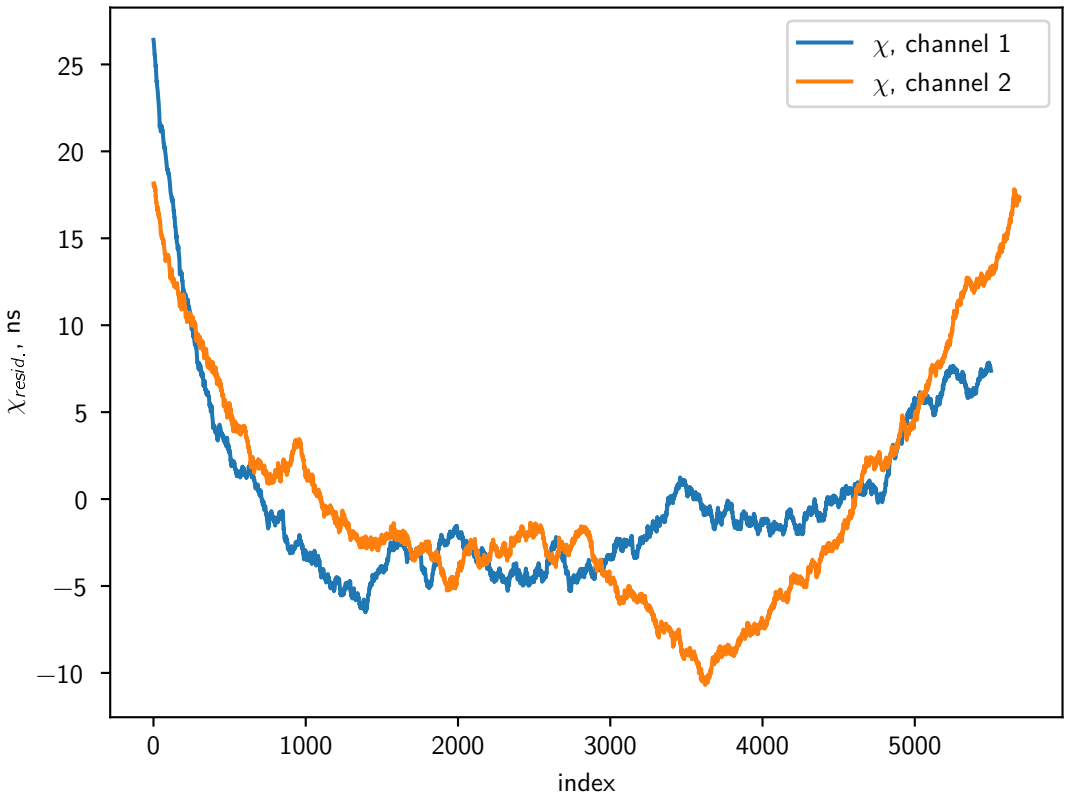

Figure 2-15. Time difference from both channels of the flight instrument

shows that the pulse duration was not constant through the test. The variation is larger than 200 ps from the beginning to the end of the test. Since none of the components on the detection chain have a variation of propagation delay due to temperature large enough to explain this effect, and since the temperature of the APDs is actively controlled, those variations are attributed to the laser driver and the laser diode, which are not controlled in temperature.

Several experiments can be performed to determine the origin of this variation. Recording the emitted pulse would allow to account for changes in the laser source, and this will be done for the on-orbit experiment. Probing the CSAC mounted on OPTI and using it as a reference for the function generator would remove errors due to the clock deviation. Each OPTI channel is equipped of three temperature sensors in order to calibrate temperature effects, and they can

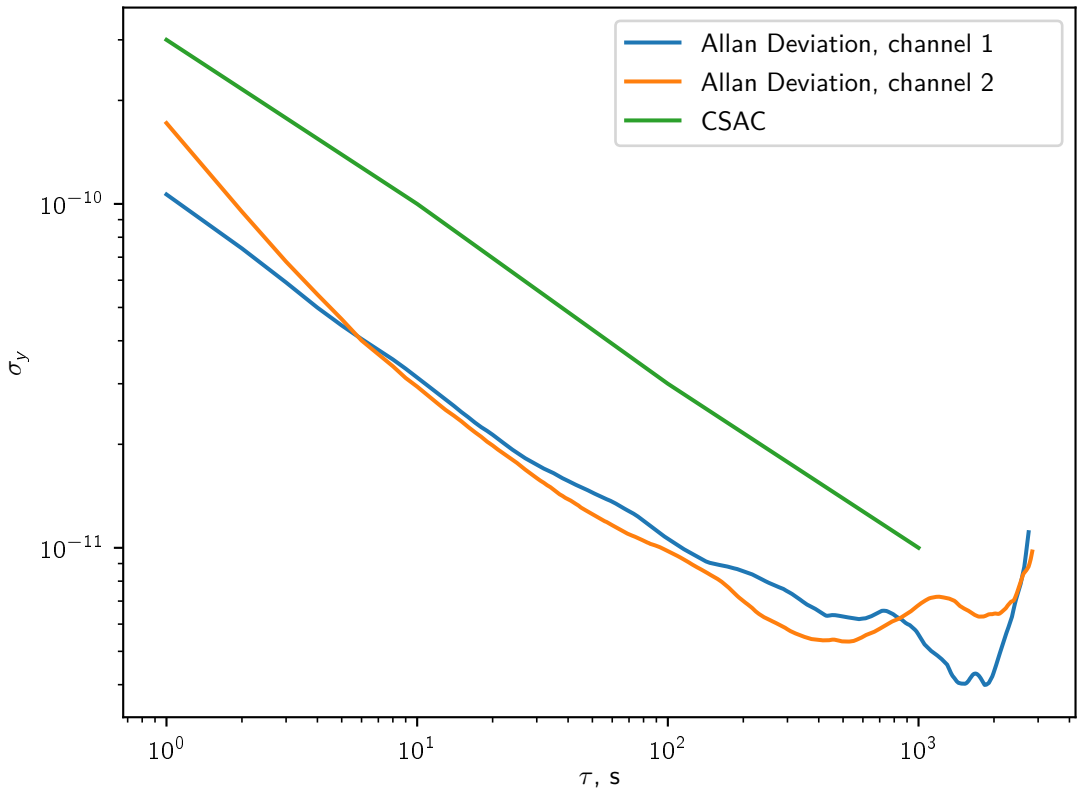

Figure 2-16. Allan deviation from both channels of the flight instrument

be used to estimate the temperature sensitivity of the instrument. Regardless of their origins, variations in the pulse duration can be accounted for with the same mechanism used for time walk.

2.5.2.3 Stability in nominal operating conditions

For channel 1, the detection threshold was set to a nominal value. As shown in Figure 2-18, the slope of the Allan deviation is close to $\tau \mapsto \tau^{-0.5}$. This is characteristic of white frequency noise (9), which is likely due to the clock. Time transfer operations provides an independent measurement of the phase, and exhibits white noise in phase with a slope of τ^{-1}. Thanks to Equation 1–13, the single time-transfer errors are estimated to be below 60 ps.

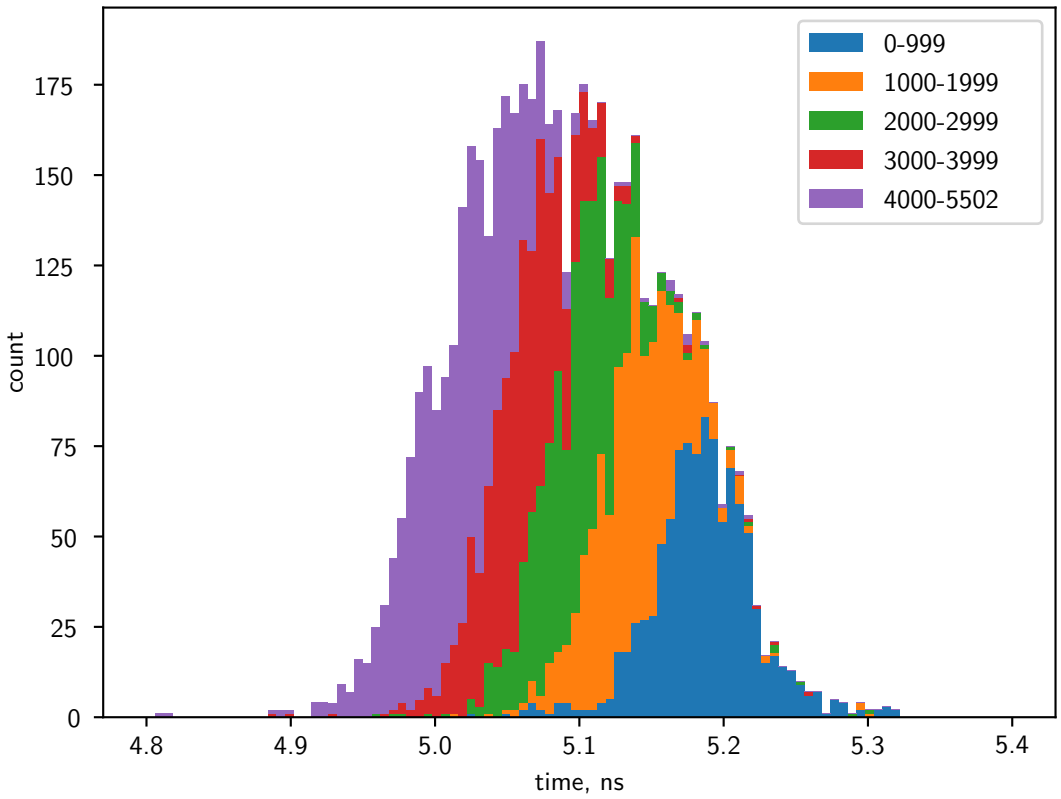

Figure 2-17. Pulse duration histogram from channel 1 of the flight instrument

2.5.2.4 Stability in degraded conditions

Figure 2-19 shows the Allan deviation in the case of higher than required thresholds. This simulates pulses with a lower light level and a higher noise without the constraint of adjusting the APD bias. The time-transfer error is then higher, and its slope of τ^{-1} is now apparent. With Equation 1–13, this error is estimated at 104 ps. The frequency noise, due to the clock, is still present as slightly lower levels, compared to channel 1.

2.5.2.5 Comparison with other missions

The data from the T2L2 mission is publicly available, and this enables a more complete comparison, using the same algorithms to process the data. The time-transfer pass selected was long, with a maximum elevation of 78 degrees, and done with a powerful station. The MeO SLR facility at Grasse (France) used in this pass is also capable of lunar ranging, and

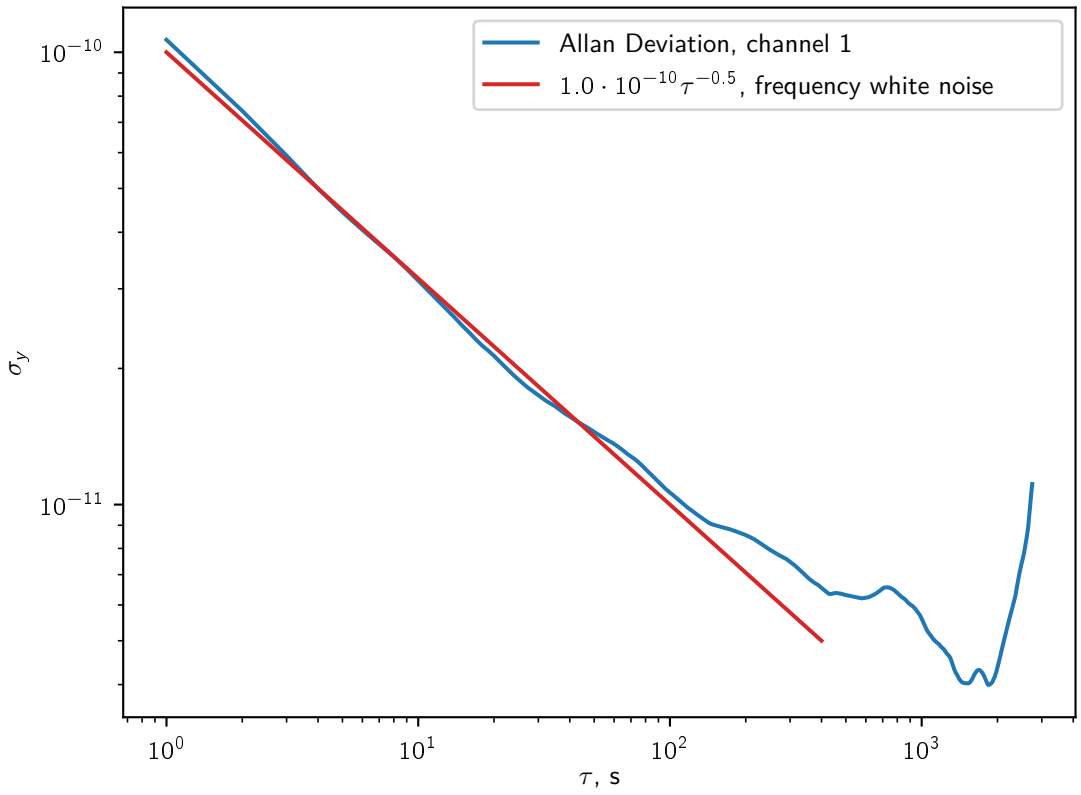

Figure 2-18. Model of the channel 1 results

was part of the calibration of T2L2. The residuals from this pass have been corrected for time walk, Sagnac effect, and the geometry of the spacecraft by the T2L2 Scientific Mission Center. Then, they have been inputed to the algorithm in Appendix A to obtain the Allan deviation, which is plotted in Figure 2-20. Lines with a slope of τ^{-1} have been added to represent T2L2 ground tests (28) and the RMS time-transfer performance of LASSO (23).

The long term stability of the T2L2 data shows that the time transfer errors dominate during the whole pass. Although the reference clock of T2L2 is a quartz oscillator, its stability is superior to the CSAC, a cesium atomic clock. This quartz oscillator, the DORIS USO, is larger and consumes more power than the CSAC. As for OPTI, the tail of the Allan deviation have been included. For large integration times, the Allan deviation of OPTI has a different

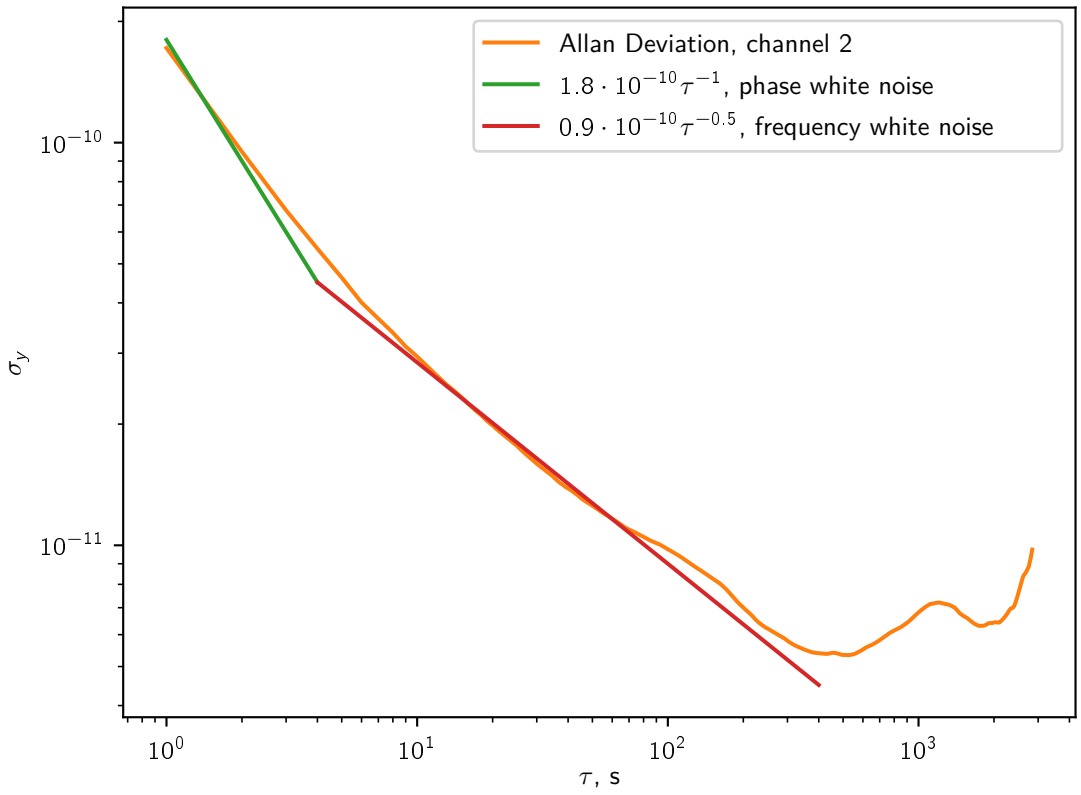

Figure 2-19. Model of the channel 2 results

aspect compared to the one of T2L2. The pulse duration was not constant for OPTI's test, and it is probable that a similar, slow phase wander affects the measured timestamps.

Figure 2-20 provides a validation of the instrument design, an explanation of its performance up to 100 s, and a comparison with previous experiments. The errors are below CSAC specifications at all times. As explained in subsubsection 2.5.2.3 and subsubsection 2.5.2.4, the $\tau^{-0.5}$ section of the curves are due to the clocks, and the τ^{-1} parts due to time-transfer.

Compared to LASSO, OPTI offers an improvement in terms of time-stamping accuracy and repetition rate, and is expected to perform better once on orbit. The resolution of OPTI's TDC is superior, and the low altitude of the CHOMPTT mission compared to LASSO's GEO orbit yield consequent advantages in term of link budget. Compared to T2L2, the time-transfer performance is expected to be similar. The T2L2 event timer is much more capable than the

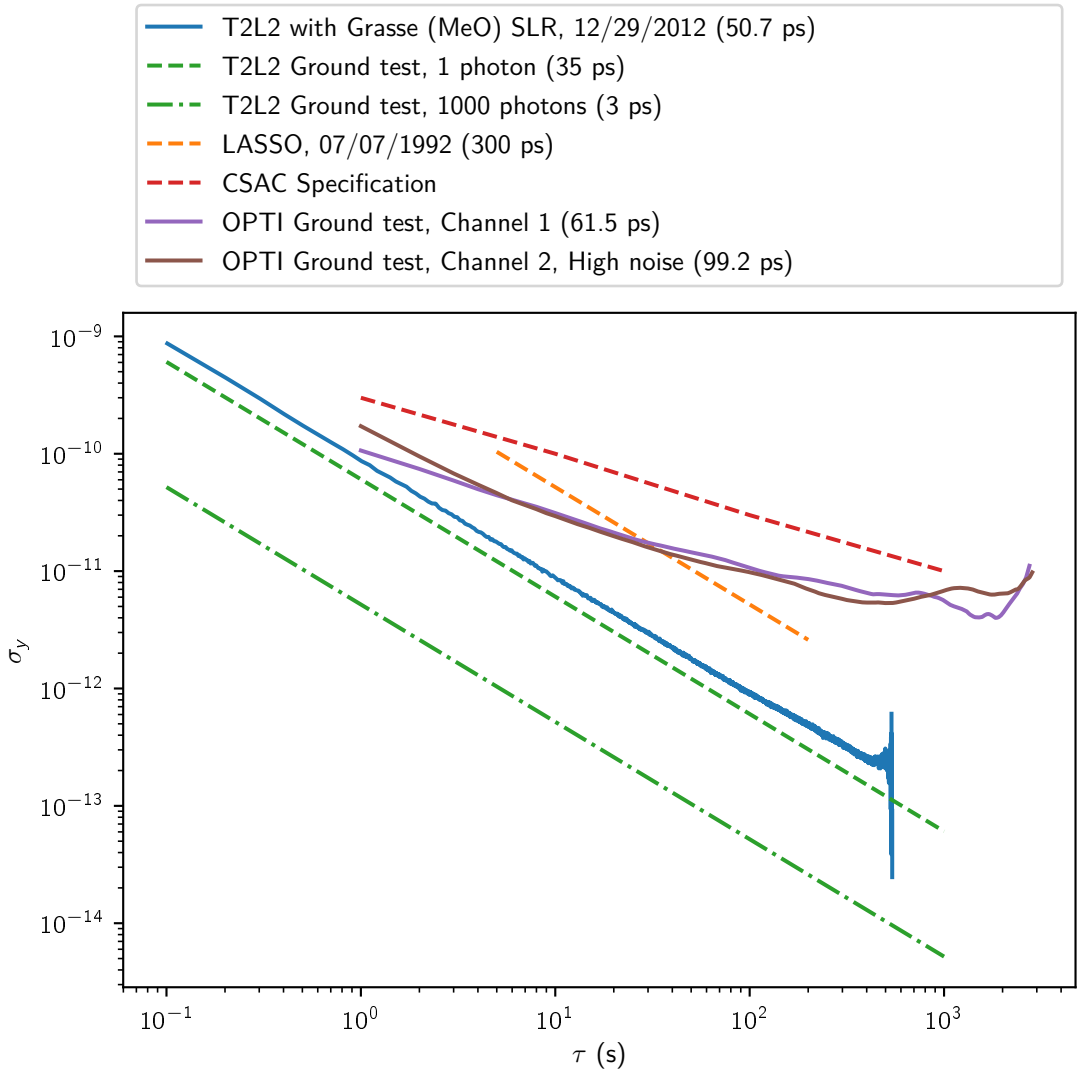

Figure 2-20. OPTI performances compared to past experiments

one included in OPTI, which cannot be more accurate than 10 ps. T2L2's detection scheme is more advanced, more sensitive, and can record pulse energy. It can adjust to pulse energy, something that OPTI cannot do autonomously. However, OPTI was built at a vastly lower cost, is smaller, and consume an order of magnitude less power. In timer transfer mode, an OPTI channel consumes 4.5 W, when T2L2 uses 42 W (28). OPTI can reach a repetition rate

of 10 Hz, and in similar atmospheric conditions, it has the potential to equal the time-transfer abilities of T2L2.

2.5.2.6 Integration with the CHOMPTT CubeSat

To complete the CHOMPTT mission, OPTI has been integrated into a 3U CubeSat, a small satellite of 10 cm $\times$ 10 cm $\times$ 34 cm. The nadir face of the satellite is shown in Figure 2-21, this face bears all the optical components of OPTI. The picture shows six, 1-cm retro-reflectors in the middle for the return pulses, and four laser diodes on a copper mount in the lower part, used as beacons to find the satellite from the ground. The two apertures on the right and left side of the image are bandpass optical filters, centered around 1064 nm. They cover the APDs of two OPTI channels. The launch of CHOMPTT is expected in May 2018.

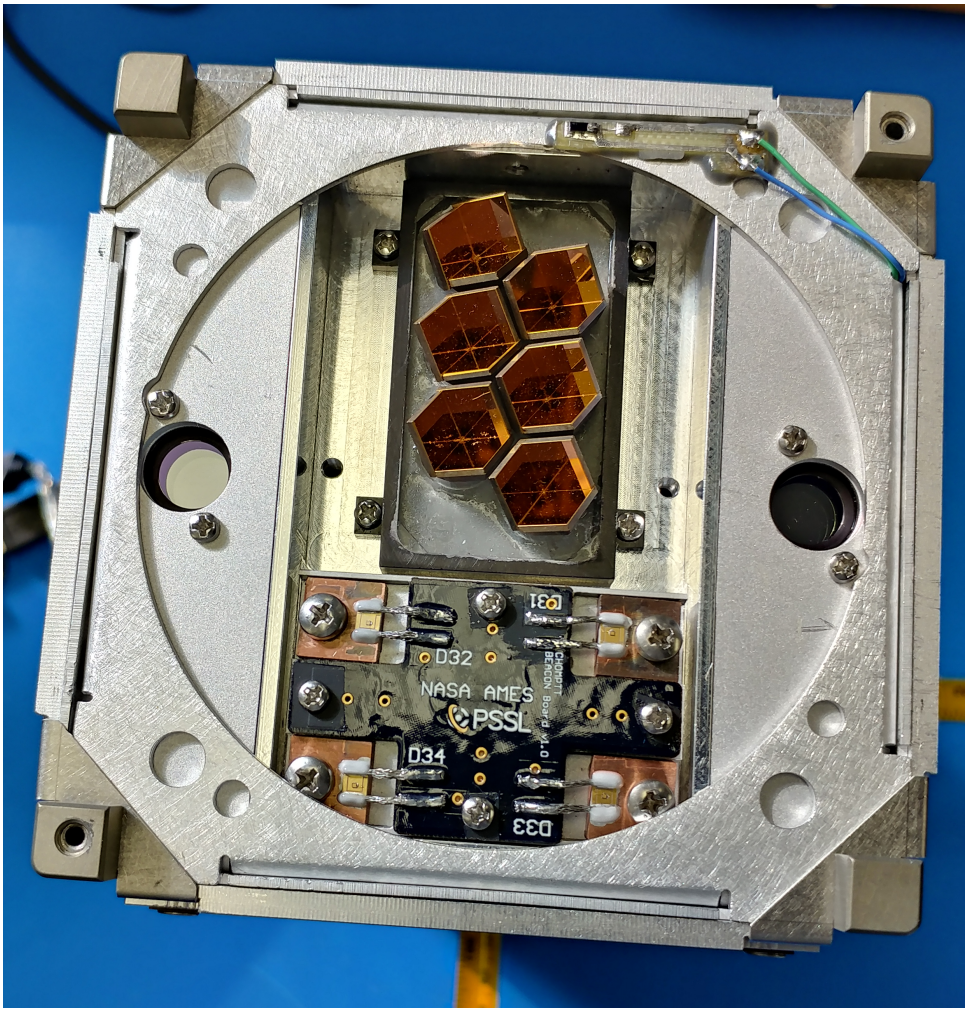

Figure 2-21. OPTI integrated in the CHOMPTT CubeSat. Photo courtesy of Tyler Ritz.

CHAPTER 3
LOW POWER PULSED OPTICAL COMMUNICATION

3.1 Related Works

3.1.1 Optical Communications Modulation Medthods

Various methods have been demonstrated for modulation and demodulation of optical communication signals. Coherent methods like BPSK and DPSK offer superior receiver sensitivity at high data rates while direct-detection methods such as on/off keying and pulse position-position modulation are less complex and allow higher peak-powers, and therefor longer link distances. Pulse Position Modulation (PPM) and Differential Pulse position Modulation (PPM) are the schemes used in this work and have already been described in detail in section 1.5.

On/Off Keying (OOK). In OOK modulation, data is encoded by two optical power levels. On/Off Keying is a common standard for fiber optic communications.

Sub-Carrier Intensity Modulation (SC-IM). The Sub-Carrier method modulates the light power level with a modulated signal at a much lower frequency than the light itself. The data is modulated on a carrier frequency in the KHz to GHz range. The modulated signal is then applied to the light intensity level. This method allows the use of RF components to modulate and demodulate.

Homodyne Binary Phase Shift-Keying (H-BPSK). The H-BPSK method encodes bits with the phase of the emitted light. This is usually done with an electro-optic modulator, separated from the laser source. Binary systems only use two phase positions, 0° and 180°. Higher-order homodyne modulation has been proposed (37), but not demonstrated for space optical communication applications. Homodyne detectors require a reference oscillator. In the case of optical communication, this done with a laser controlled through an optical phase locked loop (38). The received light and the reference oscillator are fed to an 90° optical hybrid. The optical hybrid operates like an interferometer and has a role similar to the mixer on a radio receiver. The demodulated signal is used both to recover data and to steer the

reference oscillator with a Costas control loop (39). The H-BPSK scheme offers higher detection sensitivity at high data rates.

Differential Phase Shift-Keying (DPSK). Like the H-BPSK method, the DPSK method use the light phase to send data. This time, each bit is coded by the difference in phase between two consecutive pulses. The data is recovered by superimposing the received signal with itself, with a time shift of one bit. A Mach Zehnder interferometer is used for that purpose; so a local reference oscillator is not required. However, the bit rate is set by the optics and cannot be adjusted.

3.1.2 Optical Communication Missions

An optical network was proposed as early as 1945 by Arthur C. Clarke in (40). Space-born free-space optical communication has evolved from concepts to experiments in the 1990s, to routine operations in early 2000s, and since 2016 to commercial exploitation. Optical communications has also been demonstrated for interconnection between subsystems inside several spacecraft, including the ISS. Efforts to standardize fiber optic communication for spacecraft has been conducted and resulted in SpaceFiber(41), a technology similar to SpaceWire (42) for electrical signaling. Here we cite a few examples of optical communication transmitters, with a focus on space segments.

3.1.2.1 GOPEX (1992)

In 1992 the Galileo Optical Experiment, using the Galileo probe, demonstrated an uplink at a record distance of 6 million km (66). Pulses were sent with frequency-doubled Nd:YAG lasers from the Starfire Optical Range at Kirtland Air Force Base and the Table Mountain Facility to the Galileo probe while it was conduction an earth fly-by. The pulses were recorded by Solid-State Imaging system and images send back to earth with the probe's radio downlink for verification. One of the images is shown in Figure 3-1. The larger spots, on the right, are from the Starfire optical range. The spots on the left are from the Table Mountain Facility. The record set by GOPEX has been broken in 2006 using MESSENGER's Mercury Laser

Table 3-1. Laser communication transmitters on past or ongoing missions

Year	1994	1998	2000	2001
Experiment	LCE(43)(44)	SILEX(45)(46)	STRV-2(47)(48)	SILEX(46)
Vehicle	ETS-VI	SPOT4	TSX-5	ARTEMIS
Tx mod	OOK	OOK	OOK	2-PPM
Tx rate	1 Mbps	50 Mbps	1000 Mbps	2 Mbps
Tx laser	AlGaAs LD	AlGaAs LD	AlGaAs LD	AlGaAs LD
Tx wavelength	830 nm	847 nm	810 nm	819 nm
Tx power	13.8 mW	40 mW	36 mW	5 mW
Tx aperture	75 mm	250 mm		125 mm
Rx mod.	OOK	none	OOK	OOK
Rx rate	1 Mbps	none	1000 Mbps	50 Mbps
Rx detection	Direct, Si APD	Direct, Si APD	Direct, Si APD	Direct, Si APD
Rx aperture	75 mm	250 mm	137 mm	250 mm
Link distance	45000 km	45000 km	45000 km	45000 km
W and P	80 W 22 kg	150 W 150 kg	100 W 50 kg	150 W 160 kg

Table 3-1. Continued

Year	2005	2007	2012	2013
Experiment	LUCE(49)(50)	TSX-LCT(46)(51)	FITSAT-1(52)	LLCD(53)(54)
Vehicle	OICETS	TerraSAR-X[a]	FITSAT-1	LADEE
Tx mod	OOK	H-BPSK	5KHz subcarrier	16-PPM
Tx rate	50 Mbps	5500 Mbps	10 bps	622 Mbps
Tx laser	AlGaAs LD	MOPFA[b]	LEDs	MOPFA[c]
Tx wavelength	847 nm	1064 nm	526/625 nm	1550 nm
Tx power	100 mW	700 mW	4000 mW	500 mW
Tx aperture	260 mm	125 mm	no optics	100 mm
Rx mod	2-PPM	H-BPSK	none	4-PPM
Rx rate	2 Mbps	5500 Mbps	none	20 Mbps
Rx detection	Direct, Si APD	Homodyne	none	Direct
Rx aperture	260 mm	125 mm	none	100 mm
Link distance	45000 km	5000 km	LEO	400000 km
W and P	220 W 140 kg	125 W 35 kg	20 W $<$1 kg	137 W 32 kg

[a] Identical terminal on NFIRE.

[b] Nd:YAG laser, phase modulator, and ytterbium-doped fiber amplifiers

[c] 1550 nm laser diode, two stages erbium-doped fiber amplifier.

Altimeter. Pulses were sent from MESSENGER and from Earth and recorded on both ends to provided clock synchronization and ranging at a range of 24 million km (26).

Table 3-1. Continued

Year	2013	2014	2014	2015
Experiment	EDRS(55)(50)	OPALS(56)(57)	SOTA(58)	OCSD(59)(60)
Vehicle	Alphasat[a]	ISS	SOCRATES	AeroCube 7
Tx mod	H-BPSK	OOK to 16-PPM	OOK	OOK or 4-PPM
Tx rate	1800 Mbps	50 Mbps	10 Mbps	up to 50 Mbps
Tx laser	MOPFA[b]	MOPFA[c]	Multiple	MOPFA[d]
Tx wavelength	1064 nm	1550 nm	976/1549 nm	1060 nm
Tx power	2200 mW	2500 mW	217/35 mW	10 W
Tx aperture	135 mm	22 mm	50 mm	Fiber
Rx mod	H-BPSK	none		
Rx rate	1800 Mbps	none	1 kbps	10 kbps
Rx detection	Homodyne	none	InGaAs APD	InGaAs PIN
Rx aperture	135 mm	none	50 mm	18 mm
Link distance	45000 km	LEO	1000 km	1000 km
W and P	160 W 56 kg	100 W 50 kg	40 W 6 kg	50W $<$1 kg

[a] Precursor terminal on Alphasat. Similar terminals launched on Sentinel-1A (2014), Sentinel-2A (2015), Eutelsat 9B (EDRS-A, 2016), Sentinel-1A (2016), Sentinel-2B (2017) (61). Identical terminal on upcoming HYLAS-3 (EDRS-C, 2018).

[b] Nd:YAG laser, phase modulator, and ytterbium-doped fiber amplifiers

[c] 1550 nm laser diode, erbium-doped fiber amplifiers

[d] 1060 nm laser diode, two stages ytterbium-doped fiber amplifiers

3.1.2.2 LCE (1994)

The Laser Communication Experiment (LCE) is a payload on the Japanese Engineering Test Satellite-VT (ETS-VI). Its objective was to establish communications between a geostationary satellite (ETS-VI) and either a low-earth orbit satellite or a ground station (67). For this purpose, LCE used an AlGaAs laser diode at 830 nm with an average power of 13.8mW for emission and a Si avalanche photodiode for the receive channel. Both the transmit and receive channels shared a 7.5 cm telescope and aimed at a data rate of 1024 Mb.s^{-1}. Tracking was achieved with a CCD camera and a 4-quadrant Si photodiode and pointing was done by a gimbal mirror with a piezo-actuator point-ahead angle correction. The weight of the payload was 22 kg. Due to a failure of its apogee engine, ETS-VI remained in a highly elliptical orbit. Despite those difficulties, LCE was able to establish an optical link. However, the errors

Table 3-2. Laser communication transmitters on upcoming missions

Year	2018		2019	2023
Experiment	VSOTA(62) (44)		LRCD(63)	DSOC(64)(65)
Vehicle	RISESAT		LRCD	Psyche
Tx mod		DPSK	16-PPM	PPM
Tx rate	up to 100kbps	2880 Mbps	622 Mbps	264 Mbps
Tx laser	Laser diodes	MOPFA[a]	MOPFA[b]	
Tx wavelength	980/1550 nm	1550 nm	1550 nm	1550 nm
Tx power	540/80 mW	500 mW	500 mW	4 W
Tx aperture		108 mm	108 mm	220 mm
Rx mod.	none	DPSK	4-PPM	
Rx rate	none	2880 Mbps	20 Mbps	2 kbps
Rx detection	none	Self-homodyne	Direct	
Rx aperture	none	108 mm	108 mm	220 mm
Link distance	2000 km	GEO	GEO	up to 2.5 AU
W and P	10 W 1 kg	Dedicated bus	Dedicated bus	

[a] 1550 nm laser diode, two stages erbium-doped fiber amplifier.

[b] Separated from the DPSK channel, similar architecture.

Table 3-3. Specifications for MOCT

Year	20xx
Experiment	MOCT
Vehicle	CLICK
Tx mod	4-PPM to 32-PPM
Tx rate	20 Mbps to 100 Mbps
Tx laser	MOPFA[a]
Tx wavelength	1550 nm
Rx mod.	4-PPM to 32-PPM
Rx rate	20 Mbps to 100 Mbps
Rx detection	Direct, InGaAs APD
Link distance	up to 1000 km
W and P	10 W 2kg

[a] 1550 nm laser diode, two stages erbium-doped fiber amplifier.

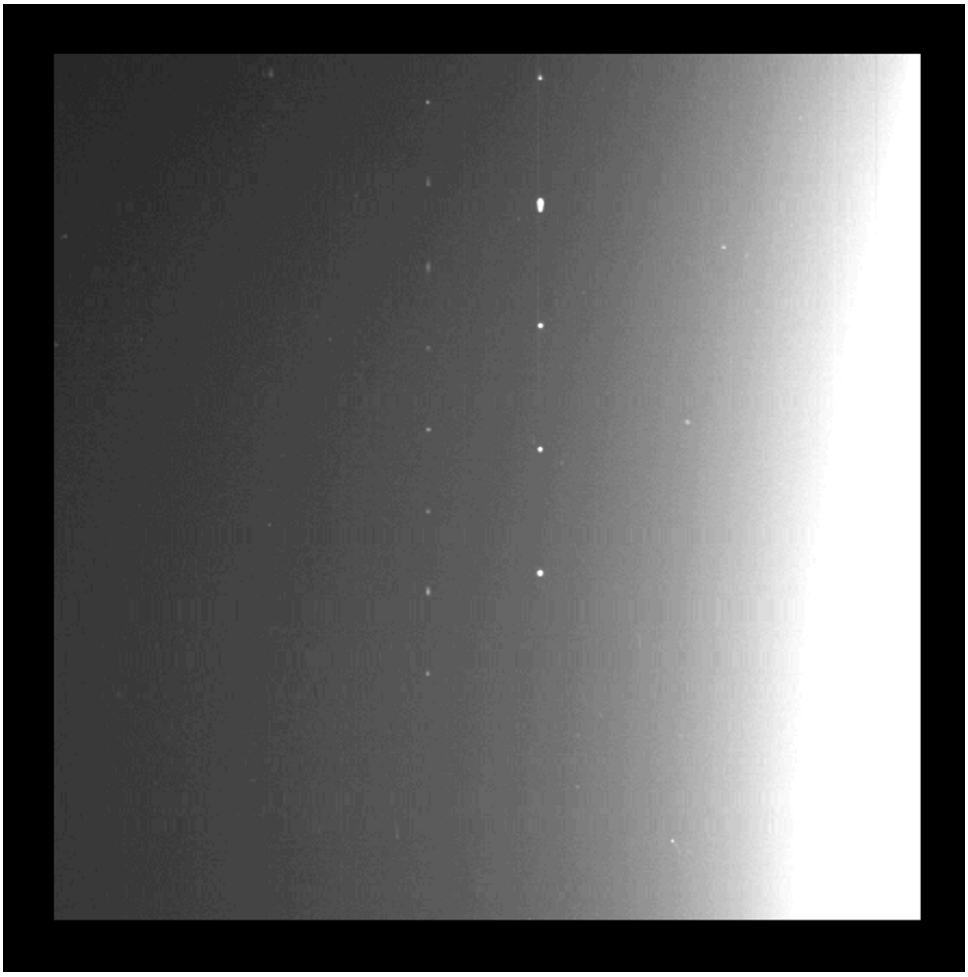

Figure 3-1. Capture from the Galileo Solid-Sate Imaging system for the GOPEX Experiment, published in (66). Picture from NASA.

in LCE tracking were large compared to the downlink beam waist and the optical signal was intermittent. LCE was able to complete most of its objectives and gathered valuable data on atmospheric effects for ground-to-space links (68).

3.1.2.3 SILEX (2001)

The Semi-Conductor Inter Satellite Link EXperiment (SILEX) was an LEO-to-GEO satellite link experiment centered on two terminals. Optical Payload for Intersatellite Link Experiment (OPALE) was a terminal on the Advanced Relay and TEchnology MISsion (ARTEMIS). OPALE weighted 150 kg, and consumed 130 W. PASTEL (Passager Spot de Télécommunication Laser) was a similar terminal on SPOT4 (Satellite Pour l'Observation de la

Terre 4). PASTEL weighed 157 kg, with a power consumption of 150 W. The complete optical assembly was mounted on a gimbal. Both OPALE and PASTEL were equiped with AlGaAs laser diodes at 830 nm, capable of transmitting up to 60 mW average power, with 25 cm telescopes (69). Both used Si avalanche photodiode for detection. Tracking was achieved with a CCD camera, and was established through a wide angle beacon of 750 mrad from OPALE to PASTEL (70) followed by the narrower communication beam of 6 μrad from PASTEL. PASTEL and OPALE established an unidirectional data link, from SPOT4 to ARTEMIS, on November 20th 2001 (71). The link reached data throughputs up 50 Mbps, and was routinely used to download images from SPOT4 to a ground station through ARTEMIS (72). 2018 daily sessions were attempted, out of which 156 failed, until SPOT4 retired in 2013 (71). Various other experiments using the terminal on ARTEMIS were conducted. A link

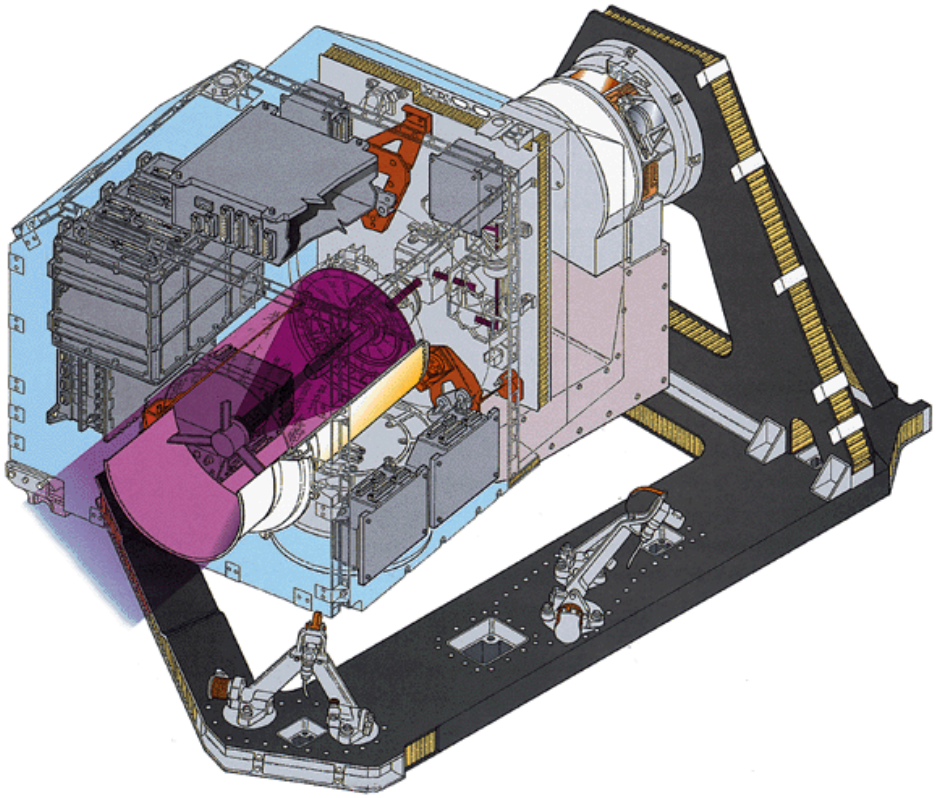

Figure 3-2. SILEX Laser Terminal. Reprinted from ESA Bulletin 91 (73).

from GEO to a plane at high altitude was demonstrated in 2007 with LOLA (Liaison Optique

Laser Aéroportée), on a Falcon 20. LOLA used a 73 mm aperture and used similar laser and detection systems, based on AlGaAs laser diodes ans Si avalanche photodetectors. A link between ARTEMIS and on optical ground station was also established on November 15th 2001 (71). Another LEO-to-GEO link was tested through the LUCE mission, described in the next section.

3.1.2.4 LUCE (2005)

LUCE (Laser Utilizing Communications Equipment) was an optical communication payload on-board the Optical Inter-orbit Communication Engineering Test Satellite (OICETS). LUCE was designed to operate with OPALE, and established a link on december 9th 2005. Unlike PASTEL on SPOT4, LUCE was also capable of receiving data. LUCE also demonstrated a link to a ground station (50).

3.1.2.5 TSX-LCT (2007)

TSX-LCT validated technologies for a cross-link between two satellites. Two identical terminals built by TESAT Spacecom Gmbh were hosted on TerraSAR-X, from the DLR, and NFIRE from the Missile Defense Agency. The terminals used Homodyne BPSK modulation, and reached an unprecedented uncoded data throughput of 5.6 Gbps (51). The transmitter used a Nd:YAG laser, followed by a phase modulator and an ytterbium fiber amplifier, and the receiver used an optical phase-locked loop. Pointing was achieved with the data beam, without a beacon. The terminal on TerrasSAR-X also established links with an optical ground station.

3.1.2.6 FITSAT-1 (2012)

FITSAT-1 from the Fukuoka Institute of Technology was a 1U (10 cm by 10 cm by 10 cm) CubeSat deployed from the ISS in 2012. FITSAT-1 was fited red and green LEDs with an electrical peak power of 230 W and 160 W respectively (52). The LEDs were modulated with a 5 kHz sub-carrier, with a duty-cycle of 15%, and were capable of sending messages in Morse code.

3.1.2.7 LLCD (2013-2014)

The NASA Lunar Laser Communication Demonstration was a payload on the Lunar Atmosphere and Dust Environment Explorer. It set the state-of-the-art for optical communication beyond the Geostationary orbit with a data rate of $20\ \mathrm{Mb.s^{-1}}$ for uplink, and $622\ \mathrm{Mb.s^{-1}}$ for downlink from the moon (54). LLCD used a transmitter based on PPM modulation with a 0.5 W erbium-doped fiber amplifier, at 1550 nm. The link was reliable, and the wight and power within 31 Kg and 90 W respectively. Figure 3-3A shows the fiber components of the LLC modem, and 3-3B shows the 10 cm optical aperture, on gimbals with inertial stabilization.

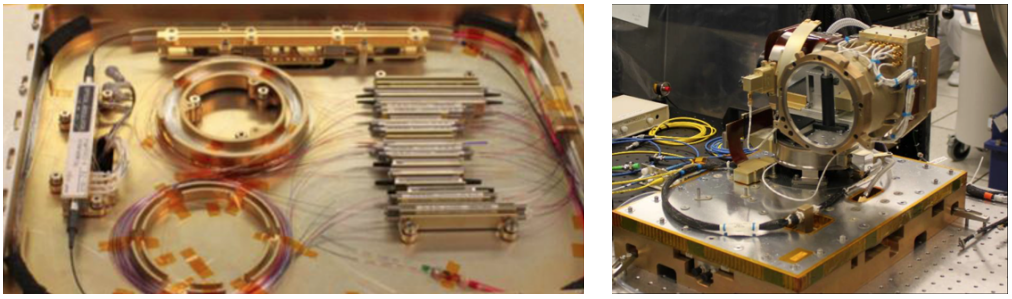

A B

Figure 3-3. A) LLCD Modem Fibers, B) LLCD Optical Module

3.1.2.8 OPALS (2014)

Optical Payload for Lasercom Science (OPALS) was a module installed on the International Space Station in 2014, and it was used as a test-bed for high-bandwidth downlinks at 1550 nm. OPALS demonstrated data throughputs of 50 Mbps with a 2.5 W laser system.

3.1.2.9 AeroCube7-OCSD-A (2015)

Aerocube 7 aims at demonstrating various capabilities on CubeSats, including precision pointing, proximity operation, and innovative thrusters. The main experiment is a laser transmitter built with a two-stages ytterbium-doped fiber amplifier. The laser system output power is 10 W, at 1060 nm. It is capable of sending up to 50 Mbps with OOK modulation. Three spacecraft have been launched, OCSD-A, B and C. OCSD-A is the engineering unit of OCSD-B and OCSD-C that has been launch in 2015 for risk reduction. Issues with the attitude control system prevented any test of the optical transmitter with OCSD-A. OCSD-B and

OCSD-C, featuring similar laser systems, have been launched in November 2017. The results of this mission are still pending.

3.1.2.10 EDRS (2005,2016)

The European Data Relay Satellite system is a network of hosted payloads that have an objective similar to that of the Tracking and Data Relay Satellite System started by NASA in 1983. The payloads include an Laser Communication Terminal (LCT) and Ka band radio link. The LCT communicates with satellites in low earth orbit, and transmissions are relayed to a ground station with the Ka band radio. The LCTs are similar to the terminals on TerraSAR-X and NFIRE but have been tuned for longer range, with a reduced data throughput of 1800 Mbps, uncoded. The Ka band radio is limited to 600 Mbps. A precursor terminal called TDP1 was carried by Aplhasat in 2013, a commercial communication satellite. An operational terminal was hosted on Eutelsat 9B and launched in 2016. A second operational terminal will follow in 2018, hosted on HYLAS-3. Two other terminals are planned, giving the network complete coverage of the Earth (61). As of early 2018, the clients of the EDRS network are 4 satellites of ESA's Copernicus program: Sentinel-1A&B, a pair of synthetic aperture radar imagers, and Sentinel-2A&B, a pair of multi-spectral imagers. EDRS is now open to third parties.

3.2 System Architecture and Implementation*

In order to demonstrate optical communication on a low power platform, the Precision Space Systems Laboratory (PSSL) at the University of Florida is developing a pulsed laser transmitter. The Miniature Optical Communications Transmitter (MOCT) is a compact pulsed laser transmitter with a target mass and power consumption level of 2 kg and $<$10 W while transmitting. PPM have been selected as communication scheme to maintain a low average power while maintaining a detectable peak-power.

* The results in this section have already been published in (1)

MOCT is designed to be integrated with a CubeSat of at least 3U or on larger deep space spacecraft that are power-constrained. The selected wavelength and pulse energy levels make it compatible with existing ground terminals, for example those used for the LADEE mission, or upcoming one for DSOC.

MOCT includes a novel, highly flexible modulator based on timestamps. The modulator contains a innovative calibration circuit with a record accuracy, better than 2 ps. This modulator make MOCT a capable communication systems, with maximum data rates in the tens of Mbps, but also navigation instrument with the ability to perform one-way or two way ranging and time transfer. The seed laser driver circuit built during this project offers a very high extinction ratio and have the ability to generate very narrow pulses of 100 ps. Those characteristics make it ideal for long range, deep space optical communication, at slower data rates. Although MOCT cannot reach the data rate of state-of-the-art payloads like LLCD on LADEE, and even considering the fact that MOCT does not address pointing issues, the size and the power consumption of the modulator remain very competitive.

3.2.1 MOFPA / SDPM

The MOCT is built upon two main subsystems: the Software Defined Pulse Modulator (SDPM) and the Master Oscillator Power Fiber Amplifier (MOPFA) laser system.

The MOPFA system is a 1550 nm fiber laser with target pulse widths of 100 ps and pulse energies of 1 mJ. The MOPFA uses a 50 mW 1550 nm seed laser diode. The light pulses emitted by this laser are fed into an erbium-doped fiber amplifier, with one or more stages, pumped by 500 mW 980 nm laser diodes.

The SDPM generates electrical pulses to encode the data according to a PPM scheme. The pulses are sent to the seed laser. The modulator is entirely implemented in a Field Programmable Gate Array (FPGA) to keep power, volume and complexity under control and allow flexible prototyping. The delays in the modulator are calibrated using a Delay Locked Loop (DLL). A CSAC is used as reference for the DLL and for internal counting. The SDPM is the main subject of this chapter and will be described in the following sections.

3.2.2 FPGA-Based Software Defined Pulse Modulator

Several treatments are required to generate electrical pulses from the raw input data. Those steps are described in Figure 3-4. First, a forward error-correction code is applied to the data. Next, the M-PPM scheme is applied, at the digital level, transforming the data in a string of timestamps. In order to be converted in timed electrical pulses, the timestamps are then separated in two part. The first part is a counter value, this value is compared to a running counter. When it match, a base pulse is emitted. That base pulse then travel through a variable delay chain. The second part of the timestamp is applied to the delay chain, to shifts the base pulse in time. Thanks to the delay chain, the pulse can be placed with a resolution higher than the period of one counter bit, and higher than what is allowed by the maximum system frequency. The delay chain is specific to the device used for the modulator implementation and its layout must be done carefully. The modulator is implemented in a Microsemi SmartFusion 2. As of this writing, error correction codes have

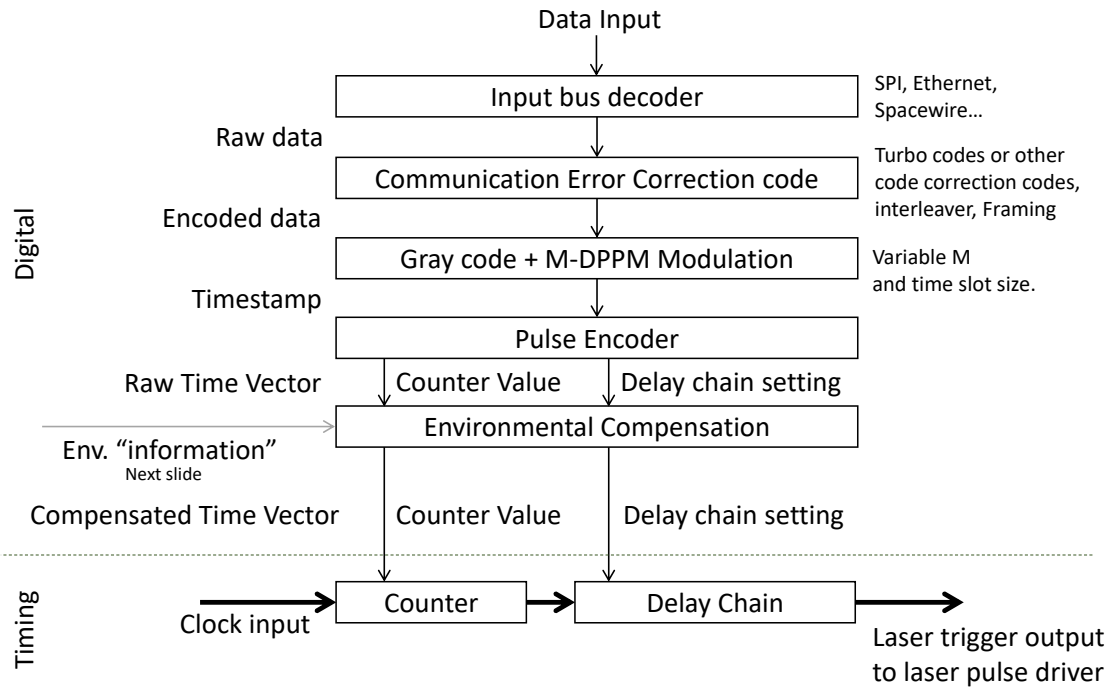

Figure 3-4. Modulator Data Flow

not been implemented in the modulator.

3.2.2.1 Counter

The modulator counter is 32 bit long and clocked at 200 MHz. The 200 MHz frequency is generated by one of the FPGA PLL from the CSAC 10 MHz signal. One periode of the counter is 5 ns, so the delay chains must be a able to adjust the pulse delay by at least the same value.

3.2.2.2 Delay chain

In our current implementation, the delay chain has two independent settings of 256 positions. The delay chain design is built around two device specific structures: The clock distribution network and the carry chain. Both run in parallel of the FPGA logic cells, in the same direction. Both are faster than the normal routing matrix. The row clock distribution lanes are slightly faster than the carry chain network, so a delay variation can be achieved by selecting in witch cell the signal cross from the clock distribution lane to the carry chain1. The delay variation is plotted in figure 1. The delay chain have an overall delay of 12 ns for a variation of 6 ns. The output jitter is 3.5 ps, at the same level as the floor FPGA fabric jitter. The size of a 1-bit increment is 12 ps in average, however non-lineraties of more than 90 ps are present, and the delay increase are monotonous.

Since two delay chains are used to obtain a delay range of 6 ns that can cover a complete counter period, it is possible to use advantageous combinations of settings to get closer to desired delay value. As shown in Figure 3-5, the objective is to find a pair of settings that together give a target delay variation. This search is done for a large range of evenly spaced target delays to get a better scale of delays. This is required since the residuals of the raw scale are large, with an integral nonlinearity of more than 90 ps, as shown in Figure 3-6. Chain designs with lower nonlinearity have large static (non-adjustable) delays that result in very low repetition rate and poor jitter performance. In therory, based on the internal measurements made using the delay locked-loop circuit, it is possible to reach extremely low deterministic jitter. Figure 3-7 shows the deterministic error of combinations of delays, assuming perfect measurements of the *raw* delays by the DDL circuit. A random jitter of up to 7 ps is also present. However, if the standard deviation of the DLL circuit

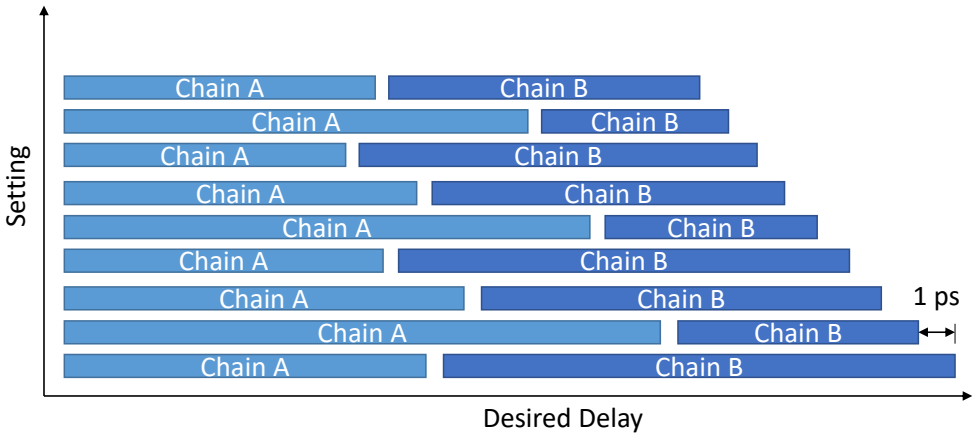

Figure 3-5. Exemples of delay combinaisons

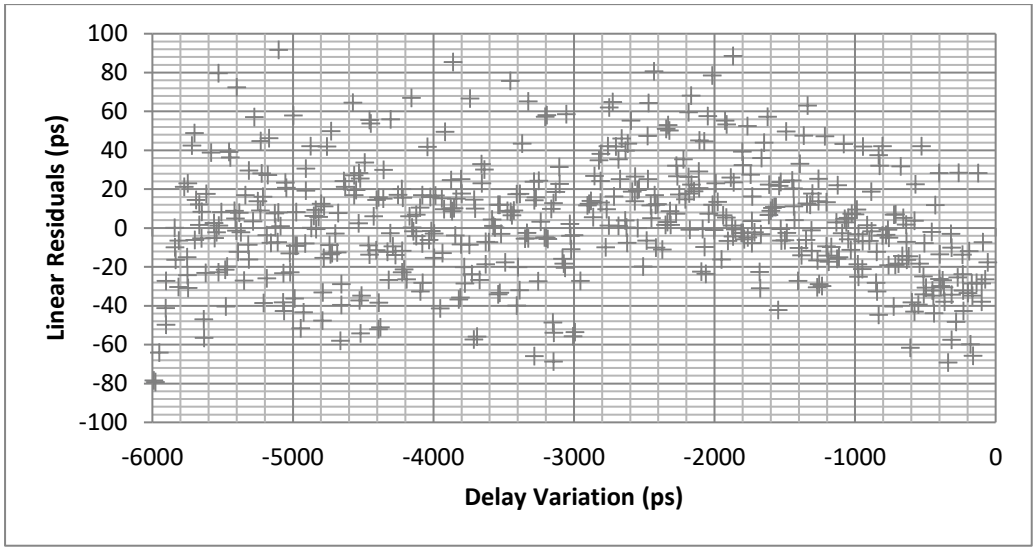

Figure 3-6. Linear residuals of raw delays

measurements is below the picosecond-level, the bias of those measurements is usually larger than a picosecond. Figure 3-8 shows the deterministic error of combinations of delays, assuming perfect measurements of the *pairs* of delays by the DDL circuit. The comparison of expected and measured results for pairs of delays provides an estimate of the bias of the Delay Locked Loop circuit. Here, this bias is always less than 6 ps, with a standard deviation below 2 ps. Even if the delay scale is not as good as depicted by Figure 3-7, the improvement over raw delays is still substantial. The raw delay and pair of delays scales are compared in Table 3-4. The DLL circuit can work at frequencies multiple of a base locking frequency,

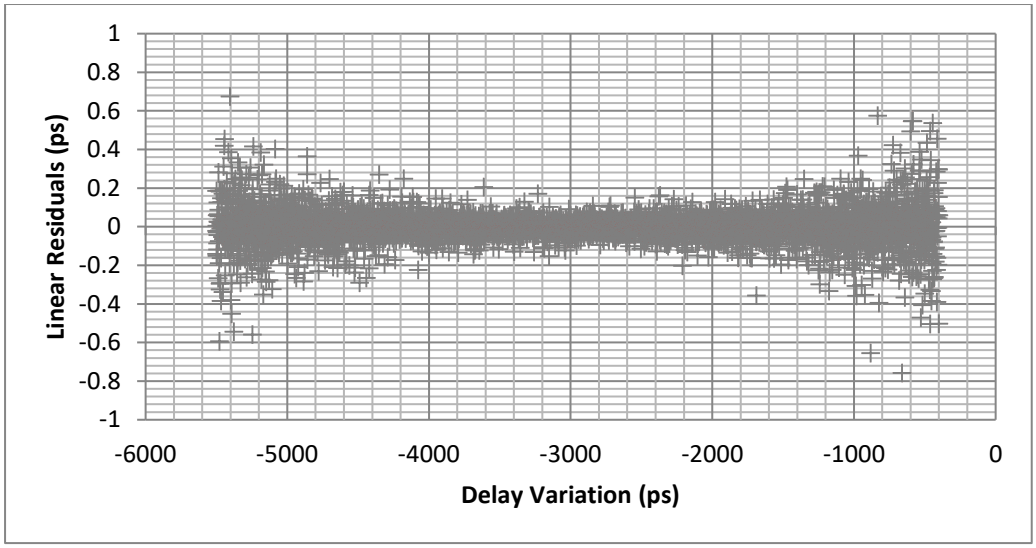

Figure 3-7. Linear residuals of theoritical combinaisons of delays

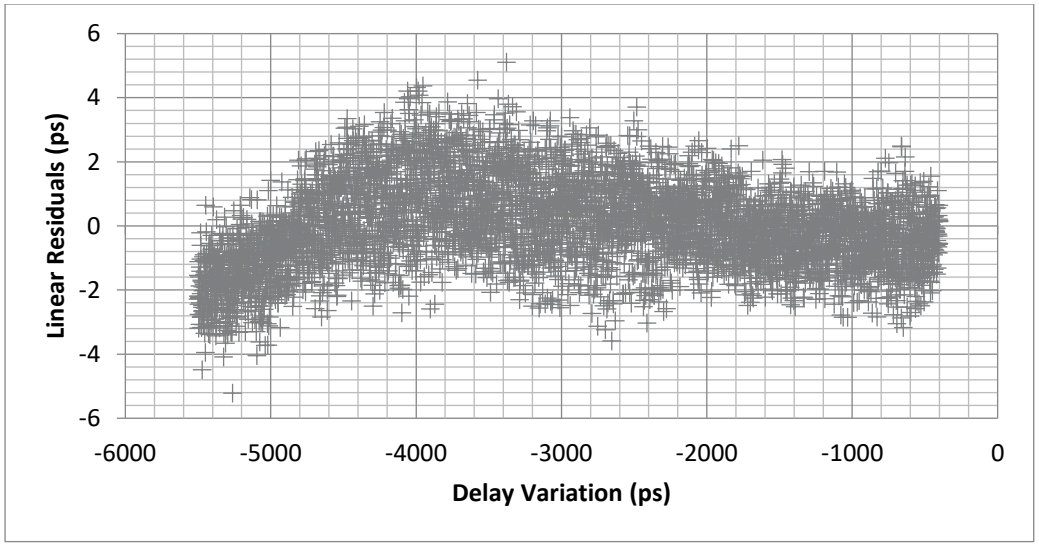

Figure 3-8. Linear residuals of measured combinaisons of delays

Table 3-4. Delay scale improvement

Value	Raw Delays	Combinations of Delays
LSB average value	11.56 ps	1 ps (adjustable)
Number of entries	512	5100
Largest gap	$>$ 70 ps	6.70 ps
Integral Non Linearity	96.7 ps	5.52ps
Standard deviation of error	39.2 ps	1.35 ps

which can be assimilated to harmonics [1]. Sampling several modes allow to estimate the bias of the measure at deferent frequency. A fixed known ballast delay could also be inserted to estimate the measurement bias with a different base and harmonics frequency.

3.2.3 Calibration and Environmental Effect Compensation*

Calibration and compensation of environmental effects is done by measuring the delays directly, thanks to a Delay-Locked Loop (DLL). The proposed DLL circuit is made of 4 parts:

1. Variable frequency generator: Generates a new clock signal at the desired frequency, referenced to an external oscillator.
2. Phase Detector: Compares a delayed signal to the original signal and finds the phase difference.
3. A delay being measured
4. Control System: Adjusts the variable frequency generator to keep the loop locked and computes the outputs, including the estimate of the delay time

The circuit operates as shown in Figure 3-9: The signal from an external clock is used as the reference input to the variable frequency generator consisting of a pair of PLLs. The output of the variable frequency generator contains the selected delay period denoted T_{var}. This signal is split into two paths: One is sent directly to the phase detector, while the other is first passed through the delay under test and then to the phase detector. The phase detector itself consists of a D-Type latch, denoted D in Figure 1, and two counters. The phase detector measures the time difference between the delayed Tvar signal and the original Tvar signal over a small window. This is done by counting the total number of Tvar pulses with the Counter A, and the number of delayed clock Tvar that arrive before a rising edge of the un-delayed clock signal with the Counter B. The control system adjusts the variable period so that the ratio of the value in Counter A divided by the value in Counter B stays as close as possible to 0.5. If the ratio is kept around 0.5, The delay under test is equal to T_{var}. The circuit has been

* The results in this section are part of a forthcoming paper in the IEEE Transactions on Instrumentation and Measurement.

implemented on a Microsemi Frequency & Time Corporation SmartFusion2 FPGA (15), using a Microsemi SA.45s Chip Scale Atomic Clock (CSAC) (12) as the external frequency reference. The CSAC provides a standard 10 MHz reference signal to the FPGA with an Allan deviation of 3×10^{10} at 1 s.

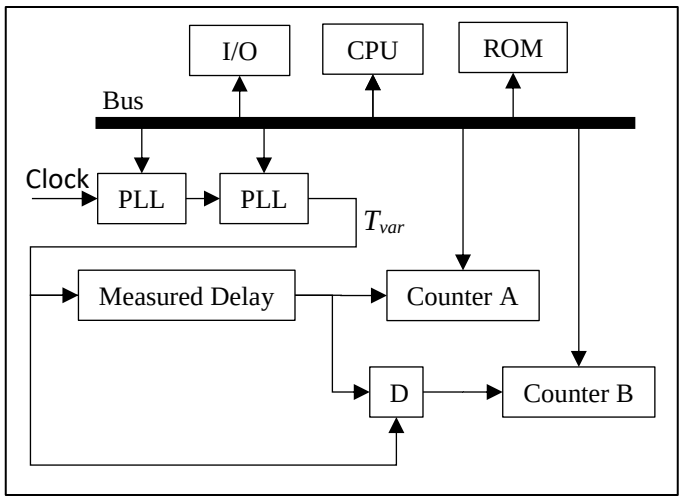

Figure 3-9. Block diagram of the Delay Measurement Circuit

3.2.3.1 Variable frequency generator using PPLs

The variable frequency generator uses two phase-locked loops successively to generate a new desired frequency from the 10 MHz reference signal. The PLLs can generate an integer fraction of the input frequency, with some restrictions. More combinations and a finer frequency ratio can be generated using two sequential PPLs. The frequency of the reference oscillator, denoted f_{clk}, is converted to an intermediate frequency, f_{mid}, with a phase-locked loop using two reference dividers R_1 and R_1', a pair of feedback dividers, F_1 and F_1', and finally an output divider O_1'. The intermediate frequency is then converted to the variable frequency generator output, f_{var}, using the second phase-locked loop with the respective dividers, F_2, F_2', R_2, R_2' and O_2'. Another pair of dividers (noted O_1 and O_2) are also present to reduce the PLLs voltage controlled oscillator's output, but they do not influence the output frequency of the PLL.

$$f_{mid} = \frac{F_1 F_1'}{R_1 R_1' O_1'} f_{clk} \qquad f_{var} = \frac{F_2 F_2'}{R_2 R_2' O_2'} f_{mid} \tag{3–1}$$

The values of dividers have limits set by the PLLs design (74):

$$\begin{aligned} R_1, R_2 &\in [\![1, 2^8]\!] \\ F_1, F_2 &\in [\![1, 2^{14}]\!] \\ R_1', R_2' &\in [\![1, 2^8]\!] \\ F_1', F_2' &\in [\![1, 2^7]\!] \\ O_1', O_2' &\in [\![1, 255]\!] \end{aligned} \tag{3–2}$$

Various frequencies are also limited inside the PLL. The input frequency must both above 1 MHz and below 200 MHz after going through the first reference divider, R_1. The output is also limited to frequency ranging from 20 MHz to 400 MHz (15). Furthermore, for our design, we are interest in a limited range of frequencies, associated with periods from 4 ns to 14 ns. This corresponds to frequencies between 71.5 MHz and 250 MHz. With this frequency range and the constrains imposed by the FPGA (74), we arrive at the following frequency bounds:

$$\begin{aligned} 1MHz \leqslant f_{clk} R_1 &\leqslant 200MHz \\ 20MHz \leqslant f_{mid} &\leqslant 400MHz \\ 1MHz \leqslant f_{mid} R_1 &\leqslant 200MHz \\ 71.5MHz \leqslant f_{var} &\leqslant 250MHz \end{aligned} \tag{3–3}$$

To be able to change the output frequency, f_{var}, rapidly, a table of PLLs dividers must be computed and stored in the system. Thanks to the restrictions on dividers and on frequencies, an exhaustive search of the divider values is possible. We searched for the best set of values that produce a scale from 4000 ps to 13999 ps with a step size of 1 ps for the output period. Figure 3-10 shows the deviation of the best combinations from a perfect 1 ps scale. The maximum deviation from the 1 ps scale is 0.12 ps. All the corresponding values for F_1, F_1', R_1, R_1', O_1' and F_2, F_2', R_2, R_2', O_2' can be compressed into a 40 kB table that is stored in the

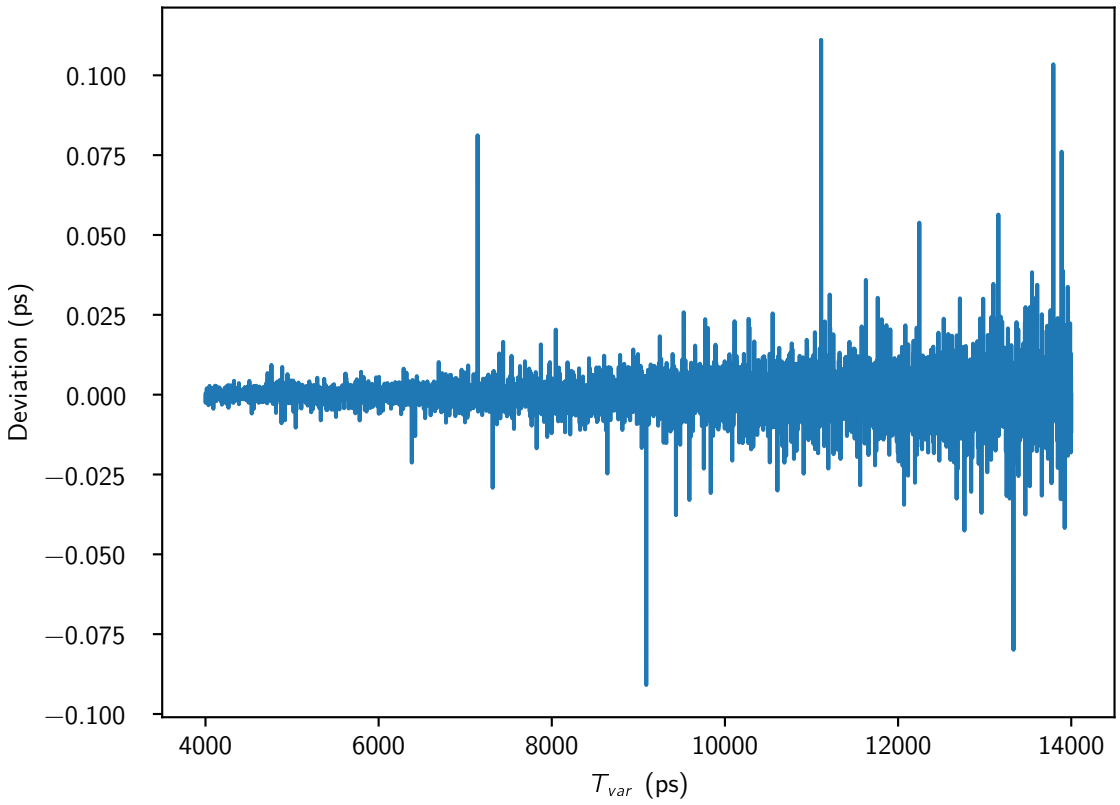

Figure 3-10. Deviation of T_{var} from a perfect 1 ps scale

control system. Because the loops are locked in phase, the average output frequency, f_{var}, is guaranteed to be the selected fraction of f_{clk}. We consider the average output frequency to be error-free. However, cycle-to-cycle jitter (noise in time) is still present, so the instantaneous frequency is not exact. The impact of this cycle-to-cycle jitter on the overall performance of the circuit is bounded by the measured timing errors discussed in subsection 3.3.1.

3.2.3.2 Measured delay

The measured delay is the delay chain of the modulator, described in subsubsection 3.2.2.2. The circuit under can be modeled as a collection of delays that we denote D_n with $n \in [\![0, 65535]\!]$, or $D_{x,y}$ with $x, y \in [\![0, 255]\!]$.

3.2.3.3 Phase detector

The phase detector compares the phase of two signals: the clock signal from the variable frequency generator, and that same clock signal delayed by the delay circuit under test with a delay of D_n. To compare the signals, the phase detector uses a D-Type latch. The latch indicates which signal arrives first, and outputs either a 0 or a 1 correspondingly. By repeating this measurement many times, and adjusting the variable period T_{var}, it is possible to find the transition between 0 (The delayed rising edge arriving after the un-delayed rising edge of the next clock period) and 1 (The delayed rising edge arriving before the next clock period). At that precise transition the phase difference, $\Delta\varphi$, is an integer multiple, k, of the delay being measured, D_n:

$$\Delta\varphi = k \cdot D_n, k \in \mathbb{N} \tag{3–4}$$

An example of one of these transitions is plotted in Figure 3-11. This figure shows the counter fraction Counter B/Counter A as a function of the variable period, T_{var}, near the transition. Note that the transition is not infinitely sharp, but can be modeled as a Gaussian cumulative distribution function (CDF). This is expected, since this behavior is caused by the latch meta-stability (75) and the PLL random jitter (76) which are both Gaussian. The best fit Gaussian CDF to the data is shown as the dashed curve in Figure 3. The best fit CDF has a mean value of 5.274 ns and a standard deviation of 3.14 ps. The mean value, which corresponds to the value of T_{var} for which the counter ratio is 0.5, is also an estimate to the delay time for the circuit under test. For a given delay circuit, D_n, with delay time, T_{del}, and $k = 1$, a sampling period T_{var}, sampled at time t_s, the probability, $P_{D_n}(T_{var}, t_s)$, of getting a one is the following.

$$\begin{aligned} P_{D_n}(T_{var}, t_s) &= \frac{1}{2}(1 + erf(\frac{T_{var} - D_n(t_s)}{\sigma_m\sqrt{2}})) \\ P_{D_n}(T_{var}, t_s) &= \frac{1}{\sqrt{\pi}} \int_{-\infty}^{\frac{T_{var}-D_n}{\sigma_m}} e^{\frac{-t^2}{2}} dt \end{aligned} \tag{3–5}$$

We assume that the delay can be modeled as a Gaussian CFD, which is validated by the measurements shown in Figure 3. The probability, $P_{D_n}(T_{var}, t_s)$, is estimated by sampling

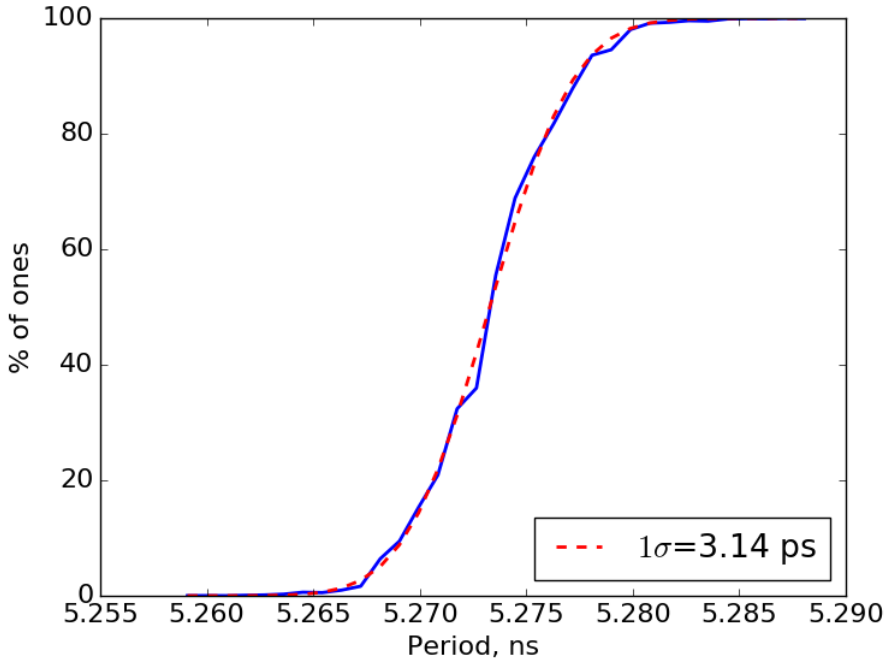

Figure 3-11. Transition in the phase detector circuit

the binary test m times, assuming a range of standard deviations, σ_m, of 2 to 10 ps. For a fixed delay, D_n, at a fixed sampling period, T_{var}, $P_{D_n}(T_{var}, t_s)$ changes depending on both measurement errors and PVT variations. Our objective is to estimate these errors. The standard deviation of the distribution, σ_m, has been verified to be stable both over time and for different settings of the delay chain. With a single measurement point, $P_{D_n}(T_{var}, t_s)$, if not equal to 0 or 1, it is possible to estimate the phase difference by inverting Equation 3–5 and solving for $D_n(t_s)$. With $P_{D_n}(T_{var}, t_s) \in]0, 1[$ and $k = 1$:

$$D_n(t_s) = T_{var} - \sqrt{2}\sigma_m erf^{-1}(2P_{D_n}(T_{var}, t_s) - 1) \tag{3–6}$$

3.2.3.4 Control system

The control system samples the phase detector counters, adjusts the PLL settings of the variable frequency generator, and performs the required calculation, Equation 3–6, to extract D_n. The controller holds the table of PLL settings. Due to its limited resources (64 MB of random access memory, 100 MIPS, 500 kB of non-volatile and program memory), the control

system cannot record and transmit all the raw results of the phase detector circuit, and must count them in a reduced period of time. For this reason, the data extracted from the circuit is not sampled at an exact time, t_s, but rather it is sampled through a series of m binary challenges over a time interval, $m \cdot T_{var}$. To measure delay periods over time, the control system adjusts T_{var} whenever $P_{D_n}(T_{var}, t_s)$ is outside of the interval $[0.15, 0.85]$. The period T_{var} is replaced by $T_{var} + 3\sigma_m[0.5 - P_{D_n}(T_{var}, t_s)]$. As the two PLLs need time to lock onto a new frequency (70 s to 16 ms each, so 140 s to a maximum of 32 ms in total (15)), the number of adjustments of T_{var} is limited to minimize the periods without feedback.

3.2.3.5 Aliases

The circuit will lock if the delay under test is equal to one period of the clock. It will also lock if the delay is an extract multiple k of the clock period. This behavior, similar to harmonics, can be exploited to measure longer delays than would be possible based on the minimum frequency of the variable frequency generator. The range of possible periods needs to be at least $[T, 2T]$ to cover any delay larger than T. If it is not possible to measure a particular delay one can measure the phase difference multiple k by measuring two successive transitions of phase differences $\Delta\varphi_k$ and $\Delta\varphi_{k+1}$:

$$k = \frac{\Delta\varphi_k}{\Delta\varphi_{k+1} - \Delta\varphi_k} \tag{3–7}$$

If it is desired to estimate k for any delay, then the range of possible periods needs to be at least $[T, 3T]$. For converters however, the expected delay values are known with sufficient accuracy not to require the use of Equation 3–7. We designed our delay chains to cover 6 ns, with a constant overhead of 6 ns. The range of periods achievable with our variable frequency generator is $[4, 14]$ and can therefore cover all delays with just $k = 1$.

3.2.4 Seed Laser Driver

The driver designed for the seed laser presented in the following section has several objectives. The main one is to maintain a very high extinction ratio. The extinction ratio r_e is the quotient of the high level optical output power P_1, signaling a set bit, and the low level

power P_0, signaling a cleared bit. $r_e = P_1/P_0$. The driver must be able to generate short pulses of a arbitrary duration, with jitter below 100 ps for both the rising edge and the falling edge. Finally, complexity and power consumption must stay under control, and the circuit must be robust and stay stable under external disturbances such as electromagnetic interference (EMI) and thermal effects.

3.2.4.1 Gain-switching

A secondary objective of the presented circuit is to explore the possibilities of gain-switching (77). All lasers require energy to be pumped into the their cavities. For laser diodes, the pump power is provided as an electrical current. Gain-switching is a laser modulation method that adjusts the laser gain by abruptly providing the pump power, and then removing it. Once the pump power is applied, several oscillations in the laser's resonator are required to produce coherent light. During these oscillations, the upper-state population in the laser cavity gain medium keeps increasing and the laser gain rises beyond its steady-sate value for the given pump power. The laser pulse build-up, and thanks to the increased gain, reaches an amplitude higher than the steady-sate output. Because of the high laser light power, the upper-sate population is rapidly depleted. If the pump power is cut at that moment, a single, shot pulse is extracted from the laser. This pulse can be shorter than the electrical pump pulse. In semiconductor laser diodes, this process results in pulses with durations from a few hundreds of picoseconds down to a few picoseconds (78)(79).

3.2.4.2 Principle of operation

The driver circuit is based on direct on/off modulation. The laser is completely turned off during pulses and stops outputting coherent light. A simplified circuit diagram is shown in Figure 3-12. Current for the laser is generated by a current source noted I1. When the Field Effect Transistors (FET) Q1 and Q2 are opened, this current is directly delivered to the laser diode D1. When Q1 or Q2 is closed, the potential at the anode of D1 is set to ground. This sets the voltage across D1 to an adjustable bias voltage v_B thanks to the voltage source V1. The bias voltage v_B should be picked below the lasing threshold of D1 to obtain a high

extinction ratio. The bias v_B voltage allows a higher voltage across D1 at all times. The variation in voltage at the anode of D1 between the ON and OFF state is reduced. Since the variation is smaller, the required rise time at the anode of D1 due to the capacitance of that node is also reduced, leading to faster commutation. Furthermore, maintaining a higher bias leads to a higher upper-sate population in the laser cavity at all times. The application of pump power generates coherent radiation faster, reducing the delay between the electrical pulse and the seed light pulse. A reduced delay leads to reduced time uncertainties due to that delay. As gain-switching is highly dependent on the turn-on dynamics of the laser, an adjustable bias gives more opportunities to control those dynamics.

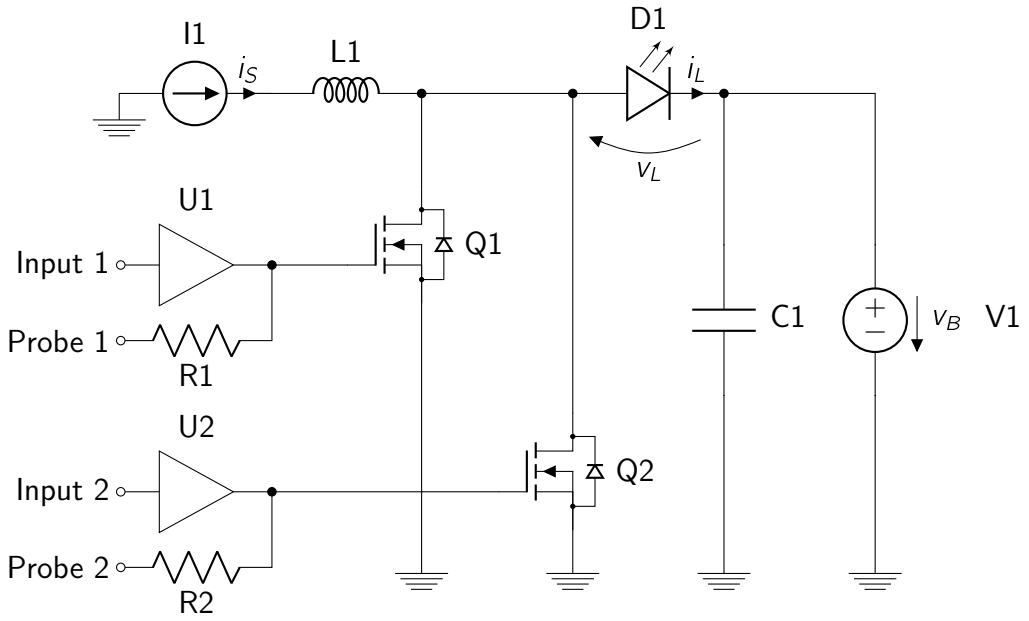

Figure 3-12. Seed laser Pulse driver circuit

The FETs Q1 and Q2 are driven by buffers U1 and U2, connected to the inputs of the circuit. As both Q1 and Q2 are connected to two parallel branches, they can both trun off the laser. The sate of the laser is the result of the boolean equation $\overline{Input1} \cdot \overline{Input2}$. Since this operation is done electrically at the laser anode, the buffers and all the electronics before the driver circuit are not required to generate short pulses, but instead have to provide two signals with a stable phase difference. Only the FETs and the laser diode must have a bandwidth

compatible with a few nanosecond or sub-nanosecond pulses. The pulse duration is set by time from an input falling edge to the other input rising edge. The resistors R1 and R2 provide a feed back from the FET gates. Their values are selected to provide measurable readings of the gates voltages while maintaining some isolation: the capacitance at the gate nodes must be maintained as small as possible to get fast commutation times and sharp rising edges at the drain for short pulses. As the shunt impedance of the current source I1 cannot be arbitrarily high, an inductor L1 is added to improve the stability of i_S at high frequencies. Similarly, a capacitor C1 is required to compensate for the series impedance of V1.

3.3 Measured Performance

3.3.1 Delay Chain Static Errors and Calibration*

We performed three tests to assess the performance of the delay measurement circuit. The goal of the first was to measure the impact of PVT effects on the on a single delay chain within the FPGA. The second demonstrates the circuit's ability to measure a large range of delay values. The final measurement uses combinations of delays to determine if there are any biases in this measurement method.

3.3.1.1 PVT variations

Time domain. The circuit was used to repeatedly measure a single fixed delay chain over time to estimate the circuit's ability to measure PVT induced variations on the delay. The probability, $P_{D_0}(T, t_s)$, was measured by repeating the phase binary challenge $m = 64511$ times. The clock period was constant with $T = 6080.8254$ ps. We acquired 100,000 data points spanning a total of 1600 s. The f_{var} adjustments that is nominally made by the circuit's control system was turned off so that a fixed delay chain could be measured. The measured counter ratios are shown in Figure 3-13. The two intervals highlighted by the red dashed and green dotted lines indicate that over short time intervals (80 s), the measured noise of the

* The results in this section are part of a forthcoming paper in the IEEE Transactions on Instrumentation and Measurement.

ratios is 0.04 (one standard deviation), and that over longer time scales, the ratios vary by 0.5. We verified that σ_m is stable over time for constant delay chain settings over periods

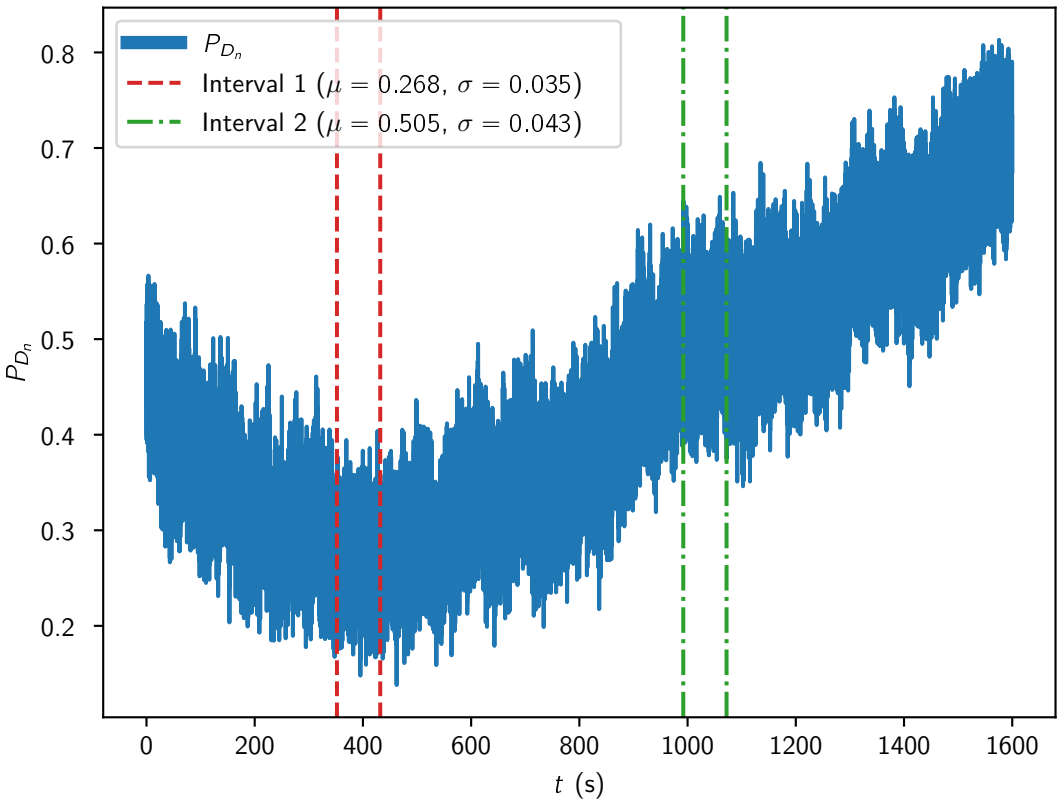

Figure 3-13. Probability of one as a function of time

of 1000 s. The average value of σ_m was 3.12 ps with a standard deviation of 0.11 ps. Using Equation 3–6, the variations of the delay, $D_0(t_s)$, were estimated. The measured delays are shown in Figure 3-14. Over the 1600 seconds, the delay varied by about 5 ps. It is likely that this level of variations over relatively long time intervals is caused by PVT variations. The variations of the delay over shorter time periods was less. For example, the standard deviation of the measured delay was below 0.5 ps on both the red dashed and green dotted intervals shown in Figure 3-14, each of which spanned 80 s.

Spectral density and filtering. The power spectral density of the measured delay over time and plotted in Figure 3-14 is shown in Figure 3-15. The spectral shape is $1/f$ below 1 Hz.

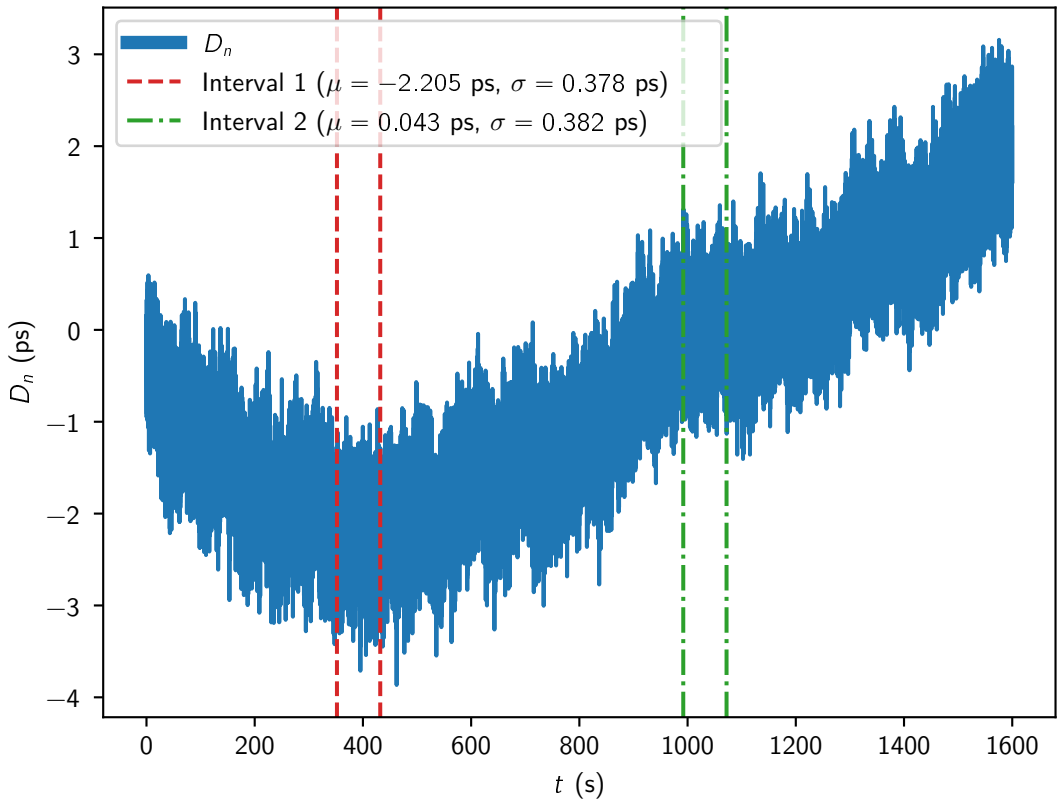

Figure 3-14. Phase difference as a function of time

Above 1 Hz, the spectrum is flat (white noise). Temperature fluctuations commonly exhibit $1f$ behavior, so we attribute the low frequency noise to thermal effects, one of the PVT variations we intended to measure. The white noise floor at the level of $0.02ps^2/Hz$ is consistent with the circuit's measurement noise. A simple low-pass filter is sufficient to obtain the delay variation due to $1f$ noise:

$$D_{Fn}(i) = \frac{63 D_{Fn}(i-1) + D_n(i)}{64} \tag{3–8}$$

Filtered delay estimates are shown in Figure 3-16, and the filtered power spectral density is shown in Figure 3-17. The filter removes spectral content higher than 1 Hz and only requires one multiplication, one addition and one bit-wise shift. It is therefore easy to implement within the control system and it is useful for separating timing variations due to PVT effects from the

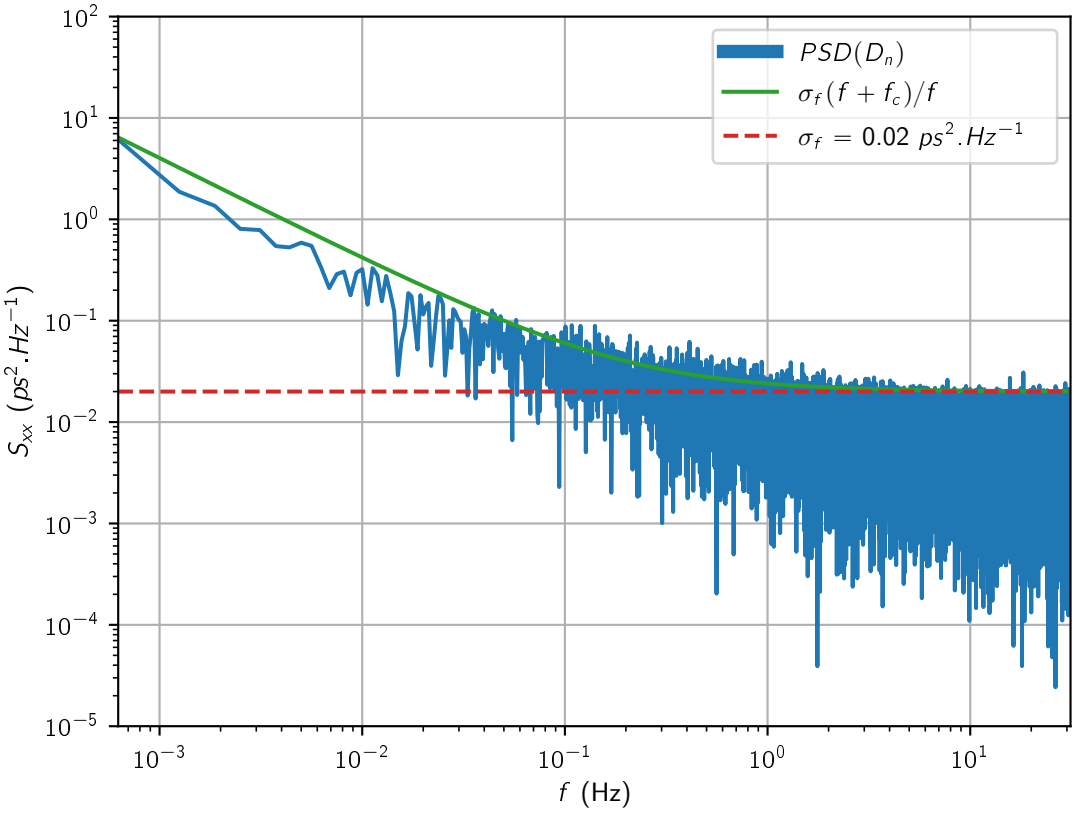

Figure 3-15. Power Spectral Density of D_n, $m = 64511$

intrinsic measurement noise. These results indicate that for the FPGA used and the standard laboratory environment in which these tests were performed, the circuit is capable of tracking thermal variations, aging effects and only slow voltage variations. Variations due to voltage noise typically occur at frequencies higher than 1 Hz. Therefore, we conclude that these results only provide an upper bound on this noise source.

3.3.1.2 Multiple delay calibration

The second test used the circuit to measure a large range of delays. We intentionally generated a set of delays that was larger than the total delay of delay chains used in time converters. Its precision, below 2 ps, is sufficient to calibrate all the elements of these chains and estimate characteristics such as the differential nonlinearities (DNL) of the complete chain. We applied the delay chain method previously described and swept through all the 256

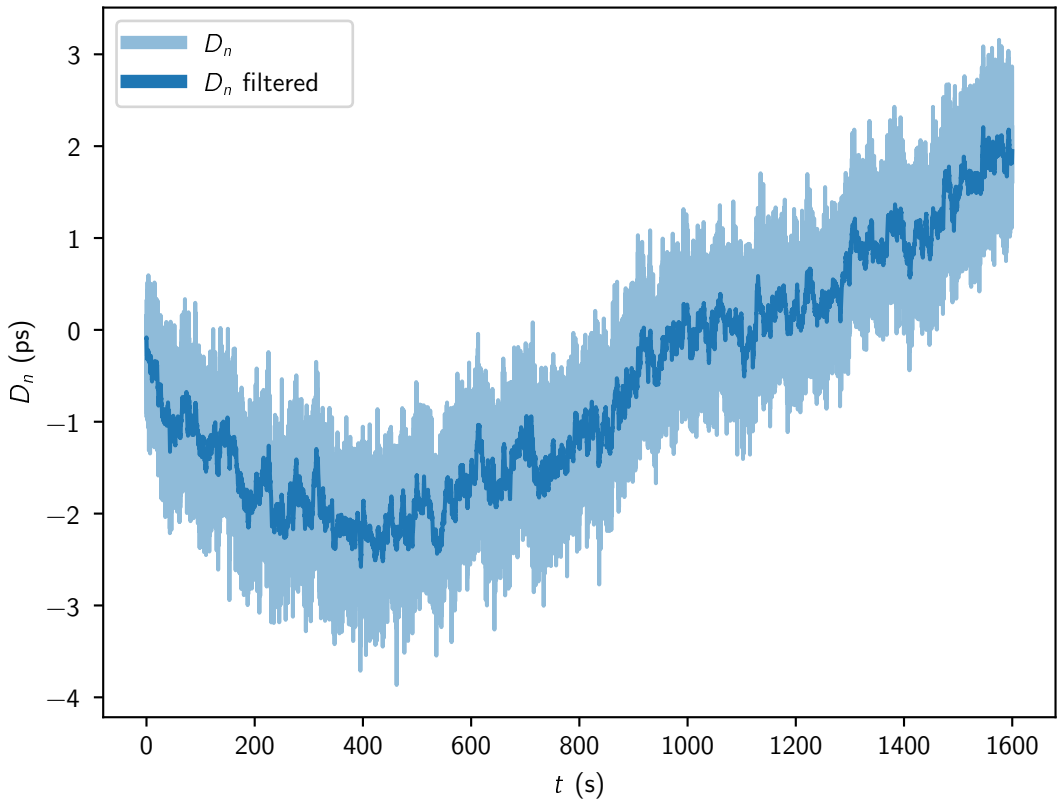

Figure 3-16. Filtered D_n as a function of time

positions on the first setting, and then through all the 256 positions on the second setting. The results are shown in Figure 3-18. We accounted for PVT variations occurring through the calibration process by repeatedly measuring a single element, D_0. We assumed that the PVT effects on the delays are homogenous so that the PVT variations on all delays are proportional to the raw delay, and as such, we used the following equation to scale the delay being measured.

$$D_n(t_0) = D_n(t_s)\frac{D_0(t_0)}{D_0(t_s)} \tag{3–9}$$

The delay with setting n, sampled at time t_0 is estimated to be the delay with the same setting n sampled at time t_s, scaled by the ratio of the reference delay, D_0, sampled at time t_0 and the same delay setting sampled at time t_s. The nonlinearities observed in Figure 7 are due to the

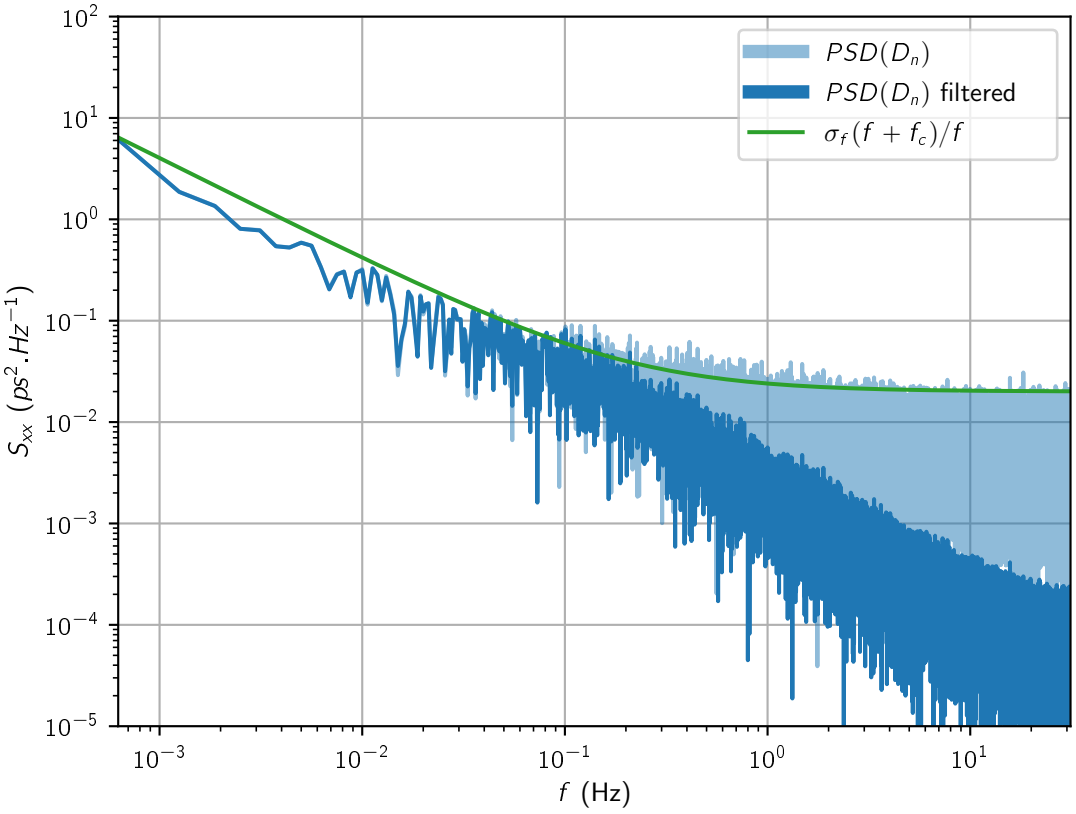

Figure 3-17. Filtered Power Spectral Density of D_n

structure of the FPGA, which is built with a pattern of 12 cells repeated along the delay chain. The maximum delay of the chain is 12 ns, out of which 6ns are adjustable. The adjustment steps are typically 12 ps, with nonlinearites of up to 80 ps.

3.3.1.3 Validation with combinations

As explained in the circuit description, the delay under test is composed of two delay chains, resulting in two independent settings $D_{x,y}$ with $x, y \in [\![0, 255]\!]$. The two adjustable settings can be changed independently, and the total delay is the sum of two individual delays that cannot be independently measured, as they are below the minimum T_{var} period of 4 ns. However, it is possible to measure four different delays that could be combined together to get zero:

$$D_{a,b} + D_{c,d} = D_{a,d} + D_{c,b} \tag{3–10}$$

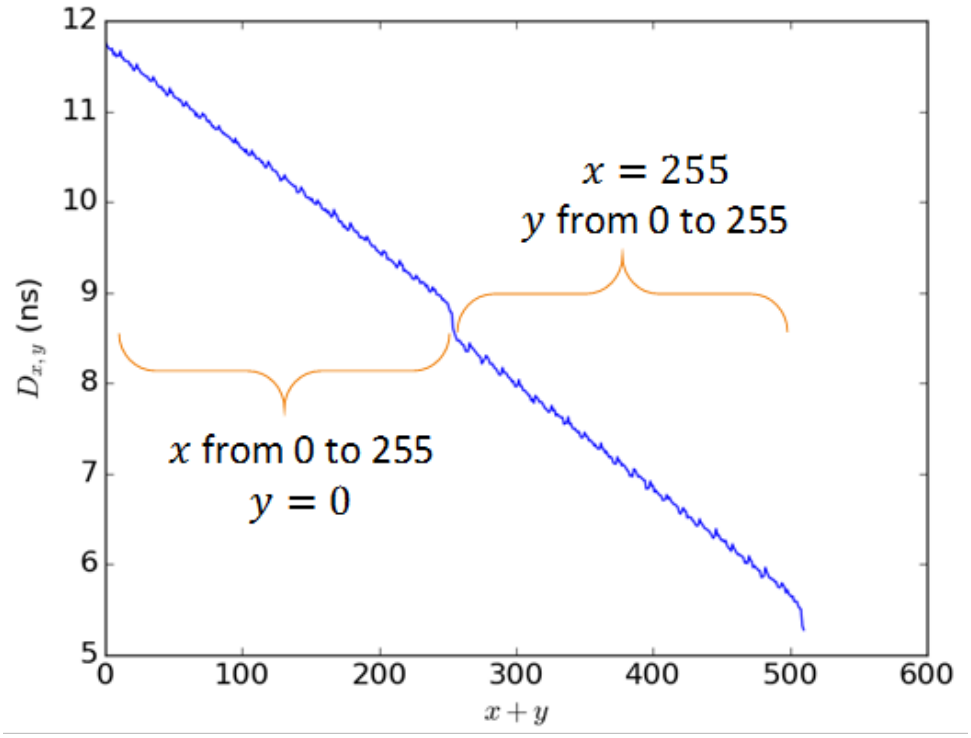

Figure 3-18. Delay chain propagation delay as a function of control input

We define an additivity error with the equation,

$$\epsilon_+(a, b, c, d) = D_{a,b} + D_{c,d} - D_{a,d} - D_{c,b} \tag{3–11}$$

Any error we measure in Equation 3–10 can be used as an upper bound on the bias and frequency dependence in the presented measurement method. The four different delays are measured using different frequencies, f_{var}. The ϵ_+ error includes the frequency dependence of the delays on the arbiter. It also includes the errors in the calibration methods, including the approximation errors associated with Equation 3–9. We measured $D_{x,y}$ for all (x, y) in $\{16 \cdot z \mid z \in [\![0, 15]\!]\}^2$. With 256 delays measured, we extracted a total of 14400 unique combinations (a, b, c, d) that should, in principle, sum to zero. A histogram of the value of $\epsilon_+(a, b, c, d)$ is shown in Figure 3-19. The resulting standard deviation of 1.687 ps is slightly above the values due to the circuit noise, of $\sqrt{4 \cdot 0.4^2} = 0.8$ ps. The biases estimated withϵ_+

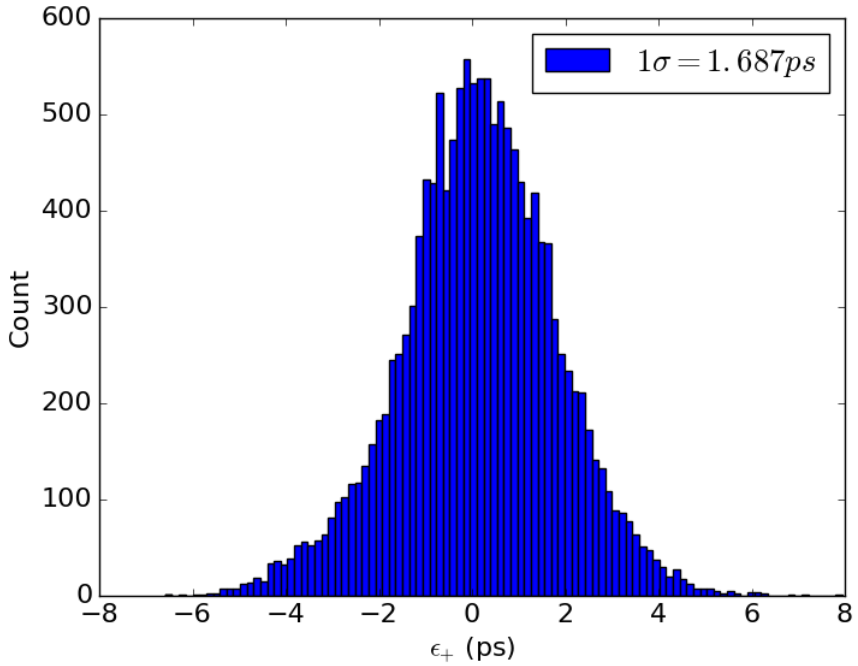

Figure 3-19. Histogram of additivity errors

are well below the typical time/digital converter accuracy of 10 ps. Therefore, this circuit should be suitable to calibrate them.

3.3.2 Seed Laser Pulses

3.3.2.1 Test at 2 Ghz bandwidth

The circuit presented in subsection 3.2.4 has been built and tested, and the test apparatus is shown in Figure 3-21. The test setup includes a 10 MHz reference rubidium oscillator, a fast PIN photodiode, and an oscilloscope. The photodetector has a bandwidth of 8 GHz, and the oscilloscope has a bandwidth of 2 GHz with a sampling rate of 6.25 Gsps. The inputs to the driver circuit are connected to a function generator. The rubidium oscillator is used as a reference by both the function generator and the oscilloscope, and is also used as a trigger for the oscilloscope sampling. The seed laser and the detector are shown in Figure 3-20.

Various settings have been tested, resulting in pulse widths ranging from 300 ps to 1 ns and optical powers between 5 mW and 40 nW. The pulse parameters selected for

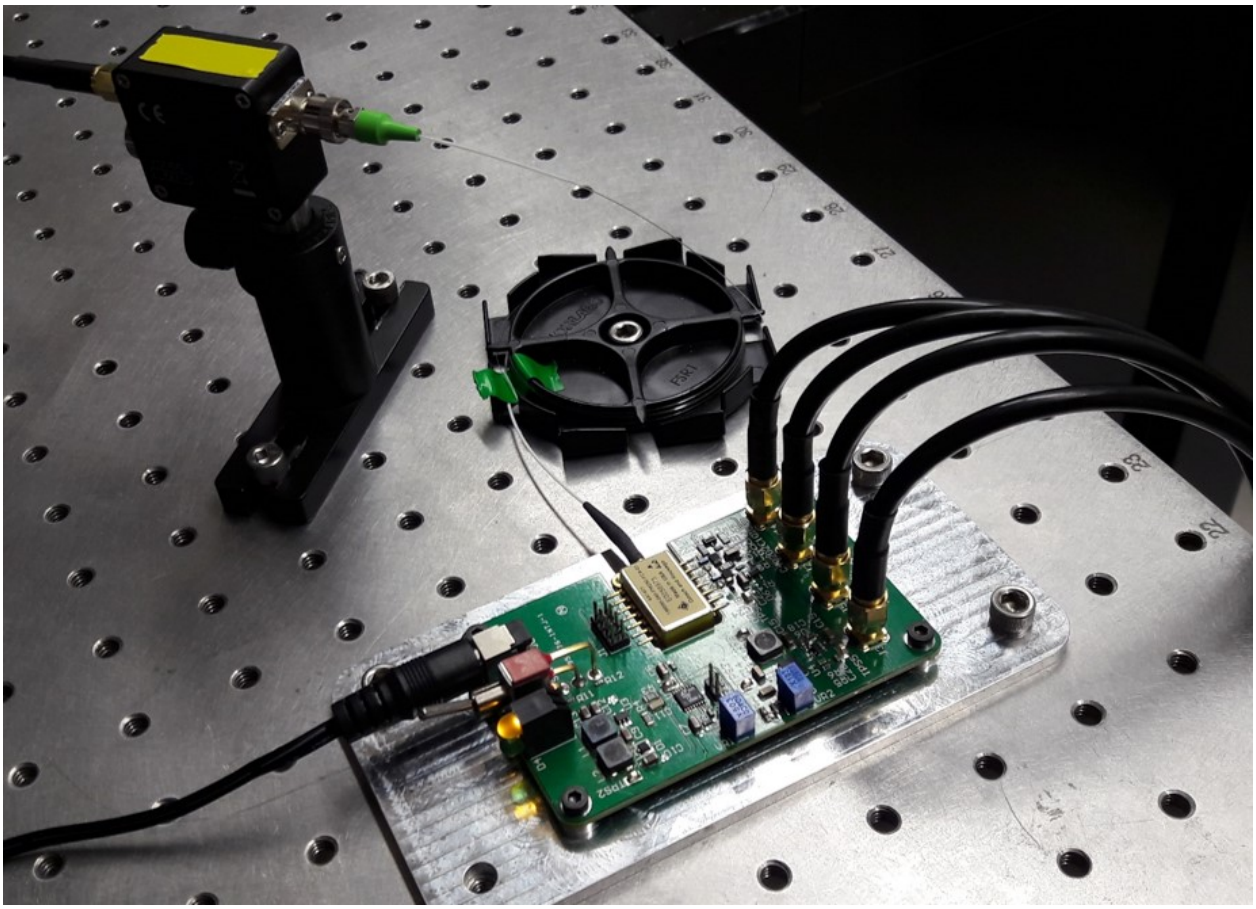

Figure 3-20. Test setup for the seed laser at University of Florida. Image courtesy of author.

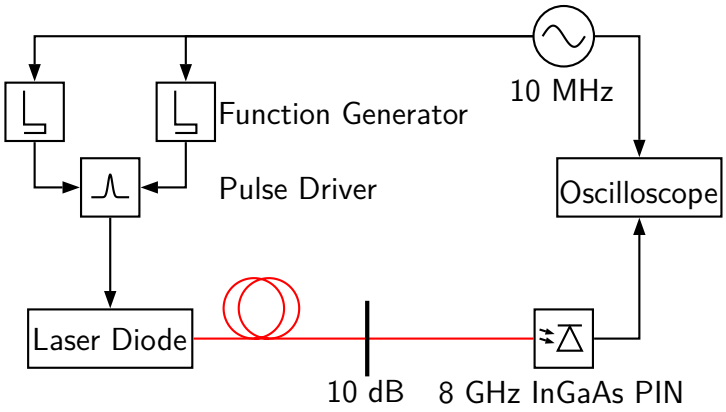

Figure 3-21. Seed laser test setup

characterization is 500 ps long and have a power of approximately 10 mW. A pulses with those parameters is shown in Figure 3-22.

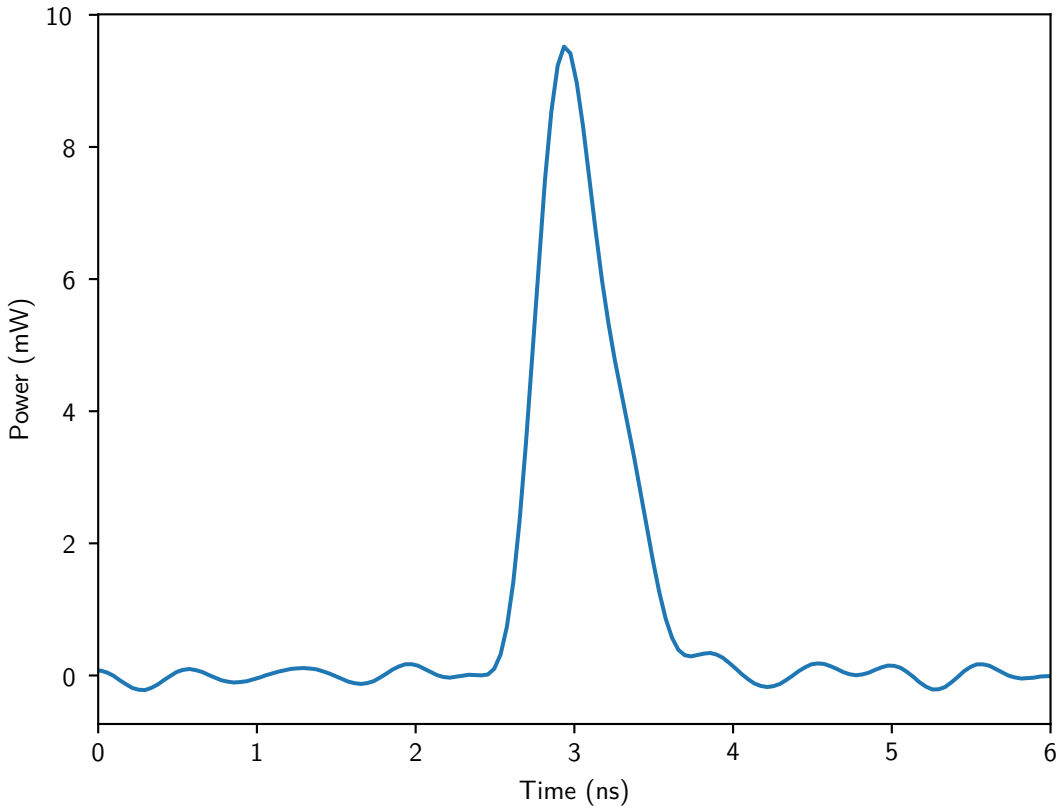

Figure 3-22. A 500 ps seed laser pulse

More than 10,000 pulses were collected, and several parameters have been recorded and plotted in Figure 3-23. Figure 3-23A shows the Full Width at Half Maximum (FWHM) duration of the pulse. The pulse maximum used for the pulse width computation is extracted from each sampled pulse. An histogram of the maximum power is shown in figure 3-23B. The power is estimated from a previous calibration of the PIN detector and is affected by proportional errors due to fiber connectors and uncertainties is the value of the density. The relative dispersion, estimated to be 2.7% for this test, is not directly affected by the calibration error. Figure 3-23C is a histogram of the position of the rising edge of the pulse from the sampling trigger signal. The measured standard deviation σ_r is the quadratic mean

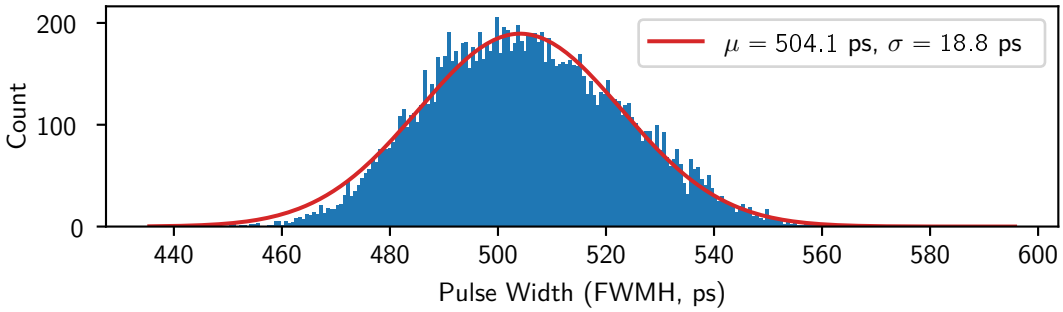

A

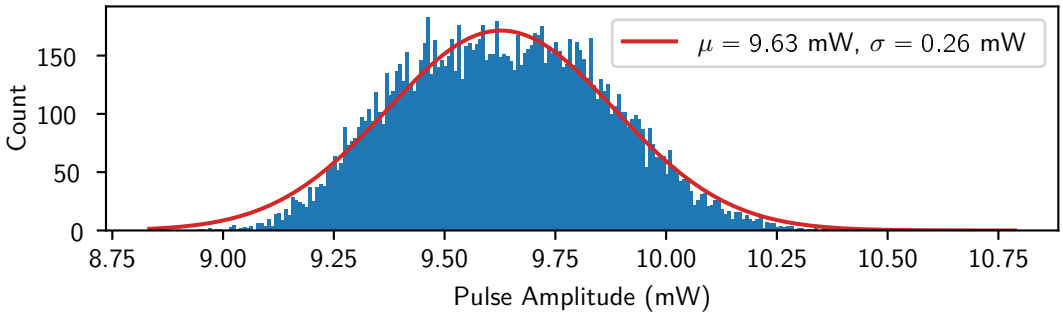

B

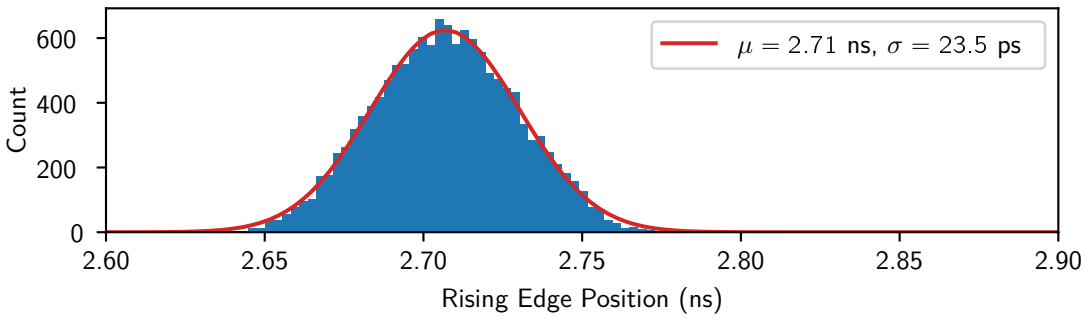

C

Figure 3-23. A) Pulse duration, B) Pulse maximum power, C) Rising edge position for 13654 pulses of Figure 3-22

of the function generator additive jitter σ_f, the driver circuit and laser additive jitter σ_c, the oscilloscope sampling channel and photodetector jitter σ_{os} and finally oscilloscope trigger channel jitter σ_{ot}:

$$\sigma_r = \sqrt{\sigma_f^2 + \sigma_c^2 + \sigma_{os}^2 + \sigma_{ot}^2} \qquad \sigma_c < \sigma_r = 23.5\text{ps} \tag{3–12}$$

Since the function generator and the oscilloscope share the same reference, the errors due to time-base noise are considered negligible. The jitter due to the trigger σ_{ot} is highly dependent on trigger channel gain and threshold and was contributing to the measured jitter by more than 100 ps with low gain settings. From Equation 3–12, we can estimate that the additive jitter of the seed laser driver is below 23.5 ps. The additive jitter can also be estimated with the pulse duration. In this case, the noise in the pulse width σ_w does not depend on the trigger σ_{ot}. If we assume that the rising and falling edge positions are statistically independent, then the pulse width standard deviation can be expressed as:

$$\sigma_w = \sqrt{2(\sigma_f^2 + \sigma_c^2 + \sigma_{os}^2)} \qquad \sigma_c < \sigma_r/\sqrt{2} = 13.3\text{ps} \tag{3–13}$$

This leads to a lower estimate of the additive jitter of the seed laser driver, not affected by noise due to the oscilloscope trigger. However, this is based on weaker assumptions. Finally, the contribution of the function generator has not been estimated with this setup. Since 23.5 ps is well below the best recorded performance for detection and time-to-digital conversion, the demonstrated jitter is deemed sufficient, and further improvement will not contribute to the accuracy of the overall system.

Figure 3-24 shows the pulse of Figure 3-22 in the frequency domain. Part of the pulse signal is beyond the bandwidth of the oscilloscope, at 2 GHz. The frequency of relaxation oscillations for the selected laser is greater than 5 GHz. Gain-switching is equivalent to selecting the first relaxation oscillation by shutting down pumping. This indicates that pulses shorter than 200 ps could be achieved. However, they are not measurable with this set-up. The receive channel has a bandwidth limited to 1 GHz. Because of that, pulses significantly shorter

than 500 ps would be integrated by the detector and are of limited interest for the transmitter presented in this work. However, shorter pulses benefit long range, deep-space communication where peak-power is the prime objective.

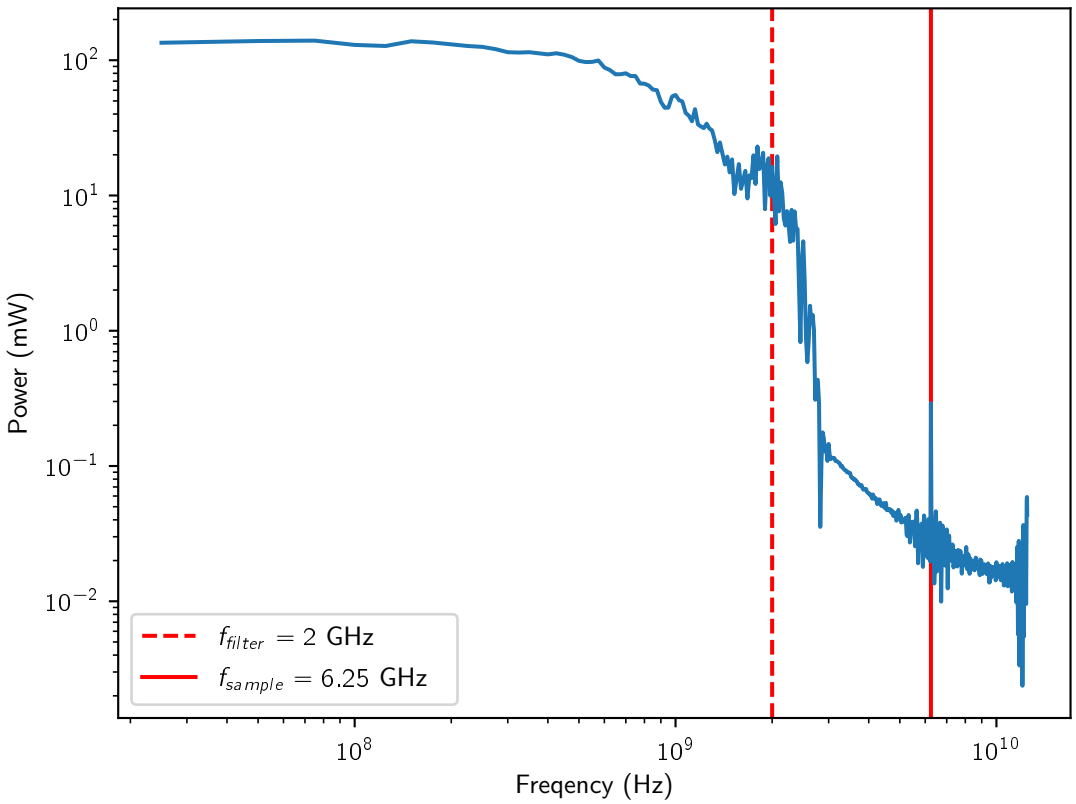

Figure 3-24. Fourier transform of the pulse in Figure 3-22

3.3.2.2 Testing at 10 Ghz bandwidth

As Figure 3-24 showed, the high frequency part of the pulses cannot be measured with a 2 GHz oscilloscope. Kerri Cahoy has offered the help of the STAR Lab at MIT to complete a measurement at a higher bandwidth.

The test setup in the previous section, Figure 3-21, have been replicated, but with faster instruments, shown on Figure 3-25. The photodetector bandwidth used was 20 GHz. The oscilloscope had a bandwidth of 10 GHz, and the function generator is replaced by a pair of pattern generators capable of generating 12.5 Gbps. Although the instrument's bandwidth was

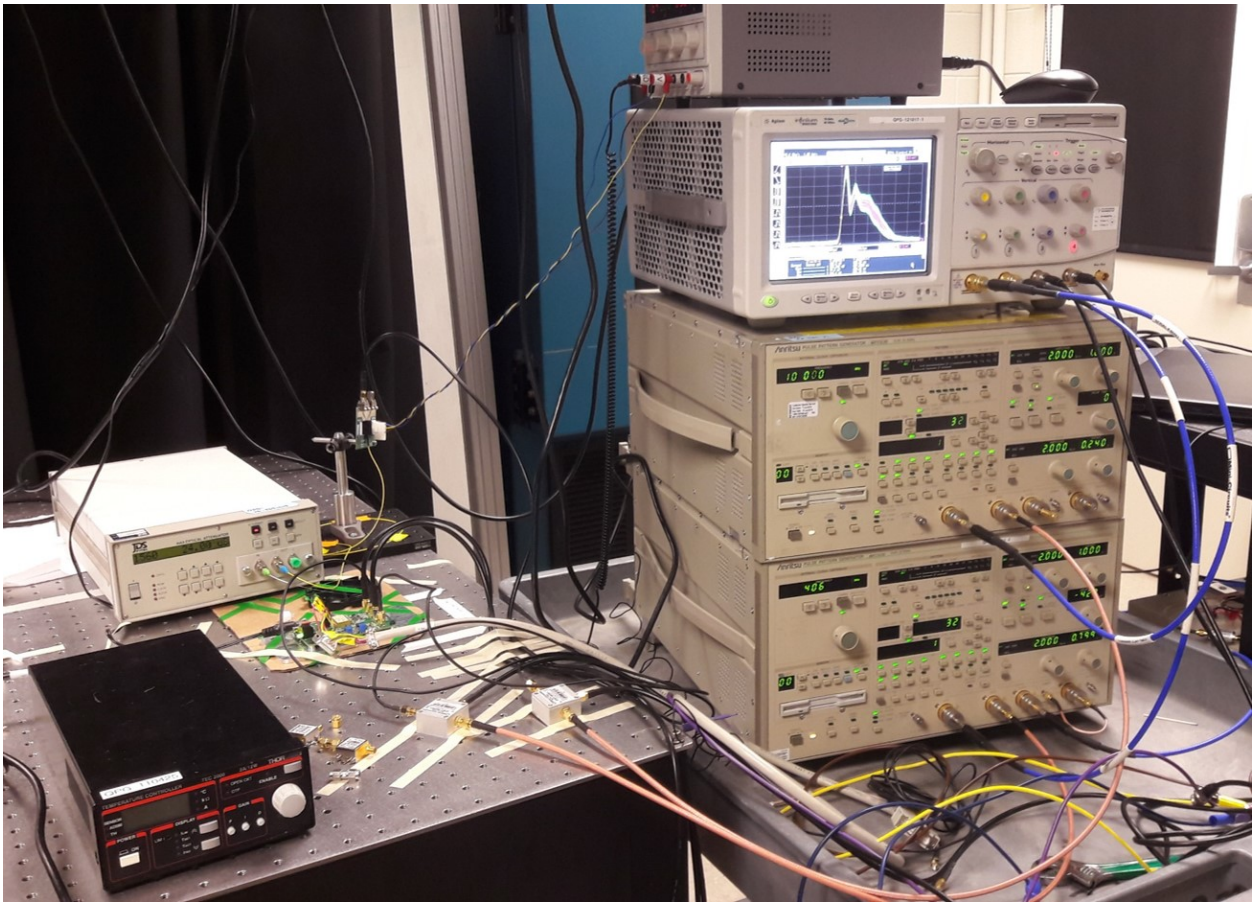

Figure 3-25. Test setup for the seed laser at MIT STAR Lab. Image courtesy of author.

greatly increased, the pattern generators were not able to reach the turn-on threshold of the FET buffers with a 50 ohm load, and bias tees had to be used to raise the trigger voltage, also introducing distortions. The photodetector was not calibrated. Its output voltage could not be related to the laser optical power.

Figure 3-26 shows the turn-on dynamics of the laser and confirms the existence of gain-switching for the selected laser. The light output suddenly rises before stabilizing on the commanded ramp, after a few oscillations.

Figure 3-27 shows the profile of 1 ns pulses. The rising edges are steeper than the falling edges due to gain-switching. The falling edge time uncertainty does not follow a Gaussian distribution as expected. The peak-to-peak time error is around 200 ps.

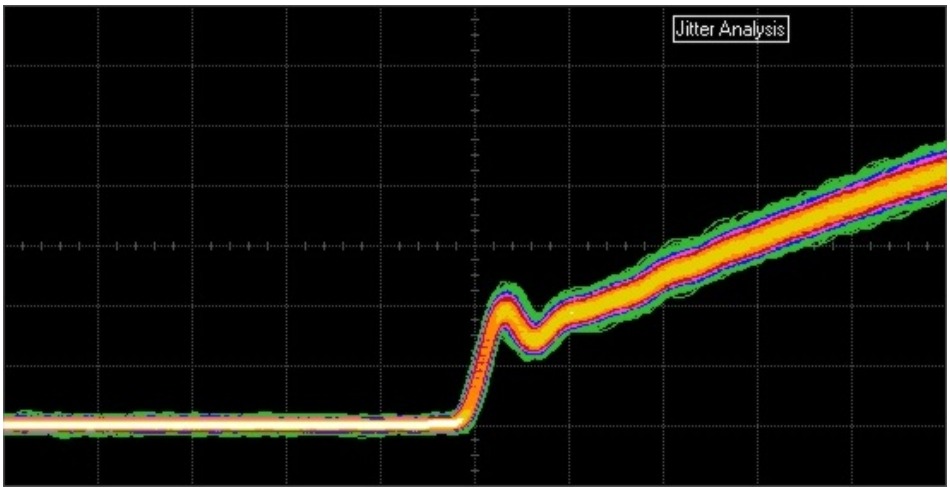

Figure 3-26. Laser turn-on with gain-switching, 200 ps per division

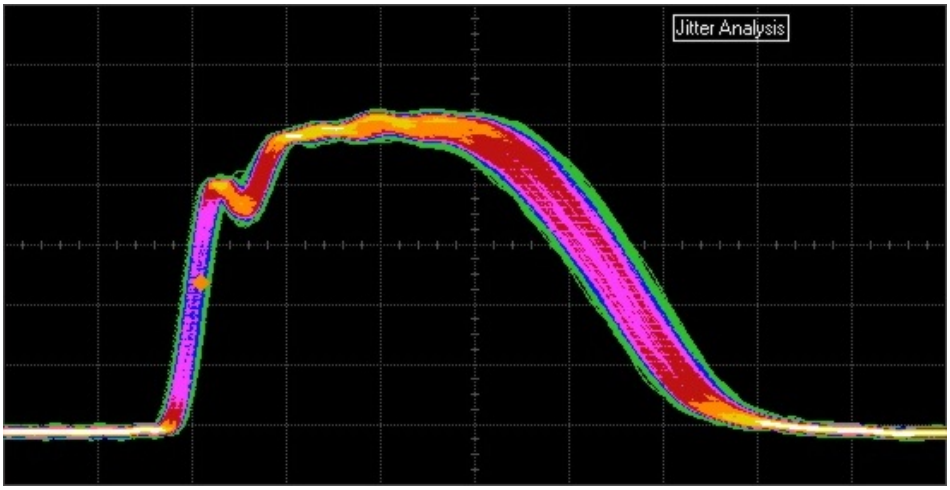

Figure 3-27. 1 ns pulses aligned on reference clock, 200 ps per division

Figures 3-28A and 3-28B both depict the same 100 ps pulses. For 3-28A, sampling is triggered by the reference oscillator of the pattern generator, for 3-28B sampling is triggered by the pulses themselves. Figure 3-28A shows again that the jitter is not Gaussian, and is close to 200 ps peak-to-peak. The jitter was lower on the previous test, with the 2 GHz oscilloscope, and the reduced bandwidth of the previous setup does not impact phase uncertainties. The pulses in figure 3-28B are not displaying high frequency noise on the rising edge that could have been filtered by the 2 GHz limit on the previous experiment. The higher jitter could be due to the marginal control signal amplitude. As the turn-on threshold is placed higher on the

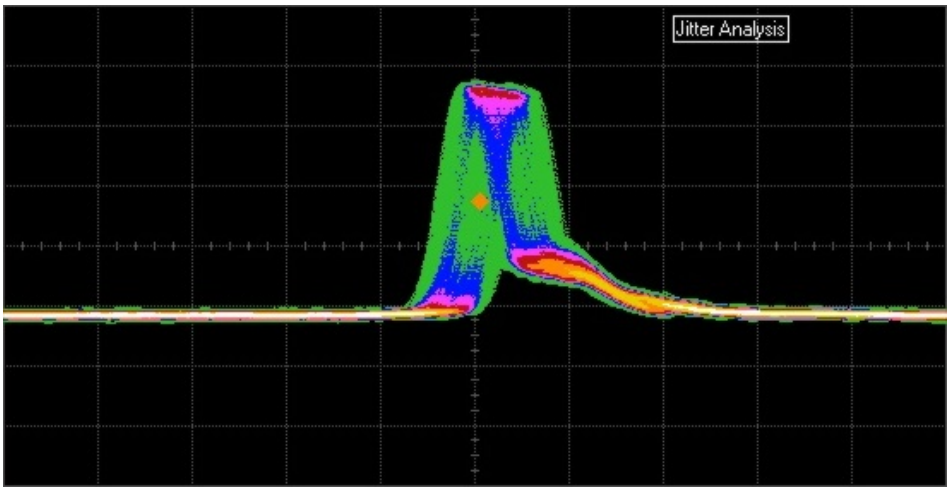

A

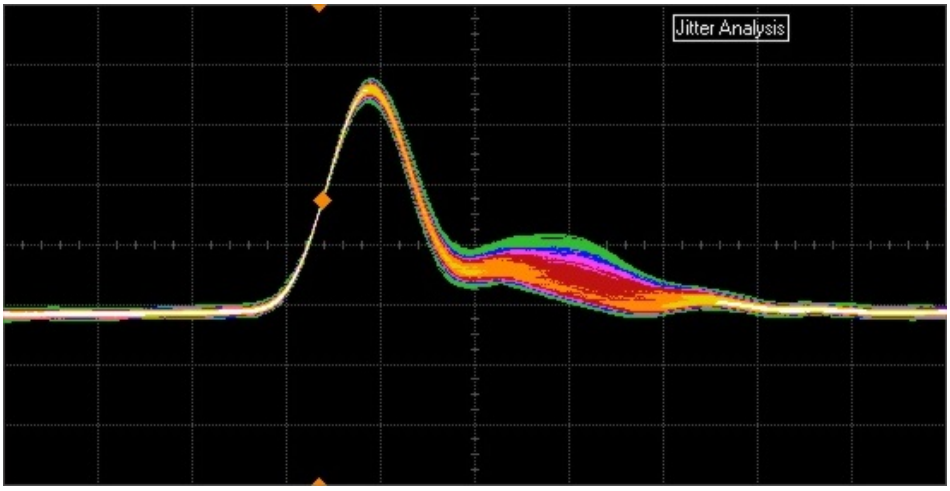

B

Figure 3-28. A) 100 ps pulses aligned to the reference clock, 200 ps per division. B) 100 ps pulses self-triggered, 100 ps per division.

rising edge of the input signal, the slope gets smaller, and the same amount of voltage noise results in a higher jitter.

The pulses on figure 3-28B are stable in time, with full-width half-maximum duration variation of less than 2 ps RMS. The cavity dynamics behave like a harmonic oscillator, forcing the pulse duration to one period of its natural resonant frequency.

Improvements to the laser driver, in particular the addition of comparators or differential signal receivers to the FET buffer would reduce the driving signal requirements, and allow the circuit to be driven directly from an FPGA.

3.3.2.3 Extinction ratio

The extinction ratio of the seed laser has been estimated with the method described by (80). The extinction ratio is equal to the pulse high level divided by the pulse low level. This ratio is one of the limiting factors on the usefulness of high PPM order: as the PPM order increases, the EDFA charge time increases and its gain rises. The seed low level light is then more and more amplified by the EDFA, reducing the EDFA high level population and limiting its gain. The seed laser driver was tuned to obtain 5 ns pulses, and the pulse repetition rate was then adjusted to lower the duty cycle. An optical power meter with a high dynamic range measured the average light intensity as a function of the duty cycle. The result is plotted in Figure 3-29.

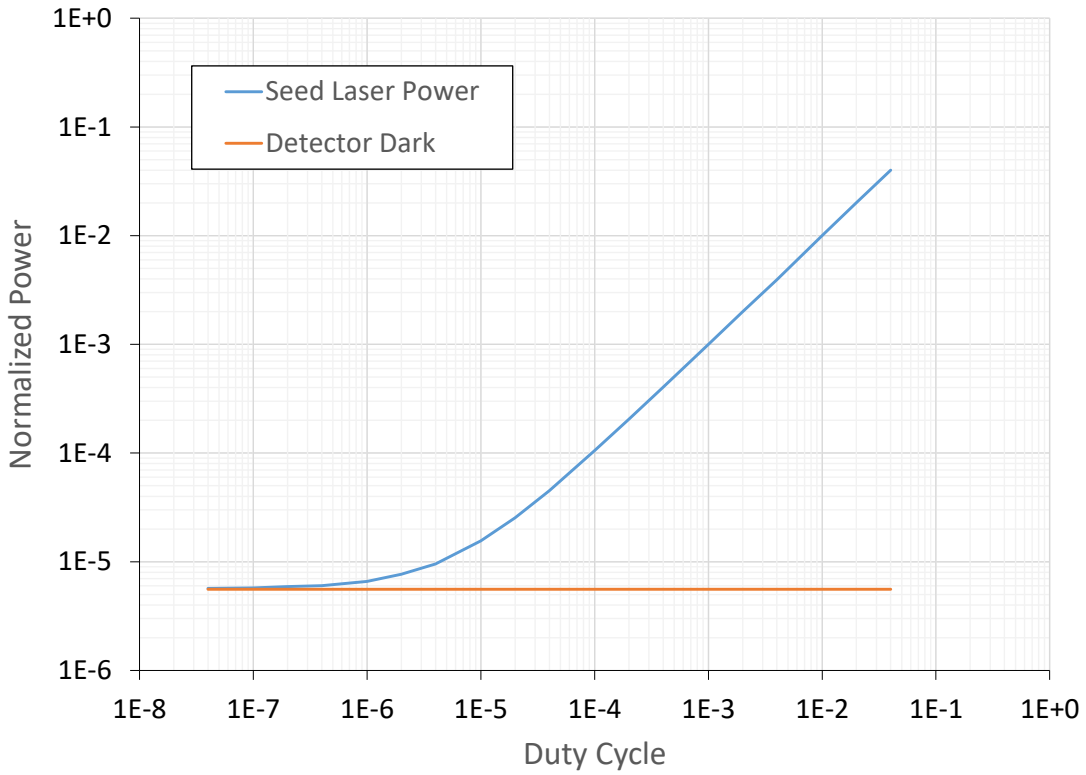

Figure 3-29. Normalized power as a function of duty cycle, used to determine the extinction ratio.

The proportional part of the seed laser curve indicates that the test setup is working correctly: the average power from the seed laser is proportional to its duty-cycle as expected.

The measurement of the low level power is limited by the detector range. The extinction ratio is greater than 50 dB (10·Log). This result is expected since no mechanism has been identified that results in optical power when the laser is not powered.

3.3.3 Modulated String Example

The prototype setup for MOCT has been used to demonstrate the emission of a short string, through the SDPM and the seed laser. To drive the prototype seed laser electronics board from the FPGA, a two of operational amplifiers wired as line driver were required. Because of slew rate limitations with the line driver circuits, the repetition rate of the setup was limited to 10 MHz, instead of 20 MHz. The data was encoded in PPM 32, with a subset of ASCII listed in Table 3-5.

Table 3-5. Encoding for modulated string test.

Symbol number	0	1	25	26	27	28	29	30	31
Value	'a'	'b'	'z'	'!'	Space	'?'	'.'	','	Newline

The raw, uncoded data rate demonstrated with this test is 50 Mbps. The PPM slots were 930 ps wide, with a guard time of 70 ns to partially simulate 20 MHz operations. The pulse duration was around 2.5 ns. The light from the seed laser was sent to an InGaAs PIN photodiode, connected to a real-time oscilloscope. The characters were extracted from the sampled signal, plotted in Figure 3-30. The test was successful at PPM 32, but constant modulation errors reaching up to 120 ps were measured.

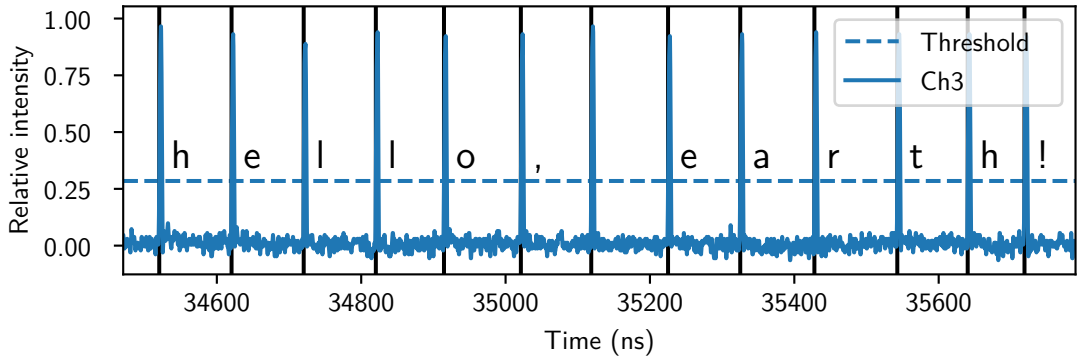

Figure 3-30. Exemple of a modulated string at 10MHz, 32-PPM (50 Mbps) (2)

3.3.4 Bit Error Rate

Since MOCT is a timestamp-based modulator, it is highly flexible and can independently adjust pulse duration, modulation order M, slot time τ, and guard time T_g. It is possible to change the order of the PPM modulation M while keeping T_g and $M \cdot \tau$ constant. This allows the data rate to be changed without any impact on the laser system, but it requires increasing the timing accuracy. The jitter must be reduced proportionally with M while the data rate is increased by a factor of only $log_2 M$.

3.3.4.1 Errors from Jitter

A complete noise budget for a free-space optical channel is outside the scope of this work due to its complexity, and also because the receiving channel of MOCT is still under design and validation. A jitter term noted $\sigma^2_{Channel}$, includes noise due to the EDFA amplification, noise from free-space propagation and optics devices, noise in the detection devices, and errors due to amplitude variations. This term could be determined in the amplitude domain from the seed laser to the receiver threshold, and then converted to the time domain. The performance of OPTI, presented in the first part of this dissertation can be used as a first estimation, around 100 ps. The seed laser additive jitter was found to be Gaussian and measured in subsubsection 3.3.2.1, below 23.5 ps. The random noise from the time-to-digital conversion has been estimated at 50 ps and was also following a Gaussian distribution. Jitter from all parts of the chain can be added in quadrature: $\sigma = \sqrt{\sigma^2_{Modulator} + \sigma^2_{Seed} + \sigma^2_{Channel} + \sigma^2_{TDC}}$. Once the jitter of the complete channel is determined it is possible to compute the bit error rate from probabilities. Figure 3-31 shows the areas associated with errors or correct symbol for jitter with a Gaussian distribution.

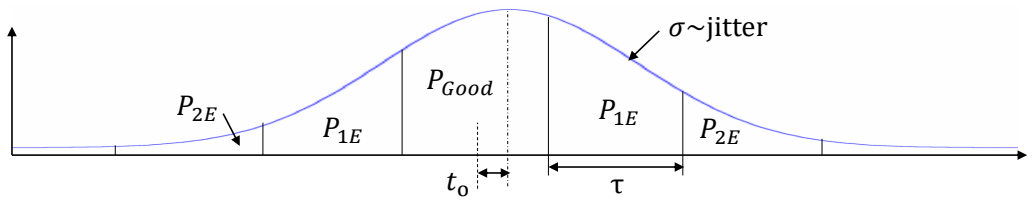

Figure 3-31. Error probabilities

In Figure 3-31, σ is the total, end-to-end, random jitter and t_o is an offset due to deterministic modulation errors and inter-symbol cross-talk. The term τ is the duration of a time slot for a M-PPM modulation scheme. P_{Good} is the probability of a symbol to be correctly transmitted. P_{Good} is equal to the ratio between the area under the Gaussian curve labeled as P_{Good} and the total area under the curve. It can be computed with Equation 3–14.

$$\begin{aligned} P_{Good} &= \frac{1}{2\sqrt{\pi}} \int_{T_{Good}} e^{\frac{-t^2}{2}} dt \qquad T_{Good} = \left[\frac{t_o}{\sigma} - \frac{\tau}{2\sigma}, \frac{t_o}{\sigma} + \frac{\tau}{2\sigma} \right] \\ P_{Good} &= CDF\left(t_o + \frac{\tau}{2}\right) - CDF\left(t_o - \frac{\tau}{2}\right) \end{aligned} \tag{3–14}$$

If we assume that a symbol error means that all the information carried by that symbol is lost, then $BER = 1 - P_{Good}$. However, if the binary data encoded in each PPM symbols is ordered following a Gray code, then the BER is lowered. Gray codes guarantee that two PPM symbols that are n-slots apart will have an Hamming distance of at most n, that is to say that at most n bits will be different. For example, two PPM symbols in neighboring slots, with distance of 1 slot, will be encoded with only a 1 bit difference. PPM symbols 3 slots apart (2 non-signaled slots in between) will have at most a difference of 3 bits. To refine our estimation of the BER, we need to compute the probability of having a pulse in each slots, depending on the number of invalid bits. Equation 3–15 gives the probability for n bits to be wrong.

$$\begin{aligned} P_{nE} =& CDF\left(t_o + n\tau + \frac{\tau}{2}\right) - CDF\left(t_o + n\tau - \frac{\tau}{2}\right) \\ &+ CDF\left(t_o - n\tau - \frac{\tau}{2}\right) - CDF\left(t_o - n\tau + \frac{\tau}{2}\right) \end{aligned} \tag{3–15}$$

Equation 3–15 does not take into account the beginning and the end of the time with PPM slots. It can also over-estimate the number of invalid bits, a symbol distant of n slots may only have a difference of 1 bit instead of n. Because of that, the resulting BER will still be an upper-bound of the actual value. An M-PPM scheme can encode $\log_2 M$ bits. There is no point to calculate the probability for more than $\log_2 M$ bits to be wrong. With $n > \log_2 M$, the complete symbol is considered lost. The probability for this case is given by Equation 3–16.

$$P_{out} = 1 - CDF\left(t_o + \log_2 M\tau + \frac{\tau}{2}\right) + CDF\left(t_o + \log_2 M\tau - \frac{\tau}{2}\right) \tag{3–16}$$

The Bit Error Ratio is the expected value of the ratio of incorrect bits over the total number of bits. For one PPM symbol, the expected value of the number of incorrect bits is the probability of n bits to be incorrect, P_{nE}, multiplied by n. The cases for $n > \log_2 M$ are covered by $\log_2 M \cdot P_{out}$. The total number of bits is $\log_2 M$. This lead to Equation 3–17:

$$BER_r(\sigma, \tau, t_o, M) = P_{out} + \frac{1}{\log_2 M} \sum_{n=1}^{\log_2 M} nP_{nE} \tag{3–17}$$

The BER values from Equation 3–17 have been plotted as a function of random jitter in Figure 3-32. The figure cover various order of PPM modulation, for deterministic errors of 120 ps as currently observed, and errors 10 ps for ideal performances, close to the level of the calibration errors in the SDPM. In this graph, the offset t_o is noted ϵ_{cal} . The asymptotic behavior of the curve for PPM128, with $\epsilon_{cal} = 120$ ps when the jitter tend to zero is due to the fact that the center of the error distribution is outside of the correct PPM slots, because ϵ_{cal} is higher than half the size of a slot. When the spread due to the random error is reduced, the probability of getting 1 wrong bits out of 7 increase since the distribution center is outside the correct slot.

3.3.4.2 Errors from Insertion/Deletion

The BER from Equation 3–17 does not take into account pulses that are not detected (deletion) or pulses detected but not emitted, due to noise or other light sources (insertion). Insertion are frequent with single-photon detection systems associated with long range links. Errors due to timing noise are called replacements: the symbol detected is not the symbol being emitted. Replacements can easily be detected and corrected by Forward Error Correction Codes (ECC). The impact of insertions and deletions is different. They must be detected to be corrected with traditional error correction codes. Detection of missing or extra pulses in guaranteed with PPM, and only one symbol is affected, so this case is analogous to a replacement. With DPPM, detection is not systematic: if a pulse is inserted at a time T_i after the previous pulse, with $T_i > T_g$ and $T_i < M \cdot \tau$, the insertion is not detected. If next emitted pulses is detected at a time T_v after the inserted pulses, with $T_v > T_g$ and $T_v + T_i < M \cdot \tau$,

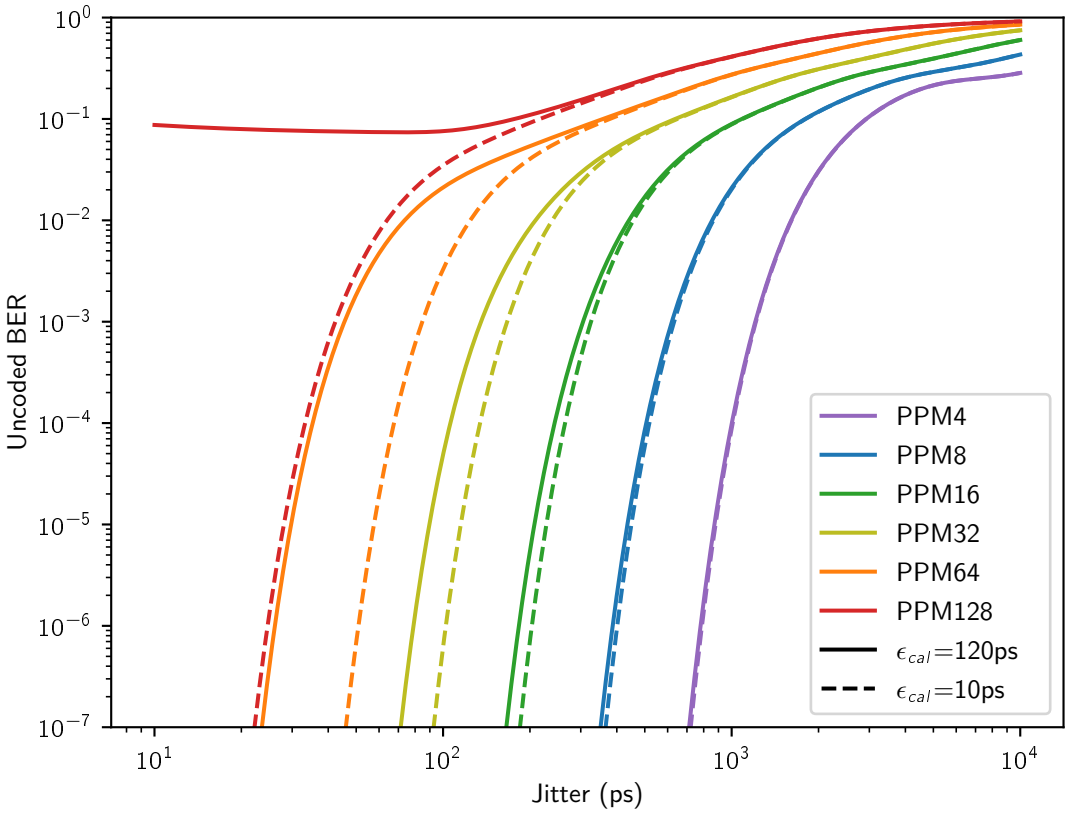

Figure 3-32. Bit error rate as a function of jitter

then the insertion is not detected at the next pulse, and all incoming data is shifted by one symbol. Deletion can also go unnoticed. If the time interval between the two detected pulses T_d is lower than $M \cdot \tau$. If $T_g > M \cdot \tau$, insertions and deletions cannot happen unnoticed.

None of the usual and modern ECC, like low-density parity-check codes or Turbo codes can effectively cope and correct an undetected insertion/deletion, at a minimum a complete packet will be lost. The data throughput gain G_{mod} between PPM and DPPM can be determined from Equation 1–17 and Equation 1–18.

$$G_{mod} = \frac{M\tau + T_g}{\frac{(M+1)\tau}{2} + T_g} \tag{3–18}$$

If the loss of a complete packet must be avoided, then $T_g > M \cdot \tau$ and Equation 3–18 becomes:

$$G_{mod} < \frac{4M}{3M+1} \tag{3–19}$$

If error-free communication is required, the gain in data throughput of DPPM over PPM is at most $4/3$. If insertion/deletion were to be detected by a dedicated code, G_{mod} is at most equal to 2. Any code with a rate below 0.5 would be detrimental and non-differential PPM would be superior.

If the probabilities of insertions P_i and deletions P_d are known, then the BER formula in Equation 3–17 can be completed:

$$BER_{PPM}(\sigma, \tau, t_o, M) = P_i + P_d - P_i P_d + (1 - P_i - P_d + P_i P_d) \cdot BER_r(\sigma, \tau, t_o, M) \tag{3–20}$$

For DPPM, insertions and deletions imply the loss of two symbols. Since all pulses are coded by the time interval between two pulses, the jitter of both pulses must be taken into account, resulting in a time uncertainty of $\sqrt{2}\sigma$. With $T_g > M \cdot \tau$, Equation 3–17 becomes:

$$BER_{DPPM}(\sigma, \tau, t_o, M) = 2P_i + 2P_d - 2P_i P_d + (1 - 2P_i - 2P_d + 2P_i P_d) \cdot BER_r(\sqrt{2}\sigma, \tau, t_o, M) \tag{3–21}$$

The yield of DPPM over PPM is further reduced by the impact on BER.

Because of the factors listed in this subsection, DPPM lacks a clear advantage over PPM for long range optical communication systems. The use of DPPM is not recommended for MOCT.

CHAPTER 4
CONCLUSION AND RECOMMENDATIONS FOR FUTURE RESEARCH

4.1 Conclusion

Two devices have been designed through this research. The first one is a precision time-transfer instrument. Through four iterations, the design has been refined to reach record-low size, weight and power. The final version can keep track of time with less than 300 mW, and can perform time transfer with less than 5 W. Each instrument channel is smaller than 10 by 10 by 3 cm. The instrument precision is better than 80 ps on ground tests. This is comparable to the on-orbit performances of the T2L2 mission, with a much reduced cost, size and power but at the cost of reliability, temperature control and sensitivity, and also oscillator stability.

The second device is a modulator for free-space laser communication. It is entirely implemented in a FPGA, and only require a clock signal as a reference for calibration. The modulator uses timestamps to process and generate pulses with a counter and delay chains. The modulator integrates a calibration circuit with a measured accuracy below $1\sigma = 2$ ps. The calibration circuit can both map the delay chain and track environmental effects in real time. The modulator has been tested with an output rate of 20 MHz, and could be pushed to 50 MHz. A laser driver for pulsed optical communication has been built. This driver is capable of generating pulses using gain-switching. The pulses can be arbitrarily long, and as short as 100 ps with the selected laser. The pulses are stable, with a jitter bellow 25 ps and relative amplitude variations smaller than $1\sigma = 3\%$. This driver is robust and does not require advanced RF layout techniques. Together, the modulator and the seed laser have been used to generate a test communication string. This short example has demonstrated communication at 100 Mbps.

4.2 Future Work on CHMOPTT and CLICK

CHOMPTT is scheduled to launch in May of 2018. First results are expected soon after and will need to processed and interpreted. OPTI is capable of different experiments. The

clock of each channel can be compared and time transfer can be attempted with both channels at the same time if the satellite power allows it.

CLICK development will continue through the next years, targeting a launch in 2019. A detection channel based on an APD and a TDC is being designed, along with an electronics board including an FPGA for the modulator. The modulator/demodulator system is expected to reach 100 Mbps in 32-PPM, at a range of up to 1000 km.

4.3 Recommendations for Future Research

In the instrument in the first part of this dissertation, all the components from the APD to the TDC have been selected with minimum delay and low temperature sensibility in mind. They are still expected to show some variations with changing thermal conditions. To model the temperature effects, the instrument channels have been outfitted with two diode temperature sensors, and the instruments is capable of logging the temperature of the CSAC. Characterizing and modeling these effects with thermal-vacuum test could improve the results through post-processing. A set of two instrument channels, used as engineering models and identical to the flight boards are available. More generally, the instrument lacks amplification and gain control on the detection chain. This aspect should be improved if next generations of OPTI are needed.

The pulse modulator in the second part of this work can be improved. The calibration circuit has shown great promise, with a great accuracy and a fast rate of measurement. However, the accuracy of the modulator lags behind the calibration circuit. Static errors of up to 120 ps have been measured. This is not an obstacle for CLICK, and for long range optical communication purposes, the shot noise and the single photon detector time uncertainties limit the useful to about 50 ps. However, there could be other application to an high-rate, high-accuracy digital-to-time converter, and through improvements to the delay chain and more advanced deterministic jitter modeling, the modulators error could be reduced to few tens of ps and reach performances unavailable to fast counters or serialization circuits.

The seed laser driver in the second section has a very high extinction ratio. Because of its limited pulse repetition rate, below 40 MHz, it cannot be used for high-throughput communication, in the Gbps range. On the other hand, it can be used with high-peak power fiber amplifiers similar to LIDAR lasers. A similar circuit would be a good starting point for a CubeSat-sized communication system beyond Earth orbit, around the moon or beyond. This system could be made compatible with existing or under developments ground stations such a NASA's Deep Space Optical Communications (DSOC).

APPENDIX A
DERIVATION AND COMPUTATION OF THE ALLAN VARIANCE

The general M-samples variance, with sampling period T and sample time τ, is by defined by (8)[1] as:

$$\sigma_y^2(M,\, T,\, \tau) = \frac{1}{M-1}\left\{\sum_{i=0}^{M-1}\left[\frac{x(iT+\tau)-x(iT)}{\tau}\right]^2 - \frac{1}{M}\left[\sum_{i=0}^{M-1}\frac{x(iT+\tau)-x(iT)}{\tau}\right]^2\right\} \tag{A–1}$$

We will focus on the special case of $M = 2$. Also, since all the oscillators observations in this work will be performed with timestamps, the sampling period T is equal to the sample time τ. As shown in Equation 1–3, the sampled timestamps $x(t)$ provide a countnious observation of $y(t)$.Equation A–1 can be writen as:

$$\sigma_y^2(2,\tau,\tau) = \sum_{i=0}^{1}\left[\frac{x_{i+1}-x_i}{\tau}\right]^2 - \frac{1}{2}\left[\sum_{i=0}^{1}\frac{x_{i+1}-x_i}{\tau}\right]^2 \qquad \text{with} \qquad x_k = x(k\tau) \tag{A–2}$$

$$\sigma_y^2(2,\tau,\tau)|_k = \left[\frac{x_{k+1}-x_k}{\tau}\right]^2 + \left[\frac{x_{k+2}-x_{k+1}}{\tau}\right]^2 - \frac{1}{2}\left[\frac{x_{k+1}-x_k}{\tau} + \frac{x_{k+2}-x_{k+1}}{\tau}\right]^2 \tag{A–3}$$

$$\sigma_y^2(2,\tau,\tau)|_k = \frac{1}{2\tau^2}\left[x_{k+2} - 2x_{k+1} + x_k\right]^2 \tag{A–4}$$

The Allan variance is the expected value of the 2-samples varriance:

$$\sigma_y^2(\tau) = \left\langle \sigma_y^2(2,\tau,\tau)\right\rangle = \frac{1}{2\tau^2}\left\langle x_{k+2} - 2x_{k+1} + x_k\right\rangle_k \tag{A–5}$$

[1] (8), equation (11)

The follwing Python code was used through this work to compute the Allan deviation form timestamps. It is a direct application of Equation 1–8.

```
import numpy as np

def adev(tdiff,per):
    '''Return the Alan deviation.
    tdiff is a list of time samples. Samples equal to np.NaN are
      ↪ ignored.
    per is the sampling period.
    All time units must be homogeneous'''

    tau = range(1,(len(tdiff)-1)/2)
    dev = []
    x = np.array(tdiff,dtype='float64')

    for n in tau:

        x_l = np.array(x[2*n:]-2*x[n:-n]+x[:-2*n],dtype='float64'
          ↪ )
        avar = np.nanmean(x_l*x_l) / (2*n**2*per**2)
        dev.append(np.sqrt(avar))

    return [np.array(tau,dtype='float64')*per,dev]
```

APPENDIX B
APPROXIMATION OF PHASE NOISE TO COMPUTE JITTER

Jitter can be obtained by integrating phase $\mathcal{L}(f)$ with the following equation:

$$x_{jitter} = \frac{1}{2\pi f_0}\sqrt{\int_{1Hz}^{10^5 Hz} 2\mathcal{L}(f)df} \tag{B–1}$$

Usually, phase noise is available in device specifications as tabulated data. Since all common types of phase noise can be accurately modeled as affine functions in the log-log plane (81), a good approximation to integrate $\mathcal{L}(f)$ is to use the trapezoidal method with logarithmic axises. Equation B–2 define the function $\mathcal{L}(f)$ as a line on a log-log figure passing through $(f_1, \mathcal{L}_1)$ and $(f_2, \mathcal{L}_2)$:

$$log_{10}(\mathcal{L}(f)) = \frac{1}{10}\frac{\mathcal{L}_{2|dBc} - \mathcal{L}_{1|dBc}}{log_{10}(f_2) - log_{10}(f_1)} log_{10}(f) + \frac{1}{10}\frac{log_{10}(f_2)\mathcal{L}_{1|dBc} - log_{10}(f_1)\mathcal{L}_{2|dBc}}{log_{10}(f_2) - log_{10}(f_1)} \tag{B–2}$$

This can be rewritten as:

$$\begin{aligned} \mathcal{L}(f) &= 10^{a\cdot log_{10}(f)+b} = 10^{log_{10}(f^a)}10^b = f^a 10^b \\ a &= \frac{\mathcal{L}_{2|dBc} - \mathcal{L}_{1|dBc}}{10(log_{10}(f_2) - log_{10}(f_1))} \qquad b = \frac{log_{10}(f_2)\mathcal{L}_{1|dBc} - log_{10}(f_1)\mathcal{L}_{2|dBc}}{10(log_{10}(f_2) - log_{10}(f_1))} \end{aligned} \tag{B–3}$$

Integration of $\mathcal{L}(f)$ from f_1 to f_2:

$$\int_{f_1}^{f_2} 2\mathcal{L}(f)df = 2\cdot 10^b \int_{f_1}^{f_2} f^a df = 2\frac{f_2^{a+1} - f_1^{a+1}}{a+1}10^b \tag{B–4}$$

With multiple segments, the integration forumal is:

$$\begin{aligned} \int 2\mathcal{L}(f)df &= 2\sum \frac{f_{i+1}^{a_i+1} - f_i^{a_i+1}}{a_i+1}10^{b_i} \\ a_i &= \frac{\mathcal{L}_{i+1|dBc} - \mathcal{L}_{i|dBc}}{10(log_{10}(f_{i+1}) - log_{10}(f_i))} \qquad b_i = \frac{log_{10}(f_{i+1})\mathcal{L}_{i|dBc} - log_{10}(f_i)\mathcal{L}_{i+1|dBc}}{10(log_{10}(f_{i+1}) - log_{10}(f_i))} \end{aligned} \tag{B–5}$$

The follwing Python code was used through this work to comute the jitter from phase noise:

```
import numpy as np

def JitterFromPhaseNoise(Lf,f,f0):
    '''Lf: phase noise in dBc
    f: frequency in Hz
    f0: oscillator frequency
    Lf and f must have the same size'''

    # f_{i}, f_{i+1}, L_{i}, L_{i+1}
    fi = f[:-1]
    fip1 = f[1:]
    Li = Lf[:-1]
    Lip1 = Lf[1:]

    ai = (Lip1-Li) / (np.log10(fip1) - np.log10(fi)) /10.0
    bi = (Li*np.log10(fip1)-Lip1*np.log10(fi)) / (np.log10(fip1)
    ↪ - np.log10(fi)) /10.0
    Sphi = 2*np.sum(  10.0**(bi) * (fip1**(ai+1)-fi**(ai+1))/(ai
    ↪ +1) )

    jitter = 1.0/2/np.pi/f0 * np.sqrt(Sphi)

    return jitter
```

APPENDIX C
COMPUTATION OF THE BIT ERROR RATIO

The follwing Python code was used through this work to compute the BER. Figure 3-32 is obatained with this function.

```
import numpy as np

def BER(Mtau,to,jt,Ml):
    '''Mtau: time dedicated to slots (n * tau)
    to: time offset
    jt: random jitter
    Ml: log2 of M, M is the number of possible symbols
    all time units must be homogeneous'''

    cdf = norm.cdf
    slot=float(Mtau)/(2**Ml)
    pb = 0

    for n in xrange(1,Ml):
        pba = cdf((n+0.5)*slot,to,jt)-cdf((n-0.5)*slot,to,jt)
        pbb = cdf((-n+0.5)*slot,to,jt)-cdf((-n-0.5)*slot,to,jt)
        pb += (pba+pbb)*n

    pb += (1-(cdf((Ml+0.5)*slot,to,jt)-cdf((-Ml-0.5)*slot,to,jt))
    ↪ )*Ml

    return pb/Ml
```

REFERENCES

[1] P. Serra, N. Barnwell, T. Ritz, and J. W. Conklin, "Deep space laser communication transmitter and high precision timing system for small satellites," in *Proceedings of the AIAA/USU Conference on Small Satellites*, 2016. [Online]. Available: https://digitalcommons.usu.edu/cgi/viewcontent.cgi?referer=https://www.google.com/&httpsredir=1&article=3382&context=smallsat

[2] N. S. Barnwell, S. Parry, T. Ritz, P. Serra, and J. Conklin, "Laser amplifier system in a deep space optical transmitter for small satellites," in *AIAA SPACE and Astronautics Forum and Exposition*. American Institute of Aeronautics and Astronautics, sep 2017. [Online]. Available: https://doi.org/10.2514/6.2017-5382

[3] *BIPM Annual Report on Time Activities Volume 11*, 2016. [Online]. Available: https://www.bipm.org/utils/en/pdf/time_ann_rep/Time_annual_report_2016.pdf

[4] D. Kirchner, "Two-way time transfer via communication satellites," *Proceedings of the IEEE*, vol. 79, no. 7, pp. 983–990, jul 1991. [Online]. Available: https://doi.org/10.1109/5.84975

[5] O. Montenbruck and E. Gill, *Satellite Orbits: Models, Methods and Applications*. Springer, 2012. [Online]. Available: https://www.amazon.com/Satellite-Orbits-Models-Methods-Applications-ebook/dp/B00FC6W2LC?SubscriptionId=0JYN1NVW651KCA56C102&tag=techkie-20&linkCode=xm2&camp=2025&creative=165953&creativeASIN=B00FC6W2LC

[6] D. Israel and D. Cornwell, "Lunar laser communication demonstration: Disruption tolerant networking demonstrations over llcd's optical links," January 2014. [Online]. Available: http://ipnsig.org/wp-content/uploads/2014/02/LLCD-DTN-Demonstration-IPNSIG-Final.pdf

[7] Signetics, *Signetics Linear Vol 1 Data Book*. Signetics, 1972. [Online]. Available: https://archive.org/details/bitsavers_signeticsdcsLinearVol1_11470058

[8] D. Allan, "Statistics of atomic frequency standards," *Proceedings of the IEEE*, vol. 54, no. 2, pp. 221–230, 1966. [Online]. Available: https://doi.org/10.1109/proc.1966.4634

[9] D. Allan, N. Ashby, C. Hodge, and H.-P. Company, *The Science of Timekeeping*, ser. Application note. Hewlett-Packard, 1997. [Online]. Available: http://www.allanstime.com/Publications/DWA/Science_Timekeeping/TheScienceOfTimekeeping.pdf

[10] D. Howe, D. Allan, and J. Barnes, "Properties of signal sources and measurement methods," in *Thirty-Fifth Annual Frequency Control Symposium*. IEEE, 1981. [Online]. Available: https://doi.org/10.1109/freq.1981.200541

[11] IEEE standard 1139, "IEEE standard definitions of physical quantities for fundamental frequency and time metrology - random instabilities," March 1999. [Online]. Available: https://doi.org/10.1109/ieeestd.1999.90575

[12] Microsemi, *Quantum™ SA.45s CSAC*, Microsemi Frequency and Time Corporation, Microsemi Corporate Headquarters, One Enterprise, Aliso Viejo, CA 92656 USA, 2014. [Online]. Available: https://www.microsemi.com/document-portal/doc_download/133305-quantum-sa-45s-csac-datasheet

[13] ——, *SA.31m, SA.33m, and SA.35m*, Microsemi Frequency and Time Corporation, Microsemi Corporate Headquarters, One Enterprise, Aliso Viejo, CA 92656 USA, October 2017. [Online]. Available: https://www.microsemi.com/document-portal/doc_download/133364-sa-31m-sa-33m-sa-35m

[14] P. Laurent, M. Abgrall, C. Jentsch, P. Lemonde, G. Santarelli, A. Clairon, I. Maksimovic, S. Bize, C. Salomon, D. Blonde, J. Vega, O. Grosjean, F. Picard, M. Saccoccio, M. Chaubet, N. Ladiette, L. Guillet, I. Zenone, C. Delaroche, and C. Sirmain, "Design of the cold atom PHARAO space clock and initial test results," *Applied Physics B*, vol. 84, no. 4, pp. 683–690, aug 2006. [Online]. Available: https://doi.org/10.1007/s00340-006-2396-6

[15] Microsemi, *IGLOO2 FPGA and SmartFusion2 SoC FPGA*, Microsemi Frequency and Time Corporation, Microsemi Corporate Headquarters, One Enterprise, Aliso Viejo, CA 92656 USA, October 2016, rev. 10.0. [Online]. Available: www.microsemi.com/document-portal/doc_download/132042-igloo2-fpga-datasheet

[16] ——, *SmartFusion2 and IGLOO2 FPGA High-Speed Serial Interfaces*, Microsemi Frequency and Time Corporation, Microsemi Corporate Headquarters, One Enterprise, Aliso Viejo, CA 92656 USA, September 2017, rev. 8.0. [Online]. Available: https://www.microsemi.com/document-portal/doc_view/132011-ug0447-smartfusion2-and-igloo2-fpga-high-speed-serial-interfaces-user-guide

[17] ——, "Mitigation of radiation effects in rtg4 radiation-tolerant flash fpgas," Microsemi Frequency and Time Corporation, Microsemi Corporate Headquarters, One Enterprise, Aliso Viejo, CA 92656 USA, Tech. Rep. WP0191, April 2015. [Online]. Available: https://www.microsemi.com/document-portal/doc_view/135027-wp0191-mitigation-of-radiation-effects-in-rtg4-radiation-tolerant-fpgas-white-paper

[18] S. Henzler, *Time-to-Digital Converters*. Springer Netherlands, 2010. [Online]. Available: https://doi.org/10.1007/978-90-481-8628-0

[19] J. Wu, S. Hansen, and Z. Shi, "ADC and TDC implemented using FPGA," in *2007 IEEE Nuclear Science Symposium Conference Record*. IEEE, oct 2007. [Online]. Available: https://doi.org/10.1109/nssmic.2007.4436331

[20] J. Anderson, N. Barnwell, M. Carrasquilla, J. Chavez, O. Formoso, A. Nelson, T. Noel, S. Nydam, J. Pease, F. Pistella, T. Ritz, S. Roberts, P. Serra, E. Waxman, J. W. Conklin, W. Attai, J. Hanson, A. N. Nguyen, K. Oyadomari, C. Priscal, J. Stupl, J. Wolf, and B. Jaroux, "Sub-nanosecond ground-to-space clock synchronization for nanosatellites using pulsed optical links," *Advances in Space Research*, jun 2017. [Online]. Available: https://doi.org/10.1016/j.asr.2017.06.032

[21] T. Olatunde, R. Shelley, A. Chilton, P. Serra, G. Ciani, G. Mueller, and J. Conklin, "240 nm UV LEDs for LISA test mass charge control," *Journal of Physics: Conference Series*, vol. 610, p. 012034, may 2015. [Online]. Available: https://doi.org/10.1088/1742-6596/610/1/012034

[22] M. Lombardi, L. M Nelson, A. N Novick, and V. Zhang, "Time and frequency measurements using the global positioning system," in *Measurement Science Conference*, vol. 8, 07 2001, pp. 26–33.

[23] P. Fridelance and C. Veillet, "Operation and data analysis in the lasso experiment," *Metrologia*, vol. 32, no. 1, p. 27, 1995. [Online]. Available: http://stacks.iop.org/0026-1394/32/i=1/a=003

[24] J. F. Cavanaugh, J. C. Smith, X. Sun, A. E. Bartels, L. Ramos-Izquierdo, D. J. Krebs, J. F. McGarry, R. Trunzo, A. M. Novo-Gradac, J. L. Britt, J. Karsh, R. B. Katz, A. T. Lukemire, R. Szymkiewicz, D. L. Berry, J. P. Swinski, G. A. Neumann, M. T. Zuber, and D. E. Smith, "The mercury laser altimeter instrument for the MESSENGER mission," *Space Science Reviews*, vol. 131, no. 1-4, pp. 451–479, aug 2007. [Online]. Available: https://doi.org/10.1007/s11214-007-9273-4

[25] X. Sun and G. A. Neumann, "Calibration of the mercury laser altimeter on the MESSENGER spacecraft," *IEEE Transactions on Geoscience and Remote Sensing*, vol. 53, no. 5, pp. 2860–2874, may 2015. [Online]. Available: https://doi.org/10.1109/tgrs.2014.2366080

[26] D. E. Smith, "Two-way laser link over interplanetary distance," *Science*, vol. 311, no. 5757, pp. 53–53, jan 2006. [Online]. Available: https://doi.org/10.1126/science.1120091

[27] É. Samain, J. Weick, P. Vrancken, F. Para, D. Albanese, J. Paris, J.-M. Torre, C. Zhao, P. Guillemot, and I. Petitbon, "Time transfer by laser link –the t2l2 experiment on jason-2 and further experiments," *International Journal of Modern Physics D*, vol. 17, no. 07, pp. 1043–1054, jul 2008. [Online]. Available: https://doi.org/10.1142/s0218271808012681

[28] P. Vrancken, "Characterization of t2l2 (time transfer by laser link) on the jason 2 ocean altimetry satellite and micrometric laser ranging," Ph.D. dissertation, 2008, thèse de doctorat dirigée par Samain, Étienne et Exertier, Pierre Sciences de l'univers Nice 2008. [Online]. Available: http://www.theses.fr/2008NICE4088

[29] L. Ramos-Izquierdo, V. S. S. III, J. Connelly, S. Schmidt, W. Mamakos, J. Guzek, C. Peters, P. Liiva, M. Rodriguez, J. Cavanaugh, and H. Riris, "Optical system design and integration of the lunar orbiter laser altimeter," *Applied Optics*, vol. 48, no. 16, p. 3035, may 2009. [Online]. Available: https://doi.org/10.1364/ao.48.003035

[30] S. Bauer, H. Hussmann, J. Oberst, D. Dirkx, D. Mao, G. Neumann, E. Mazarico, M. Torrence, J. McGarry, D. Smith, and M. Zuber, "Analysis of one-way laser ranging data to LRO, time transfer and clock characterization," *Icarus*, vol. 283, pp. 38–54, feb 2017. [Online]. Available: https://doi.org/10.1016/j.icarus.2016.09.026

[31] M. M. W. J. A. G. F. I. K. B. S. R. D. M. B. M. L. Stevens, R. R. Parenti, "Time-of-flight and ranging experiments on the lunar laser communication demonstration," 2015.

[32] M. P. Hess, J. Kehrer, M. Kufner, S. Durand, G. Hejc, H. Fruhauf, L. Cacciapuoti, R. Much, and R. Nasca, "ACES MWL status and test results," in *2011 Joint Conference of the IEEE International Frequency Control and the European Frequency and Time Forum (FCS) Proceedings*. IEEE, may 2011. [Online]. Available: https://doi.org/10.1109/fcs.2011.5977727

[33] L. You, X. Yang, Y. He, W. Zhang, D. Liu, W. Zhang, L. Zhang, L. Zhang, X. Liu, S. Chen, Z. Wang, and X. Xie, "Jitter analysis of a superconducting nanowire single photon detector," *AIP Advances*, vol. 3, no. 7, p. 072135, jul 2013. [Online]. Available: https://doi.org/10.1063/1.4817581

[34] acam-messelectronic gmbH, *TDC-GPX Datasheet*, ams AG, ams AG, Tobelbaderstrasse 30, 8141 Unterpremstaetten, Austria, January 2007. [Online]. Available: http://ams.com/eng/content/download/728830/1861532/381479

[35] T. Instrument, *MSP430x2xx Family User's Guide*, Texas Instrument Incorporated, 12500 TI Boulevard Dallas, Texas 75243 USA, July 2013, rev. J. [Online]. Available: http://www.ti.com/lit/ug/slau144j/slau144j.pdf

[36] J. Williams, "High voltage, low noise, dc/dc converters: A kilovolt with 100 microvolts of noise," Milpitas, Calif., Tech. Rep. Application Note 118, 2008.

[37] S. Schaefer, W. Rosenkranz, and M. Gregory, "Comparison of homodyne and intradyne detection for high-order modulation schemes in optical intersatellite communication systems," in *2015 IEEE International Conference on Space Optical Systems and Applications (ICSOS)*. IEEE, oct 2015. [Online]. Available: https://doi.org/10.1109/icsos.2015.7425086

[38] B. S. Robert Lange, "Homodyne bpsk-based optical inter-satellite communication links," in *SPIE Photonics West 2007, San Jose*, vol. 6457, 2007, pp. 6457 – 6457 – 9. [Online]. Available: http://dx.doi.org/10.1117/12.698646

[39] J. Costas, "Synchronous communications," *Proceedings of the IRE*, vol. 44, no. 12, pp. 1713–1718, dec 1956. [Online]. Available: https://doi.org/10.1109/jrproc.1956.275063

[40] A. C Clarke, "Extra-terrestrial relays," vol. 51, pp. 305–308, October 1945.

[41] S. Parkes, C. McClements, D. McLaren, A. F. Florit, and A. G. Villafranca, "SpaceFibre networks: SpaceFibre, long paper," in *2016 International SpaceWire Conference (SpaceWire)*. IEEE, oct 2016. [Online]. Available: https://doi.org/10.1109/spacewire.2016.7771599

[42] ECSS Standard ECSS-E-ST-50-12C, "ECSS standard ecss-e-st-50-12c: Spacewire — links, nodes, routers and networks," March 2008.

[43] K. E. Wilson, J. R. Lesh, K. Araki, and Y. Arimoto, "Overview of the ground-to-orbit lasercom demonstration (GOLD)," in *Free-Space Laser Communication Technologies IX*, G. S. Mecherle, Ed. SPIE, apr 1997. [Online]. Available: https://doi.org/10.1117/12.273703

[44] B. I. Edelson and J. N. Pelton, *Satellite Communications Systems and Technology (Advanced Computing & Telecommunications Ser.)*. William Andrew, 1995. [Online]. Available: https://www.amazon.com/Satellite-Communications-Technology-Computing-Telecommunications/dp/0815513704?SubscriptionId=0JYN1NVW651KCA56C102&tag=techkie-20&linkCode=xm2&camp=2025&creative=165953&creativeASIN=0815513704

[45] G. Meurant, *Satellite Communications Systems and Technology*, ser. Advanced computing and telecommunications series. Elsevier Science, 1995. [Online]. Available: https://books.google.com/books?id=-uFQBAAAQBAJ

[46] N. Karafolas, Z. Sodnik, J. Armengol, and I. Mckenzie, "Optical communications in space," in *2009 International Conference on Optical Network Design and Modeling, ONDM 2009*, 01 2009, pp. 1–6.

[47] I. I. Kim, B. Riley, N. M. Wong, M. Mitchell, W. Brown, H. Hakakha, P. Adhikari, and E. J. Korevaar, "Lessons learned for STRV-2 satellite-to-ground lasercom experiment," in *Free-Space Laser Communication Technologies XIII*, G. S. Mecherle, Ed. SPIE, jun 2001. [Online]. Available: https://doi.org/10.1117/12.430772

[48] R. Stieger, J. Schuster, P. Adhikari, H. Hakakha, B. Riley, J. Koontz, A. Lath, C. Moursund, M. Barclay, and E. Korevaar, "Experimental operations for STRV-2 satellite lasercom terminal," in *24th European Conference on Optical Communication. ECOC '98 (IEEE Cat. No.98TH8398)*. Telefonica, Sep 1998, pp. 667–668 vol.1. [Online]. Available: https://doi.org/10.1109/ecoc.1998.732770

[49] M. Toyoshima, T. Takahashi, K. Suzuki, S. Kimura, K. Takizawa, T. Kuri, W. Klaus, M. Toyoda, H. Kunimori, T. Jono, Y. Takayama, and K. Arai, "Results from phase-1, phase-2 and phase-3 kirari optical communication demonstration experiments with the NICT optical ground station (KODEN)," in *25th AIAA International Communications Satellite Systems Conference (organized by APSCC)*. American Institute of Aeronautics and Astronautics, apr 2007. [Online]. Available: https://doi.org/10.2514/6.2007-3228

[50] N. Perlot, M. Knapek, D. Giggenbach, J. Horwath, M. Brechtelsbauer, Y. Takayama, and T. Jono, "Results of the optical downlink experiment KIODO from OICETS satellite to optical ground station oberpfaffenhofen (OGS-OP)," in *Free-Space Laser Communication Technologies XIX and Atmospheric Propagation of Electromagnetic Waves*, S. Mecherle and O. Korotkova, Eds. SPIE, feb 2007. [Online]. Available: https://doi.org/10.1117/12.708413

[51] R. Ballweg, "EDRS operations at GSOC - relevant heritage and new developments," in *SpaceOps 2012 Conference*. American Institute of Aeronautics and Astronautics, jun 2012. [Online]. Available: https://doi.org/10.2514/6.2012-1275210

[52] T. Tanaka, Y. Kawamura, and T. Tanaka, "Overview and operations of CubeSat FITSAT-1 (NIWAKA)," in *2013 6th International Conference on Recent Advances in Space Technologies (RAST)*. IEEE, jun 2013. [Online]. Available: https://doi.org/10.1109/rast.2013.6581339

[53] R. C. Elphic and C. T. Russell, Eds., *The Lunar Atmosphere and Dust Environment Explorer Mission (LADEE)*. Springer International Publishing, 2015. [Online]. Available: https://doi.org/10.1007/978-3-319-18717-4

[54] D. M. Boroson, B. S. Robinson, D. V. Murphy, D. A. Burianek, F. Khatri, J. M. Kovalik, Z. Sodnik, and D. M. Cornwell, "Overview and results of the lunar laser communication demonstration," in *Free-Space Laser Communication and Atmospheric Propagation XXVI*, H. Hemmati and D. M. Boroson, Eds. SPIE, mar 2014. [Online]. Available: https://doi.org/10.1117/12.2045508

[55] S. Constantine, L. E. Elgin, M. L. Stevens, J. A. Greco, K. Aquino, D. D. Alves, and B. S. Robinson, "Design of a high-speed space modem for the lunar laser communications demonstration," in *Free-Space Laser Communication Technologies XXIII*, H. Hemmati, Ed. SPIE, feb 2011. [Online]. Available: https://doi.org/10.1117/12.878927

[56] B. V. Oaida, W. Wu, B. I. Erkmen, A. Biswas, K. S. Andrews, M. Kokorowski, and M. Wilkerson, "Optical link design and validation testing of the optical payload for lasercomm science (OPALS) system," in *Free-Space Laser Communication and Atmospheric Propagation XXVI*, H. Hemmati and D. M. Boroson, Eds. SPIE, mar 2014. [Online]. Available: https://doi.org/10.1117/12.2045351

[57] O. V. Sindiy, M. J. Abrahamson, A. Biswas, M. W. Wright, J. H. Padams, and A. L. Konyha, "Lessons learned from optical payload for lasercomm science (opals) mission operations," in *AIAA SPACE 2015 Conference and Exposition*, 2015, p. 4657.

[58] A. Carrasco-Casado, H. Takenaka, D. Kolev, Y. Munemasa, H. Kunimori, K. Suzuki, T. Fuse, T. Kubo-Oka, M. Akioka, Y. Koyama, and M. Toyoshima, "LEO-to-ground optical communications using SOTA (small optical TrAnsponder) – payload verification results and experiments on space quantum communications," *Acta Astronautica*, vol. 139, pp. 377–384, oct 2017. [Online]. Available: https://doi.org/10.1016/j.actaastro.2017.07.030

[59] R. P. Welle, "Cubesat–scale laser communications," in *31st Space Symposium, Colorado Springs*, 2015.

[60] S. W. Janson and R. P. Welle, "The nasa optical communication and sensor demonstration program: an update," in *28th Annual AIAA/USU Conference on Small Satellites*, 2014.

[61] E. Benzi, D. C. Troendle, I. Shurmer, M. James, M. Lutzer, and S. Kuhlmann, "Optical inter-satellite communication: the alphasat and sentinel-1a in-orbit experience," in

SpaceOps 2016 Conference. American Institute of Aeronautics and Astronautics, may 2016. [Online]. Available: https://doi.org/10.2514/6.2016-2389

[62] T. Kubo-oka, H. Kunimori, H. Takenaka, T. Fuse, and M. Toyoshima, "Optical communication experiment using very small optical transponder component on a small satellite risesat," in *Proc. International Conference on Space Optical Systems and Applications (ICSOS) 2012*, 2012.

[63] B. Edwards, "Overview of the laser communications relay demonstration project," in *SpaceOps 2012 Conference*. American Institute of Aeronautics and Astronautics, jun 2012. [Online]. Available: https://doi.org/10.2514/6.2012-1261897

[64] H. Hemmati, "Status of free-space optical communications program at JPL," in *2000 IEEE Aerospace Conference. Proceedings (Cat. No.00TH8484)*. IEEE, 2000. [Online]. Available: https://doi.org/10.1109/aero.2000.879838

[65] H. Hemmati, A. Biswas, and I. B. Djordjevic, "Deep-space optical communications: Future perspectives and applications," *Proceedings of the IEEE*, vol. 99, no. 11, pp. 2020–2039, nov 2011. [Online]. Available: https://doi.org/10.1109/jproc.2011.2160609

[66] K. E. Wilson, J. R. Lesh, and T.-Y. Yan, "GOPEX: a laser uplink to the galileo spacecraft on its way to jupiter," in *Free-Space Laser Communication Technologies V*, G. S. Mecherle, Ed. SPIE, aug 1993. [Online]. Available: https://doi.org/10.1117/12.149251

[67] Y. Arimoto, M. Toyoshima, M. Toyoda, T. Takahashi, M. Shikatani, and K. Araki, "Preliminary result on laser communication experiment using (ets-vi)," in *Photonics West '95, Proceedings Volume 2381, Free-Space Laser Communication Technologies VII*, vol. 2381, 1995, pp. 2381 – 2381 – 8. [Online]. Available: http://dx.doi.org/10.1117/12.207423

[68] M. Toyoshima and Y. Takayama, "Free-space laser communications: The japanese experience," in *2009 35th European Conference on Optical Communication*, Sept 2009, pp. 1–4.

[69] H. Kaushal and G. Kaddoum, "Optical communication in space: Challenges and mitigation techniques," *IEEE Communications Surveys & Tutorials*, vol. 19, no. 1, pp. 57–96, 2017. [Online]. Available: https://doi.org/10.1109/comst.2016.2603518

[70] T. Tolker-Nielsen and J.-C. Guillen, "Silex: The first european optical communication terminal in orbit," Tech. Rep., 1998. [Online]. Available: http://www.esa.int/esapub/bulletin/bullet96/NIELSEN.pdf

[71] Z. Sodnik, B. Furch, and H. Lutz, "Free-space laser communication activities in europe: SILEX and beyond," in *2006 IEEE LEOS Annual Meeting Conference Proceedings*. IEEE, oct 2006. [Online]. Available: https://doi.org/10.1109/leos.2006.278845

[72] E. Leitgeb, M. Gebhart, and U. Birnbacher, "Optical networks, last mile access and applications," *Journal of Optical and Fiber Communications Reports*, vol. 2, no. 1, pp. 56–85, Mar 2005. [Online]. Available: https://doi.org/10.1007/s10297-004-0025-x

[73] H. Lutz, "Optical communications in space - twenty years of esa effort," Tech. Rep., 1997. [Online]. Available: https://esamultimedia.esa.int/multimedia/publications/ESA-Bulletin-091/

[74] Microsemi, *SmartFusion2 and IGLOO2 Clocking Resources*, Microsemi Frequency and Time Corporation, Microsemi Corporate Headquarters, One Enterprise, Aliso Viejo, CA 92656 USA, July 2017, rev. 7.0. [Online]. Available: https://www.microsemi.com/document-portal/doc_view/132012-ug0449-smartfusion2-and-igloo2-clocking-resources-user-guide

[75] M. Majzoobi, F. Koushanfar, and M. Potkonjak, "Techniques for design and implementation of secure reconfigurable PUFs," *ACM Transactions on Reconfigurable Technology and Systems*, vol. 2, no. 1, pp. 1–33, mar 2009. [Online]. Available: https://doi.org/10.1145/1502781.1502786

[76] M. P. Li, *Jitter, Noise, and Signal Integrity at High-Speed*. Prentice Hall, 2007. [Online]. Available: https://www.amazon.com/Jitter-Noise-Signal-Integrity-High-Speed/dp/0132429616?SubscriptionId=0JYN1NVW651KCA56C102&tag=techkie-20&linkCode=xm2&camp=2025&creative=165953&creativeASIN=0132429616

[77] K. Y. Lau, "Gain switching of semiconductor injection lasers," *Applied Physics Letters*, vol. 52, no. 4, pp. 257–259, jan 1988. [Online]. Available: https://doi.org/10.1063/1.99486

[78] T. Sogawa, Y. Arakawa, M. Tanaka, and H. Sakaki, "Observation of a short optical pulse ($<$1.3 ps) from a gain-switched quantum well laser," *Applied Physics Letters*, vol. 53, no. 17, pp. 1580–1582, oct 1988. [Online]. Available: https://doi.org/10.1063/1.99955

[79] L. Chusseau and C. Kazmierski, "Optimum linear pulse compression of a gain-switched 1.5 μm DFB laser," *IEEE Photonics Technology Letters*, vol. 6, no. 1, pp. 24–26, jan 1994. [Online]. Available: https://doi.org/10.1109/68.265878

[80] R. W. Kingsbury, "Optical communications for small satellites," Ph.D. dissertation, Massachusetts Institute of Technology, 2015.

[81] J. Rutman and F. Walls, "Characterization of frequency stability in precision frequency sources," *Proceedings of the IEEE*, vol. 79, no. 7, pp. 952–960, jul 1991. [Online]. Available: https://doi.org/10.1109/5.84972

BIOGRAPHICAL SKETCH

Paul Serra is a PhD student in the Mechanical and Aerospace Engineering Department at the University of Florida. He received a Master of Sciences in Aerospace Engineering from University of Florida and a Graduate Engineering Degree from Arts et Métiers ParisTech, in France, in 2014. He received his Ph.D. from the University of Florida in the spring of 2018. Paul works with John Conklin in the Precision Space Systems Laboratory on precision timing measurements and generation applied to navigation and free-space laser communications. His research includes the design, fabrication, and on-orbit characterization of timing instruments for compact spacecraft.